IPP-Report

Max-Planck-Institut
für Plasmaphysik

Dorothea Gradic

Doppler Coherence Imaging of Ion Dynamics in the plasma experiments VINETA.II and ASDEX Upgrade

IPP 2018-19
August 2018

Doppler Coherence Imaging of Ion Dynamics in the plasma experiments VINETA.II and ASDEX Upgrade

vorgelegt von
Master of Science in Physics
Dorothea Gradic
geb. in Fürth

von der Fakultät II - Mathematik und Naturwissenschaften
der Technischen Universität Berlin
zur Erlangung des akademischen Grades

Doktor der Naturwissenschaften
- Dr. rer. nat -

genehmigte Dissertation

Promotionsausschuss:

Vorsitzender: Prof. Dr. rer. nat. Holger Stark
Erster Gutachter: Prof. Dr. rer. nat. Dieter Breitschwert
Zweiter Gutachter: Prof. Dr. rer. nat. Robert C. Wolf
Dritter Gutachter: Prof. Dr. rer. nat. John Howard

Tag der wissenschaftlichen Aussprache: 10. April 2018

Berlin, 2018

Abstract

In magnetically confining plasma experiments, measurement of ion dynamics is of great importance to study the plasma behaviour in magnetic fields such as the exhaust particle flows in the divertor areas. The plasma exhaust heat flux in a future nuclear power plant is estimated to be too high for the proposed wall materials. This is due to the relatively small areas, where the exhaust plasma interacts with the wall, that result in high local heat loads in these small interaction areas. A solution for the exhaust problem for future high power plasma experiments is one of the major challenges for magnetic confinement fusion as an energy source. High quality experimental measurements are necessary to improve understanding of the scrape-off-layer (SOL) and divertor physics as well as to validate simulation results of edge codes such as e.g. EMC3-Eirene or SOLPS. Understanding the plasma exhaust and edge behaviour is crucial to make correct assumptions about a future, large-sized power plant. This thesis is concerned with the development of a diagnostic measuring impurity ion flows in the SOL and divertor as well as basic physical understanding of these measured flows.
Doppler coherence imaging spectroscopy (CIS) is a relatively new technique for the observation of plasma bulk ion dynamics in magnetically confined plasma experiments. It is a passive optical diagnostic that measures 2D images of the line-integrated ion flow and temperature, thus having the potential to vastly increase our knowledge about the SOL physics.
Since its invention, the Doppler CIS has been further developed and tested in several plasma experiments such as DIII-D, H-1NF, MAGPIE and MAST. The Doppler CIS has the advantage of a relatively simple hardware set-up with high entendue, providing high flow sensitivity and an order of magnitude more data at higher signal-to-noise than traditional systems. However, absolute flow calibration has proven to be difficult for many impurity ion species present in the divertor of larger plasma experiments. This is due to lack of nearby calibration lines, ambient temperature changes of the diagnostic hardware as well as the difficulty to create a calibration light source equivalent to the plasma.

The diagnostic was used successfully for first Doppler CIS ion flow measurements in the small, low-temperature linear plasma experiment VINETA.II and the medium-sized tokamak ASDEX Upgrade (AUG). The main physics objective of these studies is the research of ion dynamics in the two experiments. In VINETA.II, drifts due to electric fields were found to dominate ion dynamics. In the SOL and divertor of AUG, though there is a complex interplay of several drive mechanisms influencing the impurity ion dynamics, flows were found to be rather stable in the set of discharges where the Doppler CIS was employed. The physical background of SOL and divertor flows is reviewed in detail. This work focuses on the general characteristics of impurity ion flows in the poloidal field divertor and on bulk plasma ion flow in VINETA.II. Doppler CIS measurements from both experiments are presented: C-III, He-II and D-I in AUG as well as Ar II flows in VINETA.II. A flexible diagnostic set-up was designed to directly calibrate each flow measurement immediately before and after an investigated plasma discharge, making absolutely calibrated flow measurements possible without the use of active or passive temperature control. In AUG, they show a change of flow sign between the two divertor legs that is expected due to magnetic topology. The measured flow speeds are in the range of several kilometers per second and are mainly parallel to the magnetic field lines.

Zusammenfassung

In Plasmaexperimenten mit magnetischem Einschluss ist die Messung von Ionen-Dynamiken essentiell um das Plasmaverhalten in Magnetfeldern zu verstehen. Insbesondere ist das ausströmende Plasma im (magnetisch offenen) Rand- und Divertorbereich vom großen Interesse, da in einem zukünftigen Kernfusionsreaktor die Wärmeflüsse auf die Wand als sehr groß eingeschätzt werden. Dies liegt daran, dass die Regionen, in denen das ausströmende Plasma auf die Wand trifft, räumlich klein sind und die lokale Wärmebelastung pro Fläche dadurch sehr groß wird. Die Lösung dieses Problems ist eine Voraussetzung, um die Kernfusion mit magnetisch eingeschlossenen Hochtemperaturplasmen nutzen zu können. Genaue Messungen werden benötigt, um das Verständnis des Plasmas im magnetisch offenen Randbereich und am Divertor zu verbessern, sowie um entsprechende Computersimulationen von Codes wie EMC3-Eirene oder SOLPS zu verifizieren. Das Verstehen und korrekte Beschreiben des Randschichtplasmas ist entscheidend, um die richtige Auslegung für das ausströmende Plasma bei zukünftigen, großen Hochtemperatur-Plasmaanlagen treffen zu können. Diese Arbeit beschäftigt sich mit der Entwicklung einer spektralen Diagnostik, die die Verunreinigungsflüsse im offenen Randbereich messen kann. Der Fluss von Wand-Verunreinigungen spielt eine wichtige Rolle für den Betrieb eines Plasmaexperimentes und lässt auch Rückschlüsse auf die ausströmenden Ionenflüsse des Hauptplasmas zu.
Das Doppler-Kohärenz-Abbildungsverfahren ist eine relativ neue Methode zur Messung von Ionendynamiken in Plasmaexperimenten. Optisch passiv nimmt sie Bilder aus dem sichtbaren Bereich vom Plasma auf und kann den linienintegrierten Ionenfluss und die Ionentemperatur in ihnen sichtbar machen. Beide Parameter können bisher vor allem nur lokal in der Randschicht gemessen werden. Die Doppler-Kohärenz-Abbildungs-Diagnostik (KAD) hat deshalb das Potential, unser Verständnis dieser beiden Parameter für die Randschichtphysik deutlich zu vergrößern.
Seit ihrer Erfindung wurde die Doppler KAD weiterentwickelt und in mehreren Plasmaexperimenten (DIII-D, WEGA, H-1NF, MAGPIE, MAST...) eingesetzt. Sie zeichnet sich durch einen relativ simplen Aufbau mit großem Entendue aus und liefert ca. eine Größenordnung mehr Daten mit höherem Signal-zu-Rausch-Verhältnis als traditionelle spektroskopische Systeme. Allerdings ist die Kalibration der Flussmessung für viele spektrale Plasmalinien sehr schwierig. Dies liegt am teilweisen Fehlen von geeigneten Kalibrationslinien, Temperaturveränderungen der Diagnostik-Kristalle und an dem Umstand, dass die Diagnostik nicht in der Objektebene innerhalb des Torus kalibriert werden kann.

Erfolgreiche Messungen mit der Diagnostik wurden am linearen Niedertemperatur-Plasmaexperiment VINETA.II und dem Tokamak ASDEX Upgrade (AUG) durchgeführt. Das physikalische Ziel dieser Messungen war die Untersuchung der Ionendynamiken in beiden Experimenten. In VINETA.II wurden azimutale Plasma-Driften aufgrund von einem radialen elektrischen Feld gemessen. Im offenen Randschichtbereich und am Divertor von AUG gibt es ein komplexeres Zusammenwirken von verschiedenen Flussursachen. Trotzdem wurden in den mit der Doppler KAD untersuchten Entladungen für verschiedene Verunreinigungsspezies relativ konstante Flüsse beobachtet. Die verschiedenen physikalischen Ursachen von Ionenflüssen werden im Detail für poloidale Feld-Divertoren (eingesetzt in AUG) sowie für das Hauptplasma in VINETA.II beschrieben. Messungen aus beiden Experimenten werden präsentiert: C III, He II und D-α in AUG sowie für Ar II Flüsse in VINETA.II. Ein flexibler Diagnostik-Aufbau wurde realisiert, um direkt vor und nach jeder Plasmaentladung kalibrieren zu können. Dies ermöglichte absolut kalibrierte Flussmessungen ohne die Nutzung von aktiver oder passiver Temperaturkontrolle.

In AUG wurde ein Wechsel der Flussrichtung (vom Beobachter weg bzw. zum Beobachter hin) zwischen den beiden Divertorbeinen beobachtet. Dies wird aufgrund der Magnetfeldtopologie erwartet. Die gemessenen Flussgeschwindigkeiten liegen im Bereich von mehreren Kilometern pro Sekunde und sind hauptsächlich parallel zu den Magnetfeldlinien.

Contents

1 Introduction

Modern life and society as we know it today in Europe would not be possible without electrical power. Infrastructure, business, industry, science and people's everyday lives increasingly depend on it and there is no reason to assume that this will change in the near future.
In the next decades, a large increase of the global (electric) energy demand is to be expected. There is a great variety of prognoses, for example by the U.S. Energy Information Administration[1] or the BP energy outlook[2], that predict rises on the order of 40% until 2040. Even with decreasing energy demands in highly developed countries by the use of more energy-efficient technologies, this trend is not expected to stop. The main reasons for the enormous increase are rising population levels in many parts of the world as well as increasing living standards in key countries such as India or China.
About 80% of todays global energy consumption is provided by fossil fuel sources[3], due to technological as well as economical reasons. Despite political efforts, fossil fuel usage is expected to grow. However, fossil fuels are limited and at some point in the future will not cover the increasing energy demand anymore. Furthermore, scientific consensus is that fossil fuel waste has a serious impact on the Earth's climate, stating that the warming of the climate system is unequivocal [1] (p.2) and that human influence was the dominant cause of global warming between 1951-2010 [1] (p.13). This is why political efforts are undertaken to utilize greenhouse gas free energy suppliers.

Notable large, greenhouse gas free energy sources exist such as so-called renewable energies or nuclear fission. The term 'renewable' refers to resources that are naturally replenished on a human timescale, for example sunlight, wind, hydro power, bio-mass and geothermal heat. Usage, energy gain and research of renewable sources have risen significantly in last years. However, many renewable energies suffer from either limited geographic or stochastic availabilities. Moreover, it is not clear whether the existing renewable technologies can provide the entire energy demand of large, industrial countries such as Germany [2]. This is mainly due to storage concerns, large fluctuating energy surpluses or shortages and the need for more capacities in the existing electrical grids.
Nuclear fission power plants are a steady energy source, but produce long-lived radioactive waste and suffer from safety concerns in the public image.

In order to meet the rising global energy demand and climate protection goals, there is ongoing scientific research for more greenhouse gas free energy sources. These include

[1] International Energy Outlook 2016: `www.eia.gov/forecasts/ieo/pdf/0484(2016).pdf` (May 2017)
[2] `http://www.bp.com/content/dam/bp/pdf/energy-economics/energy-outlook-2017/bp-energy-outlook-2017.pdf` (May 2017)
[3] `https://www.iea.org/publications/freepublications/publication/KeyWorld2016.pdf` (May 2017)

developments for i.e. tidal power stations [3], bio-fuels from algae [4], airborne wind energy systems [5] or next-generation fast fission reactors that yield less nuclear waste ([6],[7]). However, there is only one electric power source currently under development, that would access a new primary energy carrier: deuterium and lithium by nuclear fusion. Primary refers to naturally occurring energy carriers necessary for the generation of useful energy for human society. Nuclear fusion research has the ultimate goal of developing a power plant capable of the economic production of electricity. Next to electricity, nuclear fusion would also be a very good source of high-temperature process heat. Fusion power plants are expected to have none of the aforementioned disadvantages but provide large amounts of energy from an almost endless resource.

Nuclear fusion has been investigated with much effort since the 1950s. Even after 60 years of successful international research, there are questions that remain unanswered of how to ultimately realize a nuclear fusion power plant. This is due to the plasma state in which the fusion fuel needs to be present. Plasma physics is a complex and broad area of research covering several fundamental physics areas like electromagnetism, fluid physics and thermodynamics. Comprehension of hot plasmas in magnetic fields is necessary to understand how to build a nuclear fusion power plant (based on magnetic confinement). An essential problem is the sufficient energy confinement of the plasma and the simultaneous removal of non-fuel plasma particles in a magnetic field. In order to observe and thus understand the behaviour of hot plasmas in experimental fusion devices, accurate and detailed measurements need to be obtained. This thesis is concerned with the development of a relatively new diagnostic instrumentation for one such measurement.

The first nuclear fusion experiment that is expected to demonstrate a burning fusion plasma (and by this the possibility of a nuclear fusion power plant) is the international ITER project, which is currently under construction in Cadarache, France. The first operation phase of ITER is scheduled for 2025. Different fusion roadmaps aim at demonstration plants before 2050 (China) [8] or after 2050 (Europe).

1.1 Nuclear fusion

The term 'nuclear fusion' denotes the merging of two nuclei, by which nuclear binding energy is converted into kinetic energy of the fusion products. The fusion process of most interest for energy production on Earth is the D-T fusion reaction:

$$ {}^{2}_{1}\mathrm{D} + {}^{3}_{1}\mathrm{T} \rightarrow {}^{4}_{2}\mathrm{He}(3.5\mathrm{MeV}) + {}^{1}_{0}\mathrm{n}(14.1\mathrm{MeV}). \tag{1} $$

The D-T fusion reaction has the highest reaction rate $\langle \sigma v \rangle$. Furthermore, it has a particularly large collision probability, σ, at the lowest fusion particle temperatures.

In a fusion power plant, a positive net energy balance has to be produced between the power gained by a large number of fusion events and the power to operate the plant. There is a

Coulomb barrier between the positive charges of the two fusing nuclei. In order to overcome this barrier, the D and T nuclei need to have high energies, and in order to have a positive energy balance in a fusion power plant, a sufficiently large number of collisions per particle is necessary. This implies high temperatures (particles with high energy in thermal equilibrium) of several 10 million degrees Kelvin or a few keV[4]. At these temperatures, the fusion constituents are in the state of a plasma. A plasma can be thought of as a gas composed of free electrons and ions, but with a collective behaviour. Given the right plasma temperature T, electron density n_e and energy confinement time τ_E, enough D-T ions are able to fuse with each other. The energy confinement time is a (statistical) measure for the quality of energy confinement, i.e. how long energy inside a fusion plasma is contained. From the power balance for D-T fusion, $P_\alpha + P_{\mathtt{heat}} = W/\tau_E$ ($P_{\mathtt{heat}} \to 0$), the triple product $n_e \tau_E T$ can be derived, which has to exceed the value

$$n_e \tau_E T \geq 3 \cdot 10^{21} \mathrm{keV} \frac{\mathrm{s}}{\mathrm{m}^3} \tag{2}$$

for the plasma to self-sustain its temperature with the gained fusion energy. Given a plasma (ion) temperature of about 10 keV (temperature with maximum reaction rate $\langle \sigma v \rangle$ for D-T fusion), this translates into plasma densities on the order of $10^{20}\ \mathrm{m}^{-3}$ and energy confinement times of several seconds[5].

As an energy source, nuclear fusion has a very high energy gain per reaction, which is 17.6 MeV for D-T. In contrast, the chemical process of burning coal has an energy gain of 5 eV per reaction. As a result, a nuclear fusion power plant needs much less fuel resources over time than conventional power plants relying on coal or gas: For a 1 GW electrical power coal plant, roughly 4000 t of coal are necessary per day[6]. A 1 GW electrical fusion power plant is expected to only require about 270 g of deuterium and about 8 kg natural lithium per day. The lithium is used to breed the radioactive tritium with the neutrons produced by the fusion reaction. Since tritium has a half-life decay time of 12.3 years, only negligible tritium reserves exist on Earth. Therefore, tritium needs to be produced in a closed breeding cycle in a fusion power plant. Lithium is available on Earth in large quantities, as well as deuterium, which can be gained from seawater.

Unlike fission, the fusion reaction itself does not produce radioactive elements, but some radioactive waste will be produced by the fusion neutrons, activating reactor components. However, all of this material, after remaining in the reactor building after the end of operation for some decades, may be regarded as non-radioactive or recycled, with no need for deep geological disposal [9].

[4] 1 eV $\hat{=}$ 11605 K. In plasma and fusion physics, it is common to use eV as a unit of temperature. The conversion to Kelvin is defined by dividing eV by k_B, the Boltzmann constant: $T\,[K] = E\,[eV]/k_B$.

[5] For a plasma-to-magnetic field pressure ratio $\beta = 5\%$ at $B = 5\,\mathrm{T}$

[6] `http://fusionforenergy.europa.eu/understandingfusion/merits.aspx` (May 2017)

In order to generate and contain a hot fusion-burning plasma, that sustains the fusion conditions by itself, many concepts have been investigated experimentally and theoretically since the 1950s [10]. Equ. (2) cannot be achieved by simply directing deuterium and tritium beams with the required energies at each other. Some sort of confinement is necessary to reach and sustain the densities and temperatures needed for a fusion reactor. Due to the high temperature, mechanical fuel cells or containers are not applicable to contain the fusion plasma. One possibility to confine a plasma are magnetic and electric fields, since a plasma consists of charged particles which can be influenced by these fields. There are also other ways such as inertial confinement fusion, however this work is only concerned with plasma experiments based on magnetic confinement. Over the past 50 years, the magnetic confinement concept has gained a solid technical and physical foundation that has led to the construction of major facilities aimed at demonstrating fusion energy producing plasmas such as the Joint European Torus (JET) or ITER.
In a future fusion power plant based on magnetic confinement, the fusion-produced helium nuclei are envisaged to transfer their kinetic energy to the plasma by collisions. After being thermalised, the helium particles need to be removed, since they act as an impurity and don't contribute to the nuclear fusion process anymore. The fusion neutrons, which are not confined by the magnetic field, are planned to transfer their kinetic energy to a heat blanket placed around the confining magnetic field area. The blankets are also planned to contain the lithium for breeding the tritium fuel. The neutron-heated blankets are going to drive a thermal turbine cycle, as in conventional coal or fission power plants.

1.2 Magnetic confinement

Since plasma particles are charged, they are subject to the Lorentz force

$$\vec{F_L} = q(\vec{v} \times \vec{B})$$

when they move with a perpendicular component to a magnetic field line. By the Lorentz force, they are constrained to gyrate around the field lines and thus can be confined by a magnetic field. The outward-directed thermal pressure of the plasma is balanced by the magnetic forces to retain the plasma in an equilibrium configuration.
Magnetic confinement devices include linear (pinch) experiments, mirror machines, levitated dipoles, tokamaks and stellarators. Today, there are many applications of linear or electric devices that are used for e.g. the investigation of low-temperature plasma physics or for research related to astrophysics. Key fusion experiments in operation and under construction today make use either of the tokamak or the stellarator concept. These two concepts were invented in the late 1950s and 60s. The idea for both of them was to bend the linear machine into a circle in order to avoid end losses, making them a torus. However, confined particles in a torus experience additional forces. In general, if there is a force $\vec{F}$ acting perpendicular to the

magnetic field $\vec{B}$, the guiding centre of a gyrating charged particle experiences a drift motion $\vec{v}_d$ perpendicular to $\vec{F}$ and $\vec{B}$:

$$\vec{v}_d = \frac{\vec{F} \times \vec{B}}{qB^2} \tag{3}$$

Sources of forces may be gravitation, electric fields or magnetic inhomogeneities in space and time.

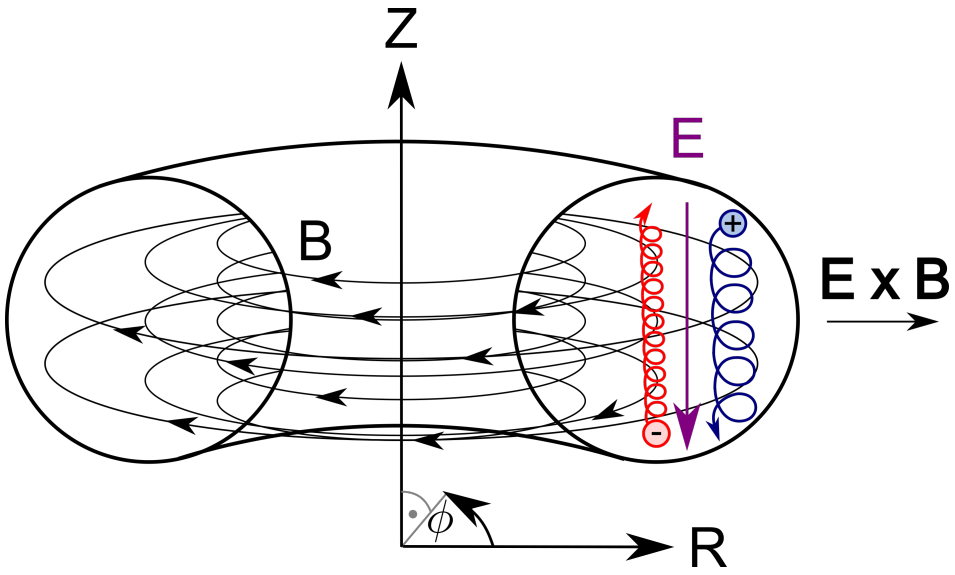

Figure 1 – Drift of charged particles in a toroidal magnetic field. The negative and positive charges try to drift up- and downwards due to spacial inhomogeneities and the curvature of the magnetic field. The electric field caused by the charge separation leads to a vertical drift of the charged particles.

For a toroidal magnetic field, particular particle drifts are caused by the curvature and gradient of the field. It is stronger on the inboard than on the outboard side of the torus. (This is why the inboard side is often referred to as the high field side and the outboard as the low field side.) The gradient force $\vec{F}_{\nabla B} = -\mu\vec{\nabla}\vec{B}$ and centripetal force due to the curvature, $\vec{F}_c = mv_\parallel^2 \frac{\vec{R}_c}{R_c^2}$, lead to charge-dependent drifts of the particles. In Figure 1, the magnetic field is oriented in such a way that the $\vec{\nabla}\vec{B}$-drift and curvature drift of the ions is directed downwards. This is the orientation in most experimental devices.
The attempt of the charges to separate causes an electric field $\vec{E}$, which leads to a charge-independent outward drift of the ions and electrons (cf. Figure 1):

$$\vec{v}_{E\times B} = \frac{q\vec{E} \times \vec{B}}{qB^2} = \frac{\vec{E} \times \vec{B}}{B^2}$$

Because of this outward drift, a simple toroidal concept is not sufficient for good magnetic confinement. An additional poloidal[7] field is necessary to twist the magnetic field lines. The

[7]Poloidal means all directions in a vertical (R, Z)-plane of a torus, as e.g. the plane in Figure 1 in which the electrons and ions are schematised to gyrate. The toroidal direction is along ϕ.

twist balances outward drifts.

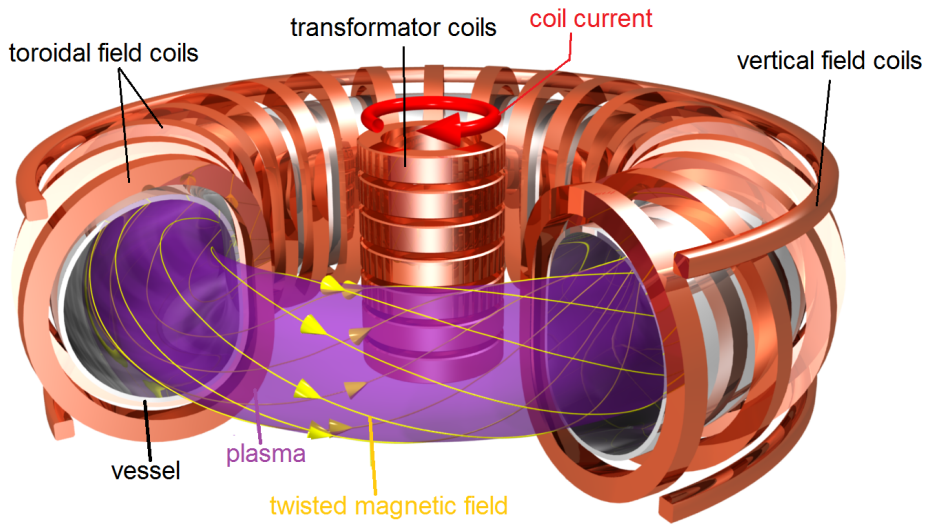

Figure 2 – Schematic of a tokamak. The plasma confining magnetic field is produced by toroidal mangetic field coils and a plasma current, that is induced by a transformer coil. Graphic: IPP, Christian Brandt.

There are two major ideas of how to realize the helical magnetic field configuration. One is the tokamak, the name being a russian acronym for 'toroidal chamber with magnetic field coils'. An overview of the tokamak concept is provided in Figure 2. Toroidal field coils produce the ring-shaped magnetic field. In the centre of the device, there is a transformer, which induces a toroidal current into the plasma. This plasma current (not illustrated in Figure 2) in turn generates a poloidal magnetic field. The superposition of the poloidal and toroidal magnetic fields produce the twisted field lines. The vertical field coils are used to balance and shape the plasma into an elliptical or triangular form.

The plasma current, which is on the order of MA in many tokamaks, is maintained by the transformer for a limited amount of time. The current can be applied for ohmically heating the plasma. However, plasma resistivity, $\eta \propto k_B T_e^{-3/2}$, decreases with increasing temperature. Due to the Coulomb cross-section of the typical plasma particle collisions, that decrease for higher average velocities of the plasma particles. The higher the relative speed between the colliding particles, the shorter their interaction time will be. Usually, the plasma becomes too good a conductor at temperatures above 1 keV for ohmic heating to be effective ([11], p.170). In present tokamaks, not the production of energy, but the magnetic confinement of high-temperature hydrogen plasmas is the focus of research. Not many of these high-temperature plasma experiments are equipped to operate with tritium and thus there is no heating by nuclear fusion products, but only external heating schemes. To study high-temperature, non-burning plasmas above 1 keV, other heating mechanisms need to be applied. Microwaves resonant to the electron and ion gyration frequencies (usually in the GHz (electron) and MHz (ion) range) can be used to effectively heat the plasma. They are referred to as electron and ion cyclotron resonant heating

(ECRH and ICRH). Another method is the injection of high-energy neutral particle beams, that may enter the plasma without being disturbed by the magnetic field. When colliding with plasma particles, these fast neutrals become ionized and distribute their energy via Coulomb collisions. This is known as neutral beam injection (NBI).
Due to the inductive nature of the transformer, only pulsed operation is possible for a tokamak, although there are experimental efforts being made to maintain the plasma current by non-inductive current drive. An advantage of the tokamak is its axisymmetric configuration, where generally all plasma parameters and the magnetic field do not depend on the toroidal coordinate. Furthermore, start-up plasmas can be heated ohmically. However, there are current-related instabilities and disruptions, that may lead to a fast collapse of the plasma. Disruptions may lead to very high local heat loads on wall components and extreme forces on the machine, having the potential to damage them. A particular issue are run-away electrons, that can be generated during disruptions. A disruption may arise if a stability limit is reached, and the plasma interacts with the wall and cools down. In that case, plasma resistivity increases and a large electric field is induced, trying to maintain the plasma current. Fast electrons in the tail of a (Maxwellian) velocity distribution make very few collisions. Due to the low collision frequency $\nu_{ei} \propto 1/v^3$, that is decreasing with increasing relative velocity between colliding particles (as for the plasma resistivity). In case of a loop voltage, a few of the fast electrons in the direction of $-\vec{E}$ gain so much energy before encountering an ion that they decrease their collision probability even more. If the electric field is large enough, they might never make a collision, practically forming an accelerated electron beam ([11], p.170) that can damage wall components.

The second concept with a twisted, toroidal magnetic field shape is the stellarator. Stellarators generate their entire confining magnetic field only externally and therefore can operate without a toroidal plasma current. The lack of a plasma current allows for continuous plasma operation, but comes at the price of a more complex, three-dimensional magnetic field topology. Because there is no net plasma current, stellarators do not experience many of the instabilities that can occur in a tokamak.
In the several decades of magnetic confinement fusion research up to today, many plasma instabilities and transport mechanisms have been discovered and investigated. Plasma transport is usually distinguished into two directions: parallel and perpendicular to the magnetic field lines. There are many phenomena that result in perpendicular transport of particles and energy, leading to a radial loss of both, out of the confined volume. Radial as well as parallel transport can be caused by particle collisions (which is referred to as *classical*). Additional forces arise due to the geometry of the magnetic confinement topology such as drifts (termed *neoclassical* when included). In tokamaks, it is observed that the transport of heat and particles often exceeds the neoclassical predictions. The difference between the observed transport and predicted neoclassical values was named *anomalous*. Anomalous transport is now believed to be caused by micro-instabilities driving turbulence. For later fusion reactors, the radial

transport of heat needs to be suppressed while e.g. impurities such as the fusion α-product need to be transported out of the core after they have thermalised. Achieving transport to its neoclassical value is one of the main issues of fusion research.

1.3 Divertor and exhaust concept

In order to deal with heat and particles radially transported out of the hot plasma core to the edge areas, the limiter and divertor concepts have been investigated in many experimental devices. They are designed to be the only components that interact with a part of the colder edge plasma by e.g. sputtering. They are made of specific materials that can withstand high local heat loads. Figure 3 shows an overview of the two basic concepts.

The plasma is divided into two areas: a confined and a non-confined area. The confined area is

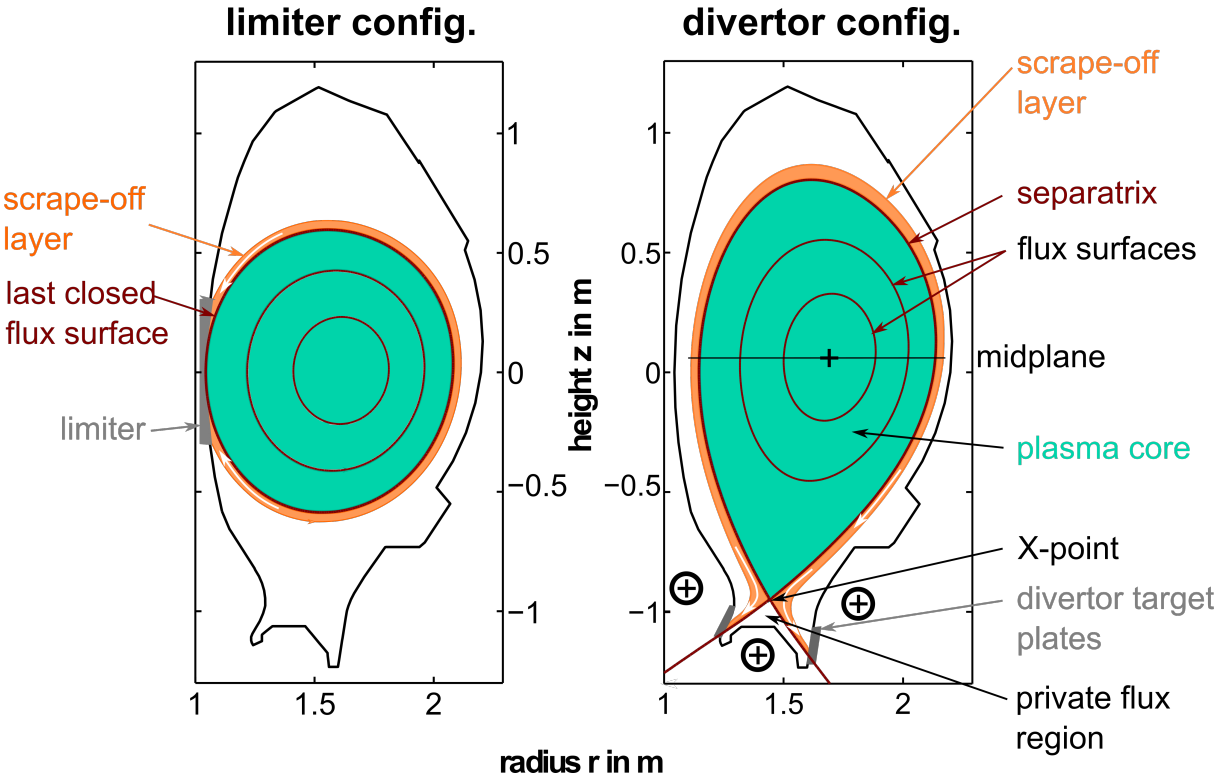

Figure 3 – The limiter and divertor concept for plasma exhaust. The schematics show poloidal cross-sections of the first wall of the ASDEX Upgrade tokamak as well as a Poincaré plot of the magnetic field. The confined plasma area is shaded turquoise, the plasma exhaust flows in the non-confined area are indicated with white arrows.

defined by the twisted magnetic field lines that indefinitely travel inside the plasma. They form magnetic flux surfaces that are characterized by constant magnetic flux and (when neglecting toroidal rotation) equal plasma pressure. An example of such a surface can be seen in Figure 2 in dark red. In the non-confined area, the magnetic field lines contact the wall at some point. Whenever plasma particles enter the non-confined edge area, they quickly hit the target plates that are touched by the open magnetic field lines. The plasma temperature is relatively low in this area, usually in the range of 1-100 eV. The non-confined and confined volumes

are separated by the last closed magnetic flux surface (LCFS), also referred to as separatrix in diverted topologies. The midplane is the horizontal plane in the poloidal cross-section that is at the height of either the geometric or the magnetic axis.

If the confined plasma volume is simply limited by a protruding object, then this is called a limiter configuration. An example of this can be seen in the left part of Figure 3. On the limiter surface, that can be made of a material with very high heat conductivity and low sputtering yields, the plasma exhaust is 'scraped off' before reaching the other parts of the wall. The large majority of the plasma exhaust is inside the so-called scrape-off layer (SOL) travelling to the limiter. This has the advantage that the majority of the surrounding chamber wall does not interact with the plasma edge. Furthermore, limiters are relatively easy to implement. However, with the limiter configuration, wall impurities e.g. sputtered from the limiter surface may enter the plasma relatively easily.

The term **divertor** denotes a specific magnetic field configuration in combination with a set of target plates adapted to this configuration. In contrast to a limiter plasma, some magnetic field lines of the divertor configuration are intentionally directed to target plates (cf. Figure 3). This is achieved via one (or several) additional field coils behind the first wall (in black), than run a current in the same direction as the plasma current. This generates a magnetic field with an X-point in the poloidal plane of the magnetic field topology. The X-point is characterized by the poloidal field being zero.
The divertor concept moves the plasma-wall interaction zone further away from the hot core plasma in order to avoid fast penetration of wall impurities and neutrals into the confined volume. Impurity control is very important during plasma operation, since the accumulation of impurities in the confined plasma volume may lead to large plasma heat losses due to radiation. Sources of impurities will be discussed in more detail in chapter 7.
The higher the input power of the plasma experiment, the higher the plasma exhaust will become. The SOL close to the separatrix is characterized by large power and particle fluxes. Since the field lines inside the SOL are open and have lengths on the order of 10-100 m in many present-day devices, much more particles are lost parallel to the magnetic field lines in the SOL before they are radially transported in significant amounts. Usually, this leads to a strong peaking of the power and particle fluxes around the separatrix, forming strike-lines on the divertor target plates where the separatrix contacts the plates. Due to the magnetic field anisotropy, the strike-lines have very high local heat loads. The broadening of the strike-line areas is dependent on the radial transport coefficients in the SOL. In many present plasma experiments, divertor target plates are designed to withstand high heat loads on the order of $10\,\mathrm{MW/m^2}$. However, in future, larger devices, even higher heat loads are expected that cannot be dealt with by the target plate materials any more. By careful arrangement of the magnetic field configuration, certain plasma parameters and the target plates, significant reduction of

the target power density can be achieved. This will be explained in more detail in the next chapter. Furthermore, with high density of neutral particles close to the target plates, efficient particle pumping is possible in the divertor region. This is accomplished by pumps below the target plates. In a future reactor, the helium ash of the fusion reaction could be removed in the divertor.
With divertors, radiation scenarios also become possible. A radiation scenario can be introduced by the intentional puffing of low-Z impurities into the SOL (such as nitrogen or neon). Low-Z elements mainly radiate energy at low temperatures. This is a desired scenario in the SOL, to decrease heat fluxes to the divertor target plates by radiation in the SOL.

There a different forms of divertors, a prominent one in tokamaks being the **poloidal field divertor**. A poloidal field divertor has a continuous toroidal magnetic X-Point topology. The exact arrangement of the target plates and the magnetic field of poloidal field divertors varies a little from experiment to experiment. Conventional poloidal field divertors are sufficient for the expected heat flows in ITER, however for larger reactors, the heat and particle loads might be too high. Therefore, further advanced divertor designs are under development, namely the Super-X divertor (tested in MAST-Upgrade) or the snowflake divertor (NSTX-Upgrade). In stellarators, helical divertors or magnetic island divertors are used [12].

The use of divertors has proven to be essential for good plasma operation. They are not only a promising solution for particle control and heat removal in future fusion devices, but also have important implications on the plasma core properties ([13]). The most important discovery made with a divertor is the High-confinement mode (H-Mode), a regime of improved core energy confinement that suppresses turbulent transport in the plasma boundary. Although, later, H-Mode could also be achieved in limiter plasmas ([14]), the confinement improvement in limiter H-Modes is lower and the power threshold to obtain the H-Mode higher. In the stellarator Wendelstein 7-AS, a high-density high-confinement mode (HDH-Mode) could be observed after the installation of a divertor [15]. Many plasma experiments have accomplished their highest densities, temperatures and confinement times with a divertor. Today, all larger plasma experiments (e.g. ITER, JET, JT60-SA, ASDEX Upgrade, DIII-D, LHD, W7-X...) operate or are designed to operate with divertors.

1.4 Particle flow diagnostics

The physics of the plasma edge and boundary are more complicated with divertors, due to the more complex divertor geometry. One goal of this work is the better understanding of the SOL and divertor physics, which is necessary e.g. for the development of simulation codes and the design of future fusion devices. There are many diagnostics concerned only with the measurement of plasma parameters in the edge. Physical phenomena differ significantly between the plasma core and edge, as well as the range of plasma parameters. The understanding of SOL

and divertor dynamics is crucial to find a reliable solution for the plasma exhaust.
With conventional plasma diagnostics such as Langmuir probes, bolometers or pressure gauges, electron density and temperature, radiated energy and neutral gas pressure are determined in the plasma SOL. A parameter of key interest is the plasma flow, which is currently not completely understood but plays an important role in the particle and heat transport in the SOL. SOL flows are also reported to interact with the core plasma (flows), mainly by friction and viscosity [13]. Furthermore, particle flows on the divertor help to determine the material erosion and (re-)deposition on the target plates.

Doppler coherence imaging spectroscopy (CIS) is a relatively new diagnostic for the measurement of particle flows [16]. It measures the Doppler wavelength shift of atomic emission lines from radiating particle species in the plasma. Differently from conventional spectroscopy systems (e.g. using a spectrometer), it does not perform a frequency domain measurement of the spectrum, but uses an imaging interferometer to perform narrow-bandwidth Fourier transform spectroscopy. This will be explained in more detail in chapter 3 of this thesis.

There are several, well established diagnostics for measuring particle flows in the plasma edge. Compared with the Doppler CIS, they have some disadvantages, but also advantages. A brief overview is provided here:

- **Doppler Spectroscopy** In all radiating areas of the plasma it is possible to measure the spectral function of neutral or partly ionized particles. For low-Z species, visible radiation usually occurs in the low-temperature areas of high-temperature plasma experiments, such as the divertor and SOL. For higher Z numbers, particles also emit visible radiation at higher temperature regions, e.g. inside the last closed flux surface. Optical fibres are typically used to transmit light from the plasma to one or several spectrometers, that may be placed at a large distance from the machine, e.g. in a separate laboratory. Usually, the plasma light is collected with collimation lenses inside a viewing port of the experiment. In the spectrometer, diffraction gratings are used to measure the intensity spectrum e.g. on a CCD chip. Depending on the wavelength resolution, ion flow velocities on the order of km/s may be deduced from the Doppler wavelength shift of the recorded emission lines.
  Doppler spectroscopy is a common method to measure ion velocities in the plasma core, usually with higher-Z impurities such as Argon. Furthermore, there are also spectroscopic applications in divertors ([17]), which require higher wavelength resolution. Doppler spectroscopy has the advantage of measuring several ion or neutral species at once, however only as line-integrated measurements.

- **Mach probes:** Mach probes are usually a set of several negatively biased electrical probes that are inserted into the plasma. The simplest set-up are two probes that are applied

on opposite sides of a pin or mounting and insulated from each other. This allows for a separated measurement of the incident ions in opposite directions by the two probes (the electrons are repelled by the bias voltage). If there is a net plasma flow in the direction of the geometrically separated probes, the collection current on the upstream side will collect a higher ion flux than on the downstream side. The ion flow can then be deduced by the current ratio of the two probes. The ratio is equivalent to the ratio of the flow velocity to the ion sound speed (the Mach number). This is why these probes are referred to as Mach probes ([18], p.82).
Mach probes are usually applied for ion flow measurements in the SOL and divertor regions of plasma experiments ([13], [19]). They are sometimes used in combination with Langmuir probes for providing simultaneous electron pressure and ion flow measurements. They can measure the flow velocity of fully ionised particles, that do not radiate and therefore cannot be measured with spectroscopic techniques. However, it is not possible to separate different ion species that hit the probes. The presence of impurities changes the measured mach number. For an accurate measure of the main plasma flow, Z_{eff} is necessary, requiring detailed analysis or modeling involving other diagnostics.

- **Laser-induced fluorescence (LIF):** The LIF diagnostic uses a tunable laser source to excite a specific atomic state in the electron shell of a plasma particle. Due to the small lifetime of the excited state a discrete atomic line is instantaneously emitted. The density dependent line intensity is measured and amplified with a photo multiplier, that has a narrow-bandpass filter in front of it. Since the laser is chopped, the laser-induced and the natural fluorescence can be differentiated.
  The pick-up optic measures along a line-of-sight that crosses the laser beam in one point. This enables a non-invasive and local measurement of the laser-induced fluorescence signal. The laser wavelength can be tuned on scales on the order of 0.1 pm, allowing an accurate measurement of the spectral intensity function of even narrow plasma emission lines. The spectral function is dependent on several broadening effects (such as Zeeman splitting or Doppler broadening) as well as the Doppler shift of the spectral line. Thus, the LIF diagnostic can be used for local and accurate measurements of the ion temperature of even less than 1 eV, the ion velocity, with an accuracy on the order of less than 100 m/s, and the density of the excited state. However, one complete wavelength scan can require up to several minutes.

These three diagnostics have in common that they measure the plasma flow at a single position or along a single line-of-sight. To measure flows simultaneously at multiple positions in the SOL, several of them have to be applied. This is not always easy to achieve. An example of such a measurement, that used Mach probe flow data from several positions in similar tokamaks, is presented in ([20]).
With the Doppler CIS, 2D images of the plasma are taken that reveal the flow velocities in the

illuminated areas of the image. Thus, a huge amount of spatial information is taken, enabling it to gain a better overview of the flows in a divertor configuration for many time slices.
The Doppler CIS has been applied for plasma ion flow measurements (MAGPIE [21], WEGA [22], HN-1 ([23])) as well as for (impurity) scrape-off layer and divertor flows in several toroidal plasma experiments (MAST [24], TEXTOR ([25]), DIII-D, CTH). It is a useful diagnostic for the observation of ion flows in the divertor, where the boundary plasma is in contact with the wall and high radiation intensities occur due to the low plasma electron temperatures. In contrast to Mach probes, the Doppler CIS allows to observe different ion species separately. However, like all spectroscopic systems, it is restricted to ions and neutrals that radiate, which is not the case for fully-stripped ions, the main component in most plasma experiments. The bulk plasma species in many high-temperature plasma experiments are usually either completely ionized hydrogen isotopes or helium.
The Doppler CIS has been applied to measure velocities in the range of 30 km/s down to 100 m/s. These low flows can also be measured by e.g. the LIF laser diagnostic, that provides the advantage of measuring the entire spectral function over the Doppler CIS, however, it needs a far larger measurement time than the Doppler CIS. The preferred resolution of the Doppler CIS can be adapted relatively easily.

In the following chapter, the flow dynamics and the relevant general edge physics are explained in more detail. In chapters 3 and 4, the theory behind Doppler coherence imaging and the set-up will be discussed. The subsequent three chapters cover the measurement results achieved in the frame of this work, which include performance tests (chapter 5), Doppler CIS measurements in the small, low-temperature plasma experiment VINETA.II (chapter 6) and the medium-sized tokamak ASDEX Upgrade (chapter 7). The last chapter provides a summary and some key conclusions of this work as well as an outlook for a future Doppler CIS on W7-X.

2 Ion dynamics in magnetic plasma experiments

The general idea of magnetic confinement devices is to strongly magnetize plasma particles in order to minimize losses of the main plasma particle species (D and T in later fusion reactors) and heat from the core. A magnetized plasma is characterized by the plasma particles having a higher gyration than collision frequency. Transport perpendicular to the magnetic field lines needs to be small. The ratio of perpendicular and parallel transport is an important characteristic for magnetic confinement experiments, both in the core of a plasma (where it defines the thermal insulation quality for the nuclear fusion process) and in the SOL, where it strongly influences the exhaust power deposition on the wall.

This chapter aims to give insight into the thermal ion dynamics in the SOL and divertor regions of tokamaks. It investigates SOL and divertor physics from the viewpoint of bulk flows for different particle species. There is a large number of processes that influence or cause plasma and impurity flows in the SOL.
The SOL and divertor are defined by open magnetic field lines. They are supposed to distribute the plasma exhaust in a controlled way onto special target plates as well as to prevent wall impurities from entering the core plasma. Generally, plasma regions with open magnetic field lines are characterized by low temperatures. Some ion dynamics and other plasma parameters connected to low-temperature plasmas will be shortly discussed for better understanding of the Doppler CIS measurements conducted in ASDEX Upgrade and VINETA.II. The focus of interest is on two essential geometries: a linear magnetic plasma experiment and the tokamak SOL with a poloidal field divertor. Although designed with quite different intentions, both of these geometries share some similar features, e.g. radial electric fields or the existence of the walls, that are intersected by magnetic field lines. The walls have a dominating effect on the plasma particles, since they e.g. impose sheath potentials, induce parallel loss channels or particle recycling. Recycling refers to plasma particles that become neutralized at the material surface and re-enter the plasma as neutrals.

Plasma flows in the SOL play an important role in the heat distribution of the plasma exhaust as well as the impurity transport inside and outside of the divertor. Asymmetries in the inner and outer divertor power loads are related to SOL drifts. There are some further indications that SOL flows have direct effects on plasma core confinement properties ([13]), such as through the transition from the low confinement mode (L-mode) to high confinement (H-mode) (also referred to as L-H transition). A comprehensive overview of the SOL flows will be presented. The chapter begins with a short overview on sheath physics and their related flows (which arise close to target plates intersected by magnetic field lines), followed by the generation of a radial electric field in a linear (open) magnetic field topology. The so-called divertor regimes, which are characterized by certain plasma parameter ranges will also be

discussed.

2.1 Plasma wall sheath

In the presence of a wall or an object in a plasma, a stationary potential sheath is formed directly above the surface of the object material (cf. Figure 4). Generally, three different sheath regions are present:

1. an electrostatic sheath, a region of net charge, where $n_e < n_i$ and the plasma is not quasi-neutral.
2. a magnetic presheath in the presence of magnetic field lines that are not perpendicular to the wall surface. Ions become non-magnetized here due to the large electrostatic forces.
3. the (quasi-neutral) presheath region

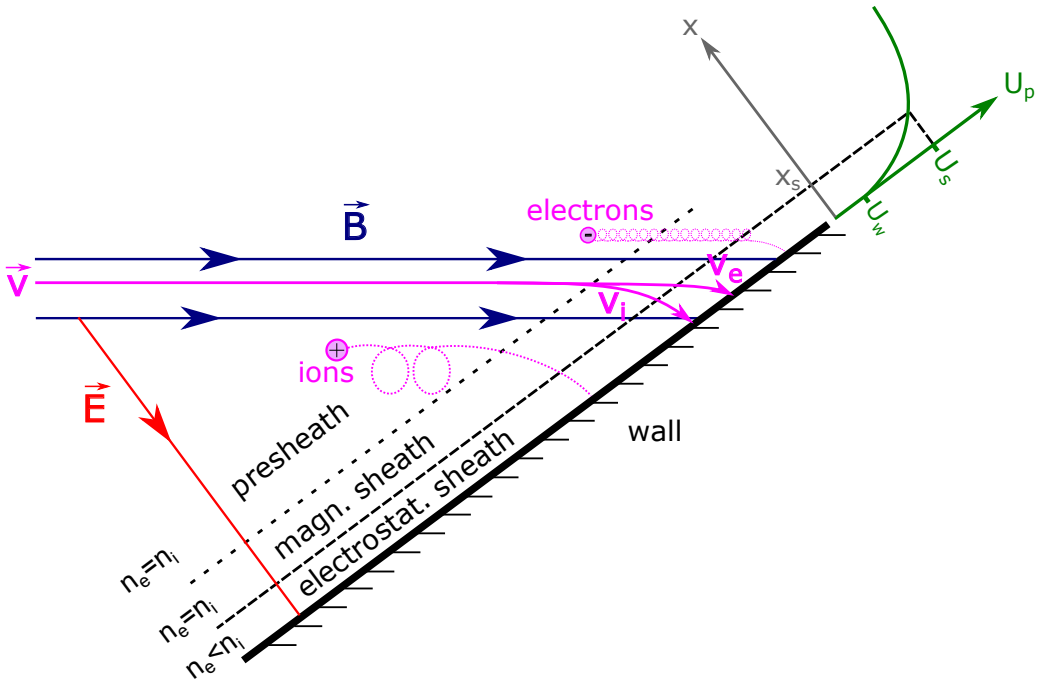

Figure 4 – Plasma wall sheath in the presence of a magnetic field. The position of the plasma-sheath transition location, x_s, in a magnetic field is under debate [26]. It is uncertain if the magnetic presheath should be interpreted as an additional presheath which accelerates the ions or not. Illustration after Figure 4.16 in ([27]).

Inside the sheath, a positive net charge is formed since the electrons travel much faster than the ions due to their low mass. According to the Poisson equation, a local (negative) plasma potential U_p is generated by the charge difference:

$$\frac{\mathrm{d}^2 U_p}{\mathrm{d}x^2} = -\frac{\rho(x)}{\epsilon_0} \tag{4}$$

where $\rho = e \cdot (n_i - n_e)$ is the charge density distribution. There is an electrostatic wall potential, U_w, which is sufficient to inhibit the free (Maxwellian) electron outfluxes [28]. The ions are accelerated towards the wall by this potential, whereas electrons are slowed down. The acceleration or deceleration is already initiated in the presheath. The electrostatic wall potential is proportional to $k_B T_e/e$ (there are different scalings for different plasma species, for hydrogenic species it is $3 \cdot k_B T_e/e$ ([28], p.48)).

.

Since the sheath electrons find themselves in a repulsive, i.e confining electric field, they suffer slow losses. As a result, the electron distribution is approximately Maxwellian and the electron density at each point in the sheath decreases according to a Boltzmann factor:

$$n_e(x) = n_{e,s} \exp\left[\frac{e(U_p - U_s)}{k_B T_e}\right] \tag{5}$$

This is known as the Boltzmann relation. U_s marks the potential at the transition point between presheath and sheath, x_s. From energy conservation ($\frac{1}{2} m_i v^2 = -eU$) and particle conservation ($n_i v =$ constant), the ion density can be described as well: $n_i = n_{e,s}\sqrt{U_s/U_p}$. Inserted into the 1D Poisson Equ. 4 together with Equ. 5, the so-called Bohm criterion for the sheath is derived (the detailed derivation can be found in e.g. [28], p.72). It states that in the sheath, the plasma ion fluid velocity may be equal to or exceed the (isothermal) sound speed, c_s:

$$v_{\mathrm{ion},s} \geq c_s \tag{6}$$

A stationary sheath can only exist if the Bohm criterion is fulfilled. The Bohm criterion is only valid in collisionless conditions (free mean path length of ions needs to be larger than x_s). The thermal ion sound speed is

$$c_s = \sqrt{\frac{k_B(T_e + T_i)}{m_i}}. \tag{7}$$

All ions crossing the sheath edge are accelerated, reach the surface and become absorbed. By the ion acceleration and electron deceleration, the ion loss rate becomes equal to the electron loss rate (this is defined as ambipolar plasma transport) and an ambipolar electric field arises in the sheath plasma ([28], p.27). The ions are monotonically pre-accelerated by a non-shielded residual field in the quasi-neutral "presheath" region. There, additional weak electric fields may arise due to collisional ion friction, ionization or magnetic deflection of the ion orbits [29].

In the presence of $\vec{B}$ hitting the wall obliquely, a magnetic presheath is formed. In this additional sheath, the ion orbits are magnetically deflected. This is the case in limiter as well as divertor configurations in fusion experiments. Since an oblique magnetic field points into a different direction than the sheath electric field, different ratios of electric and magnetic forces for ions and electrons lead to different ion and electron particle dynamics. The magnetic Lorentz

force is less for ions, since they move more slowly than electrons (except for $T_i \gg T_e$) and have much larger Larmor radii, $\rho_i = m_i v_\perp/(eB)$. In the presheath, the ions are magnetically confined, because the electric field $\vec{E} = -\vec{\nabla} U_P$ is still weak. However, in the magnetic sheath, the ions are deflected and no longer magnetized since their motion is dominated by the electric field. Depending on the collisionality and ionization, they might become accelerated to sound velocity before entering the electrostatic sheath. The electrons, with their much smaller mass and Larmor radius, remain magnetized and un-deflected in the magnetic presheath.
The magnetic presheath is intrinsically controlled by elementary collision processes and has a characteristic length scale of the ion gyro radius ([26]).

The electrostatic sheath length is on the order of a few Debye lengths $\lambda_D = \sqrt{\frac{\epsilon_0 k_B T_e}{e^2 n}}$. For many plasma experiments, these produce relatively thin sheaths on the order of 10^{-4} to 10^{-6} m. The magnetic sheath is quasi-neutral and has a width of a few ion Larmor radii. The Larmor radius in e.g. VINETA.II is on the order of 10 mm for the singly ionized argon plasma particles, whereas in ASDEX Upgrade, it is about 0.1 to 1 mm in the SOL (for deuterium ions). Thus, the Debye sheath is usually smaller than an ion Larmor radius.

2.2 Wall-limited linear plasma devices

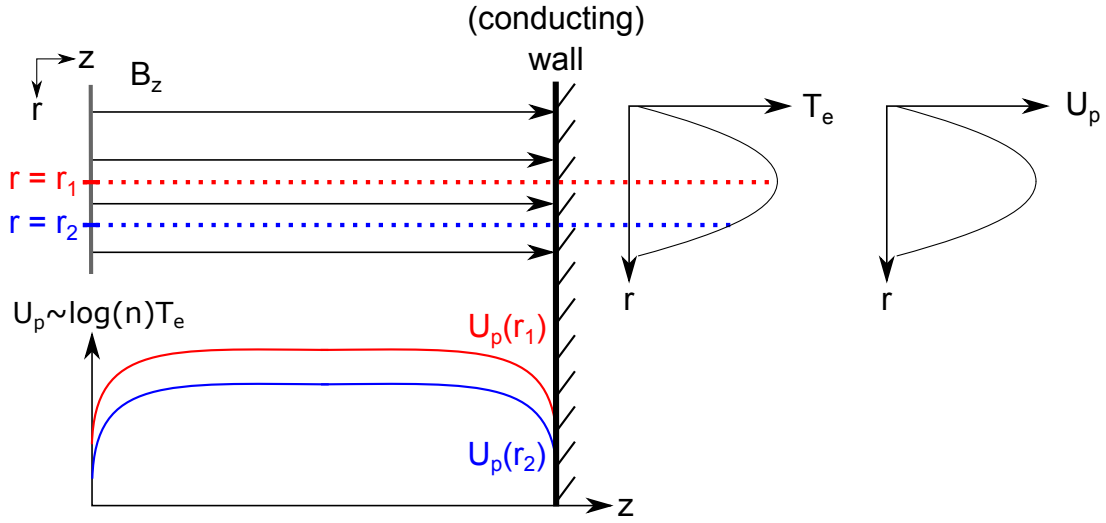

Figure 5 – Potentials evolving in a wall-limited, linear magnetic field plasma experiment. The electron temperature T_e varies perpendicular to the magnetic field lines, e.g. given by the heating source energy distribution.

The previous subsection revealed how an electrostatic potential $U \propto T_e$ is formed directly in front of an object in a plasma experiment. In the case of a wall-limited magnetic plasma experiment, parallel as well as perpendicular electric fields can arise (parallel and perpendicular to the magnetic field lines). This is shown in Figure 5, where a linear magnetic field ending perpendicular on a wall is illustrated. Between the two walls, a parallel sheath potential and associated electric field ($\vec{E}_z = -\vec{\nabla} U_p$) arises, as was explained in the previous subsection. The

higher the electron temperature T_e at a certain radial position r ($\vec{r} \perp \vec{B}$), the higher the evolved plasma potential $U_p(r) \propto T_e$ will become, in accordance with the Boltzmann relation 5.
For a radially varying electron temperature and density, another plasma potential evolves in the radial direction. Electron temperature and plasma density gradients can be present in linear plasma experiments due to the energy deposition profile of the heating source.
The evolved radial electric field E_r can, by inserting Equ. (5) into $\vec{E} = -\vec{\nabla} U_p$, be described as follows:

$$E_r \propto -\frac{k_B}{e} \nabla_r T_e. \tag{8}$$

The resulting E_r varies strongly with the electron temperature gradient scale in different experiments, from just a few V/m in wall-limited, linear experiments like VINETA.II up to a few kV/m in the SOL of a tokamak. They will lead to azimuthal $\vec{E} \times \vec{B}$ flows.

2.3 Divertor regimes

There are many mechanisms and processes that determine the plasma and impurity ion dynamics in the SOL and divertor. An already mentioned example is the radial electric field. Further flow drive mechanisms will be explained in more detail in the next subsection. Most of these drivers are strongly dependent on SOL parameters (some are also dependent on core parameters). Therefore, an overview on the SOL and divertor parameter ranges will be provided in this subsection.

Basic SOL and divertor plasma parameters such as density and temperature are found to vary strongly for different operational settings in the divertor. But their variations can be categorized, since there is a general correlation between e.g. the plasma density and the temperature ([30]). These parameter categories are referred to as divertor regimes, that were discovered in tokamaks early during the first applications of divertors ([30]). Each regime is generally characterized by a different temperature and plasma density profile along the magnetic field lines. The profile of T_e and n_e is crucial for understanding SOL flows, plasma radiation or the radial electric field structure in the SOL and divertor. The resulting forces acting on the plasma particle species and flow patterns in the poloidal divertor topology will be presented in the next subsection.

The basic idea of the divertor is to move the plasma-wall interaction zone away from the confined plasma which has three main advantages:

1. Better impurity and neutral control, since the impurities first have to travel along the open SOL field lines to penetrate the core by cross-field transport and neutrals from the target plates have a longer distance to the core.

2. Impurities in the divertor can radiate energy in the form of light, decreasing the local

heat load on the target plates. Additionally, with a high neutral density in front of the target plates, the heat loads can be further reduced.

3. Efficient pumping is possible.

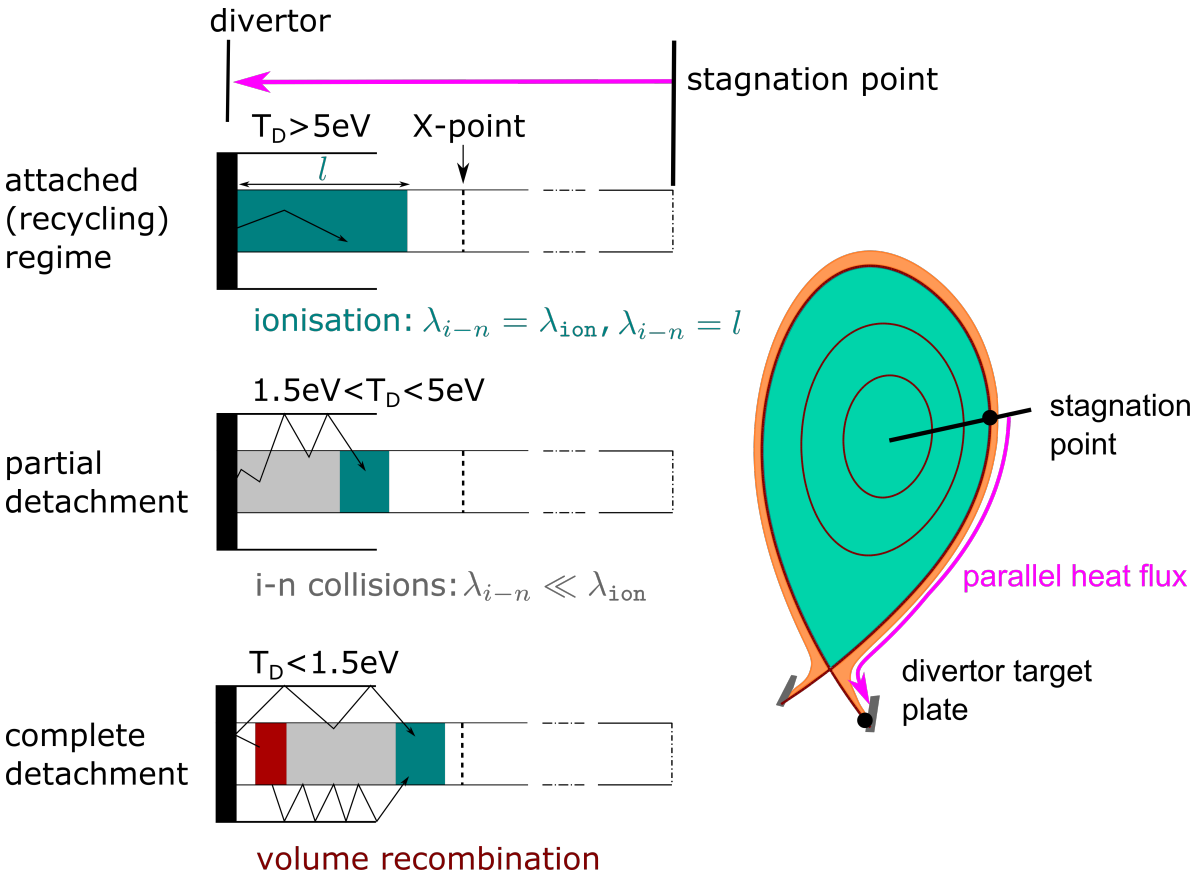

Figure 6 – Simplified overview of different divertor regimes, as e.g. used in the 2-point model ([31]). Physical properties between the flow stagnation point on a field line and the target plate are characterised. The position of the flow stagnation point in the SOL is variable, usually it is near the outer midplane due to transport asymmetries into the SOL and drifts. The jagged black arrows indicate the paths of neutral particles before being ionized. Left schematics drawn from illustrations in ([27], chapter 7).

Different divertor regimes are characterised by different plasma temperature profiles and neutral trajectories in front of the target plates. An overview of the three most important regimes is provided in Figure 6. The regime names are referring to the state of contact between the SOL plasma and the divertor wall (attached, partially or completely detached). Generally, for decreasing plasma (electron) temperature in the divertor, T_D, the SOL plasma becomes more and more detached from the divertor plates, due to an increasing neutral density and hence collisions in front of the target plates. Lower divertor electron temperatures can be achieved by increasing the overall gas density in the SOL (for a fixed power input) or intrinsic as well as extrinsic low-Z impurities, that radiate and cool the divertor plasma. The critical temperatures for the domination of either the ionisation, charge exchange (CX) or recombination process depend on the respective collision cross-sections of the plasma particle species (the temperatures

in Figure 6 refer to a hydrogen plasma).

In the case of an attached regime, the divertor plasma temperature directly in front of the targets is relatively high ($T_D \gg 5$ eV) and both ionization of neutral particles and recombination of plasma particles are small in the divertor. The overall SOL density is low and a large number of recycled neutral particles reach the SOL upstream. Cross-field transport from the main plasma across the separatrix is the main source of plasma particles in the SOL. Typically, a flow stagnation point is observed close to the outer midplane due to asymmetrical cross-field transport. Plasma particles flow downstream to the target plate and are accelerated to sound speed at the target to meet the Bohm criterion. One may divide the attached state into low- and high-recycling regimes. They are characterized by different neutral mean free path lengths, λ_{i-n}. In the low-recycling regime, the neutral particles from the target plate may penetrate deeply into the SOL (even above the X-point), where they are eventually ionized. This changes in the high-recycling regime, where the divertor density is increased due to a higher upstream density and λ_{i-n} decreases, becoming smaller than the divertor dimensions. The overall collisionality becomes larger in the high-recycling regime, increasing friction forces, decreasing the temperature and leading to an almost complete re-ionization of recycling neutrals close to the target plate [27]. The finite plasma thermal conductivity leads to larger parallel temperature gradients. Due to the high ionisation rate of neutrals in the divertor, ionised recycling neutrals are the dominant particle source in the divertor SOL.

Partial detachment resembles the high-recycling regime, however the energy flux to the divertor plates is reduced by about one order of magnitude ([27]). In front of the target plate, a zone of low divertor temperatures of $1.5 < T_D < 5$ eV is established by increasing the upstream density further. In the low temperature zone, the particle flux momentum is decreased due to an increased number of CX collisions.

The last regime is the complete detachment scenario, where a recombination zone is generated in the vicinity of the divertor target plates. The energy and particle momentum flux is almost completely lost before the plates. The high plasma density zone is moved further away from the divertor plates and the mean free path of the neutrals is increased, compared to the partial detachment regime. In order to meet power exhaust requirements, future divertors will have to operate in partial to complete detachment to reduce the particle and heat fluxes to the target plates by volumetric losses. However, in AUG with its full tungsten wall, additional seeding is required for strong detachment at the outer divertor target as the H-mode density limit is reached before strong detachment is achieved and an H-L back transition occurs before detachment of the outer target[32]. With strong additional impurity seeding completely detached H-modes with the full-tungsten wall could be achieved with stable X-point radiation ([33]).

2.4 Ion flows in the plasma SOL of a tokamak

In this subsection, different mechanisms driving plasma ion and impurity flows are described to gain a picture of plasma transport in the SOL of a tokamak divertor. The overall aim of this chapter is to understand and categorize SOL physics and phenomena from the viewpoint of bulk flows. It is necessary to distinguish the main plasma ion flow from impurity and, obviously, neutral particle flows, since they have different drive mechanisms and sources.

Many flow measurements have shown strong (near-sonic) parallel plasma flows in the SOL of tokamaks with poloidal field divertors (e.g. [13],[19],[20],[24]). Flows approaching or exceeding the local sound speed are expected on a short characteristic length scale (ion Larmor radius) of a field line ending on material surfaces due to the Bohm criterion. But they are also observed in regions further away, e.g. in the proximity of the X-point further upstream ([13]), or even in the crown (top) of a single-null magnetic field topology, opposite to the X-point ([34]). At these positions, they are largely independent of any sheath potential near material surfaces [13]. There is a large variety of drive mechanisms for plasma and impurity ion flows parallel as well as perpendicular to the magnetic field lines in the SOL and divertor. The flow pattern structure might also change for different plasma SOL parameters, i.e. for different divertor regimes. This subsection aims to give a comprehensive overview on them.
There have been many studies investigating the ion flows in the SOL by experimental means, e.g. Mach probes ([13], [35], [19]) or spectroscopy ([17],[24]), but also with simulation codes ([36],[37],[38]). In these studies, several mechanisms are reported to cause large flow speeds in the SOL:

1. a poloidal SOL pressure asymmetry as important drive mechanism for the (parallel) main plasma flows according to ([13],[20]).
2. classical drifts such as $\vec{E}_r \times \vec{B}$, $\vec{E}_\theta \times \vec{B}$ or $\vec{v}_{\mathtt{dia}} = -\vec{\nabla} p \times \vec{B}/(qnB^2)$ ('diamagnetic drift'), that may lead to perpendicular plasma and impurity ion flows.
3. secondary parallel plasma flows can be generated by Pfirsch-Schlüter ion currents or the overall toroidal rotation of the plasma.
4. the balance of thermal and friction forces, that determine parallel impurity ion divertor flows, dependent on the divertor parameters and the main plasma flow speed.

Each of the above listed physical drive mechanisms will be described in more detail in the next paragraphs. Next to these drive mechanisms, plasma flows are also found to be very sensitive to the magnetic separatrix topology (upper-, lower- and double null), with flow magnitude and direction strongly dependent on it [13]. However, in the following, emphasis will be put on a lower single null magnetic field topology only. An overview of the flow changes induced by different magnetic field topologies can be found in ([13]).

Poloidal transport asymmetries

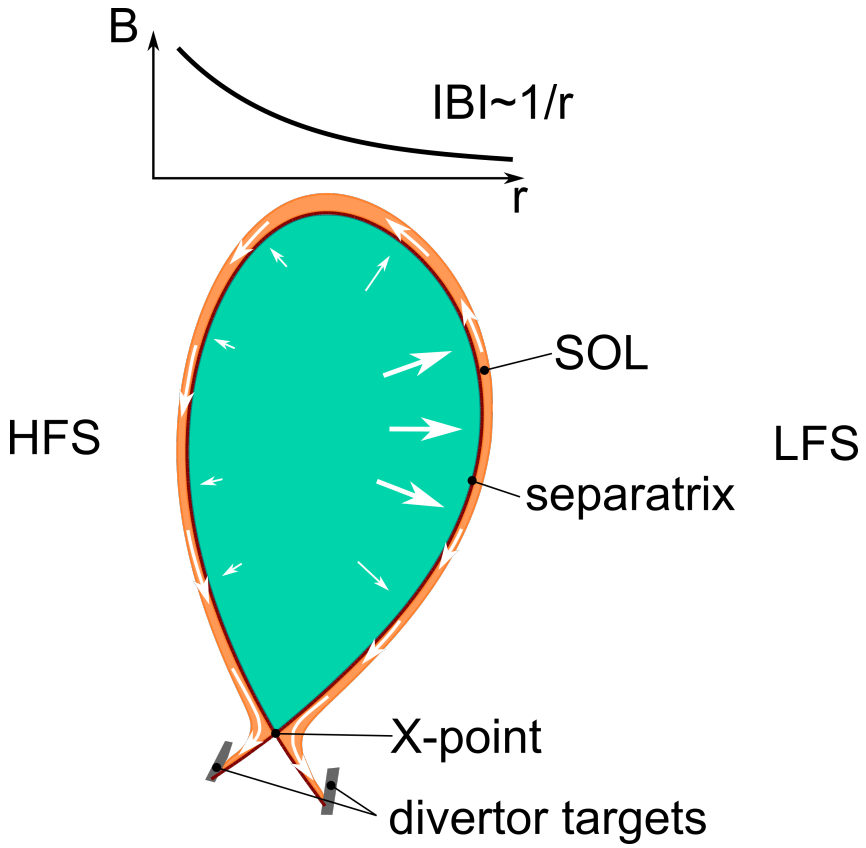

Figure 7 – Flows in the SOL and divertor regions (orange) are driven by transport phenomena in the plasma core (turquoise).

Poloidally asymmetric radial plasma transport out of the core and the divertor sink action causes a pressure asymmetry in the SOL. This leads to a flow of the main plasma species in direction to the divertor target plates on the low-field side as well as on the high-field side, illustrated in Figure 7. The poloidal transport asymmetry is sometimes also referred to as 'ballooning-like' transport (e.g. in [13]) where the word 'ballooning' refers to a pressure-gradient related plasma instability, the ballooning mode[8]. The plasma confinement is usually most unstable at the outer midplane (such as in Figure 7) due to 'bad magnetic field curvature'[9]. This is why most particles are radially transported out in the proximity of the outer midplane, also leading to the formation of the stagnation point close at this position.

The poloidal pressure variations are considered to be a major contributor to the overall SOL plasma flow, which arise to re-symmetrize the pressure ([13]). For the impurity flows that were measured with the Doppler CIS in the SOL and divertor of AUG, the plasma flow can be a major contributing drive mechanism due to friction forces (depending on the SOL parameters).

[8]The term ballooning expresses the shape and action of the instability, which acts like the elongations formed in a balloon (the plasma) when it is squeezed (the magnetic field).

[9]A confining magnetic field has a 'bad curvature' if the pressure gradient has the same sign as the magnetic field gradient. In contrast, regions of 'good curvature' are present for opposite magnetic field and pressure gradients.

Perpendicular drifts in the SOL and divertor

Perpendicular flows may arise due to curvature as well as grad-B drifts. These are in the vertical direction, either up or down depending on the direction of B and the charge sign. In most tokamaks, the ion grad-B and curvature direction is usually pointing towards the divertor (typically downwards). There is the possibility of reversing the toroidal magnetic field induced by the external coils, which results in an ion grad-B and curvature drift away from the divertor.

Perpendicular particle drifts can arise due to electric fields as well which can be produced from a number of causes in different regions of plasma experiments. Drifts caused by electric fields equally influence both impurity as well as the plasma ion species. The generation process of radial electric fields in a tokamak divertor geometry with open field lines is basically the same ([28], p.542) as in the previously discussed wall-limited, linear plasma device (cf. section 2.2) for high enough electron temperature.[10] For an electrically conducting divertor target, the plasma potential at each radial location is $U_p(r) \propto T_e(r)$. Thus, the radial electric field can be expressed in a simple approximation by the electron temperature gradient (as in Equ. (8)) or a characteristic temperature fall-off length, λ_{Te}, like ([39], p.394):

$$E_r \equiv -\frac{\partial V}{\partial r} \approx \frac{3T_e}{e\lambda_{Te}} \tag{9}$$

Usually, in attached conditions, the SOL plasma density and temperature at the target plate is highest close to the last closed flux surface (LCFS). Plasma temperatures rapidly decrease away from the LCFS into the SOL and private flux region. Therefore, the radial electric field is positive or directed outward in the SOL and private flux region (or away from the last closed magnetic flux surface) depending on the electron temperature gradient. Poloidal electric fields, E_θ, are generated by the temperature gradient along the open magnetic flux surfaces of the SOL. The poloidal electric field generates a radial drift (normal to the magnetic flux surfaces), whereas the radial electric field induces a binormal drift, that is perpendicular to the field lines, but parallel to the flux surface in the SOL[11]. Figure 8 shows an illustration of the cross-field particle drifts due to (radial and poloidal) electric fields and the ion grad-B drift. For reversed toroidal magnetic field, B_t, the magnetic and electric drifts would also be reversed.

The radial $E_\theta \times \vec{B}$-drifts drive particles from the LFS to the HFS (for ion grad-B pointing down). It is seen as one of the major reasons for plasma parameter asymmetries observed between the HFS and LFS divertor plates in many plasma experiments (e.g. [40],[41],[42],[43]). They lead to higher particle densities and thus lower electron temperature on the inboard side, resulting in different divertor regimes in the HFS and LFS (e.g. the inner side being detached

[10] In case of low temperature conditions (high collisionality and plasma resistivity), electric fields may also arise due to pressure gradients and currents.

[11] The direction indicated with the term 'poloidal' refers to a direction perpendicular to the toroidal and radial directions, thus usually not entirely perpendicular to the magnetic field lines. The term 'binormal' refers to a direction perpendicular to the magnetic field lines as well as the magnetic flux surfaces (the radial direction).

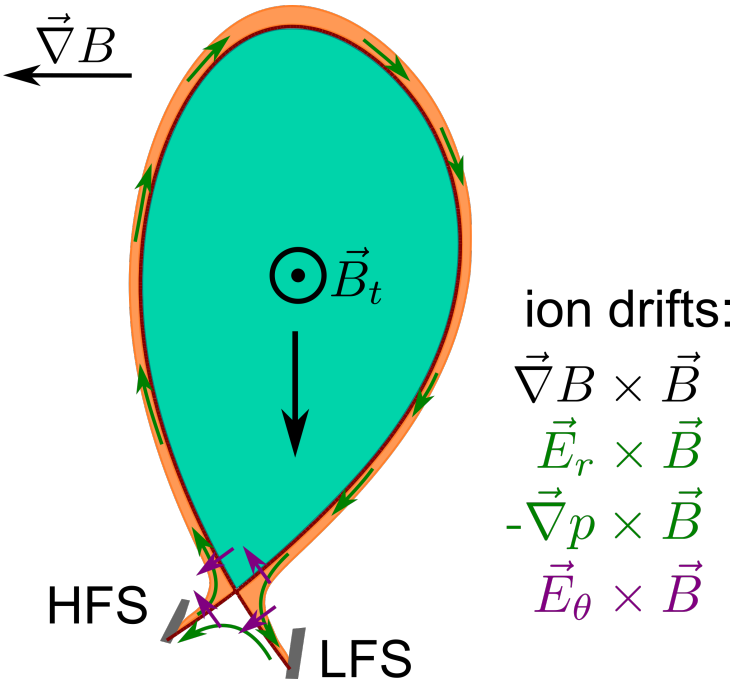

Figure 8 – Perpendicular or cross-field drifts in the SOL and divertor regions (orange) are driven by a number of causes: the gradient in the magnetic field, electric fields or due to pressure gradients (diamagnetic drift).

while the outer is attached). For reversed field configuration, dedicated experiments in JET have demonstrated that divertor energy asymmetries are strongly dependent on the sign of B, leading to a more symmetric distribution ([41]).
Due to their dependence on the electron temperature, the electric fields and their related drifts in the SOL and divertor vary strongly for different divertor regimes (cf. section 2.3) and confinement modes (L- or H-mode) ([36]). Measured poloidal and radial electric fields in the SOL and divertor are typically on the order of several hundred V/m, peaking at a few kV/m at maximum ([44],[45]).

Another source for impurity and plasma drifts are pressure gradients, that cause the so-called diamagnetic drift:

$$\vec{v}_{\mathtt{dia}} = -\frac{\vec{\nabla}p_i \times \vec{B}}{eZ_i n_i B^2} \tag{10}$$

In the region of stronger pressure, either more particles are gyrating or are gyrating faster as in the region of lower pressure, appearing as an effective net velocity.

Perpendicular impurity flows are strongly dependent on the spatial distribution of the species pressure gradients, the plasma temperature gradient as well as the electric fields in the SOL. Usually, the resulting flow speeds are smaller than parallel flows, however, for an accurate understanding of the overall impurity flows in the SOL, they are non-negligible.

Other parallel flow mechanisms

Next to ballooning-like transport asymmetries, parallel SOL (plasma) flows may arise due to diffusion and viscosity interaction with the toroidal (core) plasma rotation, presheath at the targets or ion Pfirsch-Schlüter (PS) currents.
Parallel ion PS flow can be produced due to in-out asymmetry of the (poloidal) $\vec{E}_r \times \vec{B}$- and $\vec{\nabla} p_i \times \vec{B}$-drifts in the flux surfaces [20]. The in-out asymmetry of these two drifts is caused by the dependence of the magnetic field $B \propto 1/R$ over the major radius R as well as the magnetic field geometry.
The parallel Pfirsch-Schlüter velocity is determined by:

$$v_{\parallel}^{\mathrm{PS}} = 2q \cos\theta \left(\vec{E}_r \frac{-\vec{\nabla} rp}{en} \right) \times \frac{\vec{B}_0}{B_0^2} \tag{11}$$

B_0 is the magnetic field strength at the magnetic axis at position R_0, $q \equiv rB_p/R_0B_t$ the safety factor (B_p and B_t being the poloidal and toroidal field strengths) and θ the poloidal position angle in the magnetic field topology, starting at the outer midplane. $v_{\parallel}^{\mathrm{PS}}$ is maximum at the midplane and zero at top and bottom ([28] (p.563)). Some sources ([44],[46]) state that the parallel ion flow at the outer midplane is dominated by PS flow. The PS flow direction is against the ion grad-B drift. Figure 9 illustrates the direction of the ion PS flow as well as the direction of flows due to pre-sheaths.

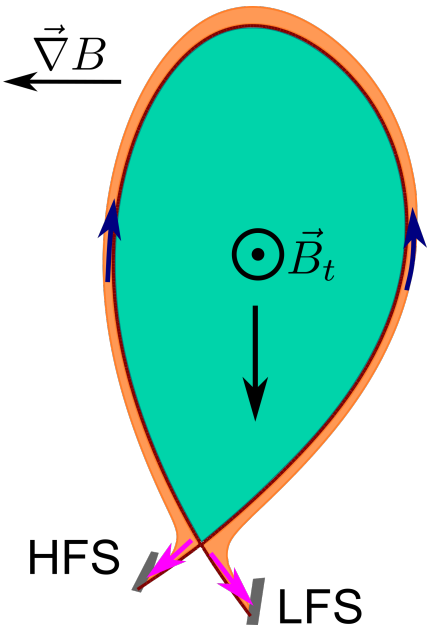

Figure 9 – Poloidal projection of secondary parallel plasma ion flow drive mechanisms in the SOL and divertor regions (orange). Blue arrows indicate ion Pfirsch-Schlüter flows. Pink arrows indicate presheath driven flows.

Divertor detachment causes momentum loss of the plasma flows before they reach the

target plates, altering the overall pressure balance. In JET, when plasma detachment is achieved at the HFS divertor target, the parallel Mach number, $M_{\parallel}$ is increased close to the divertor plates in direction to the target plates ([20]). Although the overall electron temperature, T_e, is decreased during detachment (and therefore the ion sound speed velocity, c_s, according to Equ. (7)), the parallel pressure gradient and thus the SOL flow are measured to be enhanced (cf. [20], Fig. 9). Detachment is seen as a possible reason for the larger $M_{\parallel}$ in direction to the target plates.

Toroidal (core) plasma rotation is frequently observed in tokamaks, where it can be relatively easily initiated (in contrast to stellarators) by external sources (such as neutral beam injection). SOL flows might become affected due to viscosity by the core toroidal plasma rotation or vice versa. That SOL flows can have effects on the core plasma has been demonstrated in Alcator C-Mod, in experiments that only relied on ion cyclotron wave heating ([47]).

In view of the performed Doppler CIS impurity flow measurements, the influence of some secondary flow mechanisms on impurity flows in the divertor is deemed to be of lesser importance or just very local. Detachment or presheath acceleration happens directly in front of the divertor plates whereas the PS flows are more dominant at the midplane.

Parallel impurity flows in the SOL and divertor

There are several forces that are most influential for the measured Doppler CIS impurity flows in the divertor. Depending on the applied divertor regime and impurity parameters (distribution, sources ...), they can balance differently and also result in different impurity flow speeds and directions.
Impurity flows in the SOL are of particular interest, since they play a critical role in the migration of eroded materials from the main chamber and divertor surfaces to their final deposition locations [48] and for the core plasma purity. For a sufficiently small impurity concentration, three major competing processes govern the (parallel) impurity flow in the SOL ([28],(p.299)): the ion temperature gradient, ∇T_i, force (also referred to as 'thermal force'), the frictional force and the self-pressure. Simulations ([34]) indicate that these forces determine the flow direction and density of low charge-state carbon ions at i.e. the crown of the SOL in low-density L-mode plasmas.
The thermal ion force

$$\vec{F}_{\mathrm{iG}} = \beta_i \frac{d(k_B T_i)}{ds} \tag{12}$$

is dependent on the background plasma ion temperature gradient. s is the parallel-to-B distance measured from the target to the upstream direction. β_i is a coefficient of order Z^2. The ion temperature usually increases from the target plate to the stagnation point or upstream position at the midplane. Thus, the thermal force acts away from the target, to the SOL midplane, where cross-field transport might flush the impurities into the confined plasma region. According to

[28], the origin of the thermal force lies in a fundamental aspect of the Coulomb interaction that occurs between the charged particles: the cross-section for momentum transfer decreases strongly with the relative speed of the colliding particles. As a result, the (plasma ion)-(impurity ion) collision frequency has an inverse dependence on the ion temperature ([28],(p. 299)):

$$\nu_{iz}^{\text{mom}} \propto \frac{n_z Z^2}{m_i^{1/2} T_i^{3/2}}$$

The plasma ions striking impurity ions from the cold side transfer more momentum than plasma ions from the hotter side. Unfortunately, ion temperature measurements in the SOL are scarce and the effect of ∇T_i on impurity ion transport is usually investigated by numerical modeling [34].
The friction force

$$\vec{F}_{\text{F}} = m_Z \frac{v_i - v_Z}{\tau_s} \tag{13}$$

is dependent on the background (parallel) fluid plasma ion flow velocity, v_i, the impurity fluid velocity, v_z, and $\tau_s \propto T_i^{3/2}/Z^2$ being the stopping or slowing-down time. Equ. (13) is a rather heuristic approach to include the impurity entrainment or drag by the main plasma ion flow in the parallel direction. Since the parallel plasma ion flow is typically directed towards the target plates, the friction force pushes the impurities towards the divertor target plates, acting against the thermal ion force.

A third important force for impurity particles is resulting from the pressure gradient of the observed impurity species:

$$\vec{F}_{\text{PG}} = -\frac{1}{n_Z} \frac{\mathrm{d}p_Z}{\mathrm{d}s} \tag{14}$$

This force is pushing the impurity species away from the pressure maximum and may thus lead to flows either away or towards the divertor plates.
A more complete force balance equation for SOL impurity transport, with detailed descriptions of the mentioned and further terms can be found in e.g. ([28],(p. 298 ff.)).

2.5 Summary

SOL flows in diverted tokamak experiments are the result of an interplay of several flow drive mechanisms that yield different flow patterns (either towards or away from the divertor plates) for different impurity particle species. Generally, the main plasma ion flow is directed towards the target plates inside the divertor, which acts as a sink for the exhausted plasma. More plasma is radially transported out on the LFS of diverted tokamaks due to bad curvature. The pressure asymmetry, divertor sink and toroidal rotation exchange with the core plasma can further influence plasma ion flows in the SOL with an overall direction towards the divertor plates. (There are some conditions where flow reversal of the main plasma species might occur though

this was not the case for the AUG measurements presented in this work.)
Perpendicular flows are present in the SOL of tokamaks for both main plasma and impurity species due to classical drifts. However, perpendicular flows are usually smaller than parallel flows for impurities as well as plasma ions.
Although there are differences in first wall and divertor geometries among experimental devices, the measured parallel plasma flows at locations far away from material surfaces are reported to exhibit remarkably similar characteristics [13].

Although the flow of the main plasma species is usually directed towards the divertor plates, impurities can flow in the opposite direction. As ions, impurities can be transported from their point of ionization along the SOL magnetic field lines to the periphery of the confined plasma where, by cross-field transport, they may enter the confined plasma. There are several forces acting on impurities, some of them pushing the impurities away from the targets and some towards the targets. The forces scale with the charge state Z^2 and the species exist in different SOL regions (with different parameters), thus different flow patterns and sources might arise for ionization stages of the same element. Since SOL impurity flows are a complex balance of many processes, interpretation of flow measurements will be difficult. The complexity shows that such measurements are necessary to understanding SOL impurity transport.

3 Theory of Coherence Imaging Spectroscopy

The analysis procedures and theory of the Doppler CIS diagnostic and its essential components, the birefringent plates, are reviewed in this chapter. The Doppler CIS technique was proposed by John Howard at Australian National University ([49], [50]). This thesis focuses only on the spatial heterodyne principle for the Doppler CIS. There are various other principles that have been applied to the diagnostic in the past.
The Doppler CIS is a camera-based diagnostic that measures a plasma image modulated with an interference pattern. The interferometric signal encodes the spectral function of the observed plasma light and is generated with birefringent crystals in an optical set-up in front of the camera. Depending on the orientation of the incident light to the optical axis of the birefringent plates, each light wave is split into two phase-shifted, divergent rays. By the use of a polariser and imaging lens, the rays are then coherently interfered on the CCD chip. A spatially varying modulation pattern is generated over the CCD chip, since the phase shift of the rays do not only depend on the spectral wavelength, but also on the incidence angle of the light on the birefringent plates (that is different in each CCD pixel). The nature of birefringent light splitting will be looked into more detail in the first subsection of this chapter.
Since its invention, the Doppler CIS has undergone substantial development and improvement, that continue to this day. The goal of this work are reliable absolute flow calibrations from the Doppler CIS diagnostic in the high-temperature plasma experiment ASDEX Upgrade. There have been detailed reports on the coherence imaging technique in the PhD theses of S. Silburn ([51]) and C. Micheal ([52]). This chapter tries to give a comprehensive overview on the diagnostic with the spatial heterodyne technique, however, with emphasis on elements not discussed extensively before.

3.1 Birefringent plates

The term birefringence denotes the ability of an anisotropic optical material to refract an electromagnetic wave into two orthogonally polarised rays. Birefringence is dependent on the polarisation state and propagation direction of the initial wave. The optical phenomenon of double refraction, where a single ray of light is split into two rays taking slightly different paths, is a commonly known consequence of birefringence.
In this subsection, a short introduction on birefringent plates is provided. The presented properties in this and the next subsection are necessary for understanding the generation of the fringe pattern that is measured with the coherence imaging technique.

In a uniaxial birefringent material, there is a single direction governing the optical anisotropy. The direction of the optical anisotropy is denoted by the birefringent optical axis. All directions perpendicular to the optical axis are optically equivalent. Therefore, the velocity of a light wave travelling through a birefringent material differs for electric fields perpendicular and

parallel to the birefringent axis. In the case of only perpendicular polarisation orientation to the optical axis, the incident light is described by Snell's law and is denoted as ordinary. For parallel components to the optical axis, the refracted light is denoted as extraordinary and does not obey Snell's law[12].
There are also biaxial birefringent materials, that have two birefringent optical axes. However, they will not be discussed here.

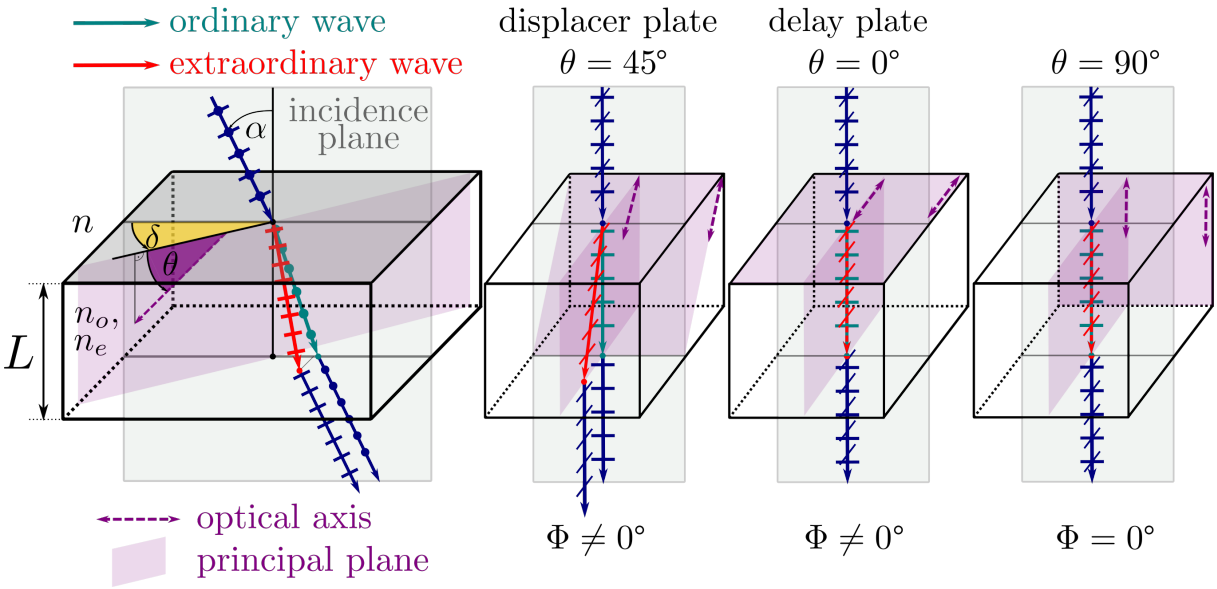

Figure 10 – Double refraction caused by a birefringent crystal. There are three principle cases of how the incident light can be influenced. θ is the angle between the optical axis and the incident surface. Φ is the phase shift between the ordinary and extraordinary ray. The left schematic was drawn after an illustration in [53].

The ordinary and extraordinary rays have different refractive indices, that depend on their velocity in relation to the optical axis, e.g. $n_o = \frac{c}{v_\perp}$. The velocity of the extraordinary ray is dependent on the angle between the electric field and the optical axis (in case of parallel alignment, $n_e = \frac{c}{v_\parallel}$). In Figure 10, there are different examples of the separation of light by a (uniaxial) birefringent material. They show two of the principal planes, which contain the optical axis and one of the polarisation directions. The electric field of the ordinary ray is always perpendicular to the optical axis. For the extraordinary ray, the electric field has some component parallel to the optical axis.
Depending on the propagation direction of the incident light and its electric field to the birefringent axis, the ordinary and extraordinary rays will diverge. Because they travel with different velocities and along different paths, there is also a phase shift Φ between the ordinary and extraordinary ray. If the propagation direction of the incident light is parallel to the

[12]In the case of normal incidence, the angle of refraction is zero, but the energy of the extraordinary ray may be propagated at an angle if the optical axis is not parallel to the ray propagation vector (cf. 2nd drawing in Figure 10). Snell's law is defined with respect to a material surface, not to any polarisation axis, which is why, regardless of the effective index of refraction, it cannot properly describe the extraordinary ray.

birefringent axis, the electric field $\vec{E}$ has only perpendicular components to it and both have $n = n_o$ (cf. right schematic in Figure 10).

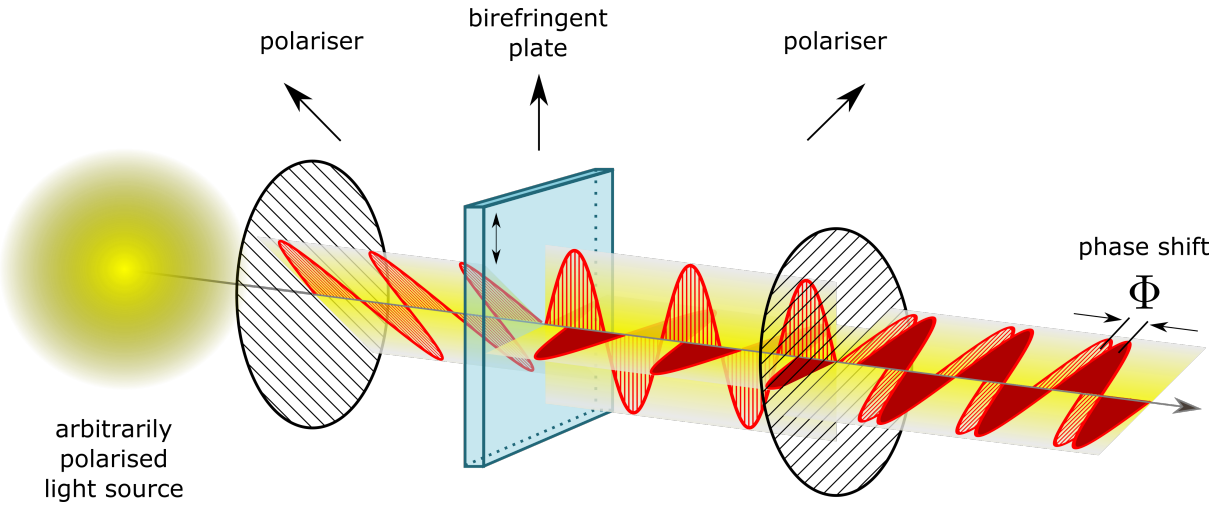

Figure 11 – Schematic of a birefringent plate between two crossed polarisers. The orientation of the plate optical axis is 45 ° to each of the polarisers. The electric field vectors of the ordinary and extraordinary ray are orthogonally polarised to each other before they pass the second polariser.

Due to the orthogonal polarisation and phase shift between the ordinary and extraordinary ray, a polarisation interferometer can be set up with birefringent crystals. This is shown in Figure 11. A uniaxial, plane-parallel birefringent plate is set-up between two crossed polarisers. This set-up is utilized in the Doppler coherence imaging diagnostic. At the first polariser, the electromagnetic waves of an arbitrarily polarised light source become linearly polarised. An ordinary and extraordinary ray are produced by the birefringent plate that have a relative phase shift Φ. Both rays are orthogonally polarised to each other, until they are aligned in the same direction by a second polariser.
From Maxwell's equations and consideration of the boundary conditions at the incident surface, the path of the extraordinary ray can be found and Φ calculated without approximation. For a uniaxial, plane-parallel plate [53]:

$$\begin{aligned}\Phi =& \frac{2\pi L}{\lambda_0}\left[\left(n_o^2 - n^2\sin^2\alpha\right)^{1/2} + \frac{n}{S}\left(n_o^2 - n_e^2\right)\sin\theta\cos\theta\cos\delta\sin\alpha\right.\\ &\left. -\frac{n_o}{S}\left(n_e^2 S - \left\{n_e^2 - \left(n_e^2 - n_o^2\right)\cos^2\theta\sin^2\delta\right\} n^2\sin^2\alpha\right)^{1/2}\right] \qquad (15)\\ S =& n_e^2\sin^2\theta + n_o^2\cos^2\theta\end{aligned}$$

A schematic overview of all the variables in Equation (15) is provided in Figure 10. α is the 'incidence angle' (between the direction of the incident electromagnetic wave and the plate surface normal). δ is the angle between the projections of the incident light and the optical axis on the plate surface. θ is the angle between the optical axis and the plate surface. n is the refractive index of air.
Thus, the phase Φ depends on the propagation direction of the incident light (in relation to

the optical axis), the wavelength λ as well as other plate parameters such as its thickness. For a single wavelength λ, there is constructive interference or destructive interference. In the case of a 45 ° angle between the polarisers and the birefringent plate axis, the amplitudes of the ordinary and extraordinary ray are equal. Only then, the rays completely cancel each other out in the case of $\Phi = 180\,°$.

There are three categoric constellations between the birefringent axis and the wave propagation direction. They are illustrated in the right three schematics of Figure 10. If the wave propagation in relation to the optical axis of the birefringent plate is...

1. ...neither parallel nor perpendicular: there is a displacement and a phase delay between the ordinary and extraordinary ray.
2. ...perpendicular: there is no displacement between the ordinary and extraordinary ray, however, there is phase shift Φ (cf. Figure 11 or 10).
3. ...parallel: there is no birefringent effect.

Corresponding to the second case, a birefringent plate with its optical axis parallel to the plate surface ($\theta = 0\,°$) is denoted as delay plate, since it contributes to the phase delay between the ordinary and extraordinary ray. In the first case of the birefringent axis neither parallel or perpendicular to the plate surface, the ordinary and extraordinary waves become displaced. This is why these plates are referred to as displacer plates (mostly $\theta = 45\,°$). Equ. (15) can be simplified for delay and displacer plates as follows:

$$\Phi(\theta = 0\,°) = \frac{2\pi L}{\lambda_0}\left[(n_o - n_e) - \frac{\sin^2\alpha}{2n_o}\left(1 + \frac{n_e}{n_o}\left[1 - \sin^2\delta\left(1 - \frac{n_o^2}{n_e^2}\right)\right]\right)\right] \tag{16}$$

$$\Phi(\theta = 45\,°) = \frac{2\pi L}{\lambda_0}\left[\frac{(n_o - n_e)}{2} + \frac{(n_o^2 - n_e^2)}{(n_o^2 + n_e^2)}\cos\delta\sin\alpha\right] \tag{17}$$

In comparison to delay plates, displacer plates generate about half the phase delay (for $\alpha = 0\,°$ in Equ. (16) and (17) for the same thickness L). However, only displacer plates show the effect of double refraction (for $\alpha = 0\,°$).

Different birefringent materials were investigated for the Doppler CIS diagnostic. The difference of the refractive indices

$$B = n_e - n_o \tag{18}$$

is used as a measure for the birefringence of a material. The higher the absolute birefringence index $|B|$, the larger the separation and phase delay Φ between the ordinary and extraordinary ray for a discrete wavelength λ[13]. The sign of B indicates the optical orientation of the (uniaxial)

[13]For perpendicular light ($\alpha = 0\,°$) on a delay plate ($\theta = 0\,°$), the phase shift between the ordinary and extraordinary ray corresponds to $\Phi = \frac{2\pi L}{\lambda}(n_o - n_e) = -\frac{2\pi L}{\lambda}B$.

crystal. E.g. in negative uniaxial crystals, the extraordinary ray moves faster than the ordinary ray and vice versa.
Generally, n_e and n_o vary non-linearly with wavelength for birefringent materials. In Figure 12, $|B|$ was determined for four different uniaxial materials in dependence of the wavelength λ. The investigated birefringent crystals are Lithium Niobate ($LiNbO_3$ or LN), α-Barium Borate (α-BaB_2O_4 or α-BBO), Yttrium Ortho-Vanadate (YVO_4) and Calcite ($CaCO_3$). These crystals can be purchased by optical component manufacturers. In the visible spectrum, the birefringence index is highest for YVO_4 and lowest for LN.

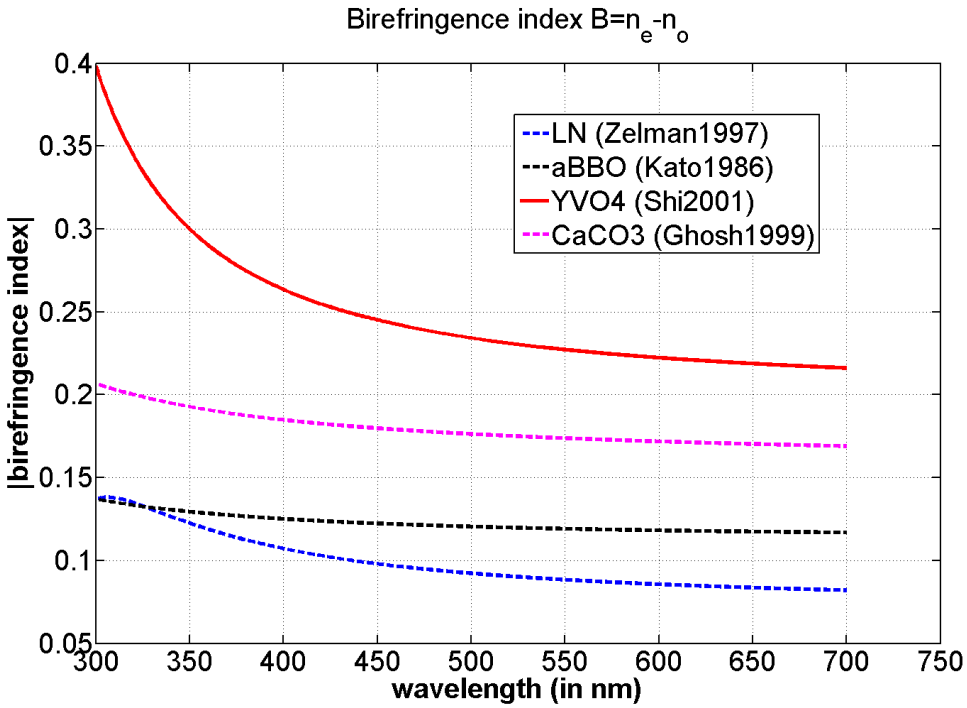

Figure 12 – Birefringent indices for four different uniaxial crystals over wavelength. The absolute birefringence value $|B| = |n_e - n_o|$ was displayed for better overview. The dashed lines indicate a negative birefringence sign, the continuous line a positive sign.

The birefringence B was calculated with the refractive indices n_o, n_e. For an arbitrary spectral wavelength λ, they can be approximated with either a simple form of the Sellmeier equation

$$n_{e,o}^2 = A_{e,o} + \frac{B_{e,o}}{\lambda^2 + C_{e,o}} + D_{e,o} \cdot \lambda^2 \tag{19}$$

or the three-oscillator Sellmeier equation:

$$n_{e,o}^2 - 1 = \frac{A_{e,o}\lambda^2}{\lambda^2 - B_{e,o}} + \frac{C_{e,o}\lambda^2}{\lambda^2 - D_{e,o}} + \frac{E_{e,o}\lambda^2}{\lambda^2 - F_{e,o}} \tag{20}$$

$A_{e,o}$, $B_{e,o}$, $C_{e,o}$, $D_{e,o}$, $E_{e,o}$ and $F_{e,o}$ are the so-called Sellmeier coefficients. They are fit values derived in various empirical studies. For each birefringent material, their values and

sources are listed in the Appendix (Tables 8 and 9). The Sellmeier equations are used in the analysis procedure of the Doppler CIS diagnostic, most notably for calculating the phase shift Φ.

For the Doppler CIS, not only the absolute value of the birefringence B is important, but also its dispersion $\mathrm{d}B/\mathrm{d}\lambda$. Since the diagnostic measures a wavelength change by the difference between two phase shifts (this will be explained in more detail in the next subsection), the parameter of interest for a delay plate is the change in phase shift $\Phi = -\frac{2\pi L}{\lambda} B$ over wavelength:

$$\frac{\mathbf{d}\Phi}{\mathbf{d}\lambda} = \frac{2\pi L}{\lambda} \cdot \left(\frac{B}{\lambda} - \frac{\mathbf{d}B(\lambda)}{\mathbf{d}\lambda} \right). \tag{21}$$

For a given plate thickness L, $\mathrm{d}\Phi/\mathrm{d}\lambda$ is a measure for the sensitivity of a birefringent material to a small wavelength change. $\mathrm{d}\Phi/\mathrm{d}\lambda$ was calculated for each of the four investigated birefringent materials over the range of the visible spectrum in Figure 13. In this work, the unit used to express the phase shift (and phase difference) is degrees, some other works prefer number of waves or radians. The highest effect of a Doppler shift can be measured with YVO_4 (for delay plates of the same thickness). Or, to get the same phase difference for a given Doppler wavelength shift, a YVO_4 delay plate would need to be less thick than a LN, α-BBO or $CaCO_3$ plate. During the course of this work, delay plates made of LN and α-BBO were used. ($CaCO_3$

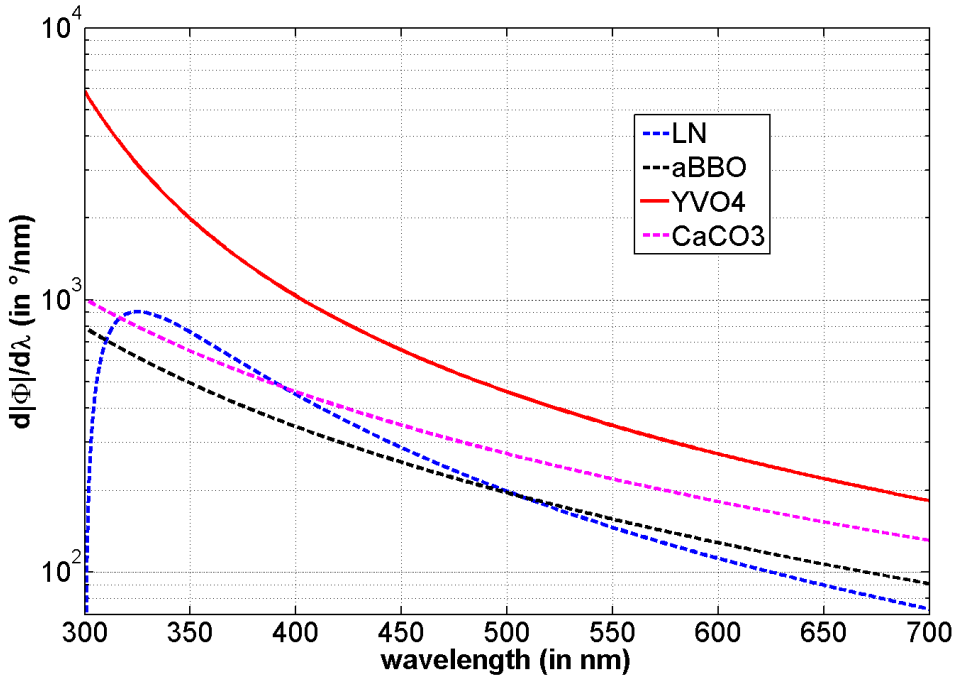

Figure 13 – The absolute sensitivity of four different birefringent materials to a wavelength change, expressed as $\mathrm{d}|\Phi|/\mathrm{d}\lambda$. For each plate a thickness of $L = 1\,\mathrm{mm}$ and $\theta = 0\,^\circ$ (delay plate), $\alpha = 0\,^\circ$ was assumed. The dashed lines indicate a negative sign, the continuous line a positive sign.

and YVO_4 were not offered in the required sizes by the manufacturers.) Generally, LN is more effective in the blue part and less effective in the red parts of the visible spectrum than α-BBO.

n_o and n_e are dependent on temperature, thus Φ is dependent on the ambient temperatures as well. This is an important implication for the Doppler CIS, since changes in Φ need to be considered for the analysis. There are measures to omit phase changes with ambient temperatures, e.g. by temperature control units to contain the birefringent plates and keep them on a constant temperature. Or by 'passive temperature control', where plate materials with negative and positive temperature coefficients are combined to balance each other's temperature-dependent changes. A measurement example of the change of Φ with ambient temperature T has been carried out by ([21]).
There are different dependences of $n_o(T)$ and $n_e(T)$ for different birefringent materials. The LN plates are more sensitive to ambient plate temperatures than e.g. α-BBO, however both materials were used in this work.

3.2 Coherence Imaging Spectroscopy

The properties of birefringent crystals enable them for use in a Fourier transform spectrometer. Fourier transform spectroscopy is an experimental technique whereby spectral information is collected based on measurements of the coherence or autocorrelation of a radiative source. There are several applications as diagnostics, e.g. the Michelson interferometer can be used as one. Either time-domain or space-domain measurements of the radiation are performed in a Fourier transform spectrometer. The radiation spectrum can then be obtained by a Fourier transform.
The main idea of coherence imaging spectroscopy is the measurement of an interferogram produced by a set of birefringent plates from a narrowband source such as a plasma emission line. This subsection will deal with the interferogram properties of that technique. Since the spectral function of an atomic emission line determines its coherence, spectral properties can be derived from the interference pattern generated by the birefringent crystals.
From the interferogram of a coherence imaging spectrometer, basic spectral properties such as e.g. the central position of a (Doppler-shifted) plasma emission wavelength are determined. In a plasma, where atomic emission lines are emitted by the atomic shells of moving ions, the central position of the emission line can be used to determine the averaged speed of the ions along the line-of-sight.

The following mathematic derivation of the interferogram signal S is based on derivations presented in [52] and [51]. The use of birefringent crystals in a Fourier transform spectrometer for plasma spectroscopy has been proposed by John Howard ([54]). By the birefringent separation of light into ordinary and extraordinary rays, a 2-beam source of coherent light is provided. Generally, in 2-beam interferometers, the path difference or phase shift between the two rays can be expressed by a time delay, $\tau = \frac{\Phi}{\nu}$ ($\nu = c/\lambda$). For a polychromatic light source

with complex electric field amplitude $E(t)$, the amplitude at the interferometer output will be

$$u(t) = \frac{1}{2}\left(E(t) + E(t+\tau)\right).$$

The corresponding detected signal S at output is

$$\begin{aligned} S(\tau) &= \langle u(t)u^*(t)\rangle \\ &= \frac{1}{4}\left\langle E(t)E^*(t) + E(t+\tau)E^*(t+\tau) + E(t)E^*(t+\tau) + E(t+\tau)E^*(t)\right\rangle \\ &= \frac{1}{2}\left[I_0 + \Re(\Gamma(\tau))\right] \end{aligned} \tag{22}$$

with the first two terms equaling the (real) intensity I_0. $\Gamma(\tau) = \langle A^*(t)A(t+\tau)\rangle$ is the time-averaged autocorrelation of the electric field for time lag τ. This is complex and known as the self-coherence of the light. The coherence Γ is related to the normalised light source spectral shape $g(\nu)$ though

$$\Gamma(\tau) = I_0 \int g(\nu)\exp\left[2\pi i\nu\tau(\nu)\right]\mathrm{d}\nu = I_0\gamma. \tag{23}$$

$\gamma = \Gamma/I_0$ is referred to as degree of coherence:

$$\gamma(\tau) = \int g(\nu)\exp\left(2\pi i\nu\tau\right)\mathrm{d}\nu. \tag{24}$$

This shows that with a Fourier Transform, information about the spectral shape $g(\nu)$ can be derived from the measurements of $S(\tau)$ over a range of τ. The time delay τ (related to Φ) is provided by the displacer plate (Equ. (17)) and the required variation by the varying incidence angle (α) to the plate over the CCD image.

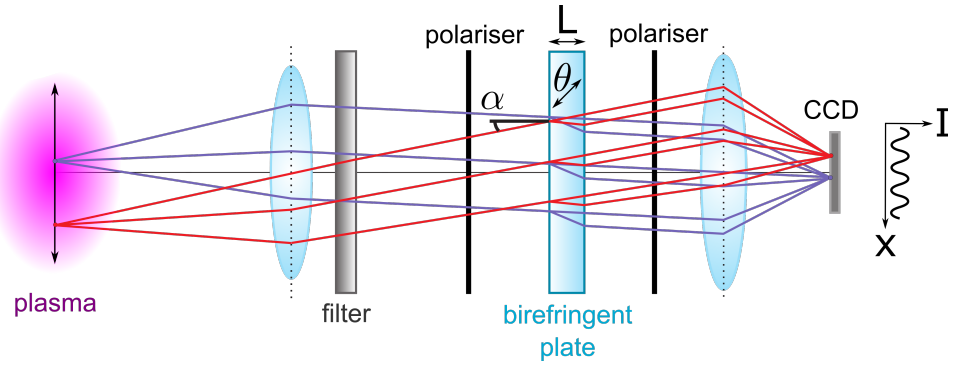

Figure 14 – Schematic of a spatial heterodyne Doppler coherence imaging spectrometer.

Figure 14 shows a schematic of this principle. The wavelengths emitted by a light source (e.g. a plasma) are imaged onto a CCD camera chip with optical lenses. Since the ordinary and extraordinary rays leave the birefringent plate with the same incidence angle α as they entered it, the imaging lens is used to interfere and focus them at a location depending on α.

Each pixel-sightline of the camera collects light that is passing the birefringent plate with the same propagation direction. Thus, birefringent crystals in combination with optical lenses and a camera enable a two-dimensional coherence measurement of a light-emitting substance. This is referred to as *coherence imaging*.

The coherence imaging system is a passive optical diagnostic. Φ varies over the CCD chip mainly in dependence of the birefringent plate parameters. The relation of the angles α and δ to the CCD chip position (x,y) for Φ simulation can be found in the Appendix A.4. $\Phi(x, y)$ is the property of interest, since it is also the measured quantity obtained with the Doppler CIS. A typical interference pattern can be seen in Figure 15, the fringe structure of which is largely due to the variation of the incidence angle α and the projection angle δ, that differ for each CCD pixel-sightline. This is why even if the wavelength is the same for each camera sightline (as e.g. during a calibration with a spectral lamp), a fringe pattern is still recorded over the CCD chip. A Doppler CIS set-up that analyses the coherence by the spatial variation of the fringe pattern is referred to as spatial heterodyne design. A spatial design has the advantage of requiring only one image per measurement, thus being able to measure plasma phenomena of shorter timescales. It is also possible to use Doppler CIS set-ups that contain the coherence data in the time domain[14].

To analyse a spatial heterodyne coherence imaging design, a fringe phase Φ varying over the CCD chip dimensions in one direction (such as in Figure 15) is required for reasons explained in the next subsection. One-directional varying fringes are either produced by a displacer plate or a Savart plate[15]. Displacer with $\theta = 45\,^\circ$ produce a linearly depending phase on the incident angle α (for $\alpha < 5\,^\circ$ and thus $\sin(\alpha) \approx \alpha$). They have been applied in more recent Doppler CIS applications in TEXTOR [25] and MAST [24]. Birefringent delay plates produce a hyperbolic fringe pattern.

A coherence imaging system requires a narrow-bandpass filter in order to separate out a single atomic emission line from the plasma. In general, it is not possible to measure the interferogram of several (non-multiplet) atomic emission lines with a coherence imaging system at the same time. Since each wavelength produces its own interference pattern, the patterns of a continuous spectrum or too many different emission lines would cancel each other out. Furthermore, the measured emission line must not be too broad for the same reason. Line broadening mechanisms in plasma experiments with strong magnetic fields are e.g. Doppler

[14]Temporal multiplexing designs have been used e.g. for the Doppler CIS on WEGA [22] or the MOSS camera on the H1-Heliac [23]. In these systems, birefringent delay plates were used in combination with a linear electro-optic (Pockels) cell. The birefringence of the cell could be altered over time by applying different electric fields. This is why at least three interference patterns had to be recorded at different Pockels cell electric fields.

[15]A Savart plate is put together by two crossed displacer plates. They produce an effective displacement of the ordinary and extraordinary ray, but a netto zero phase delay.

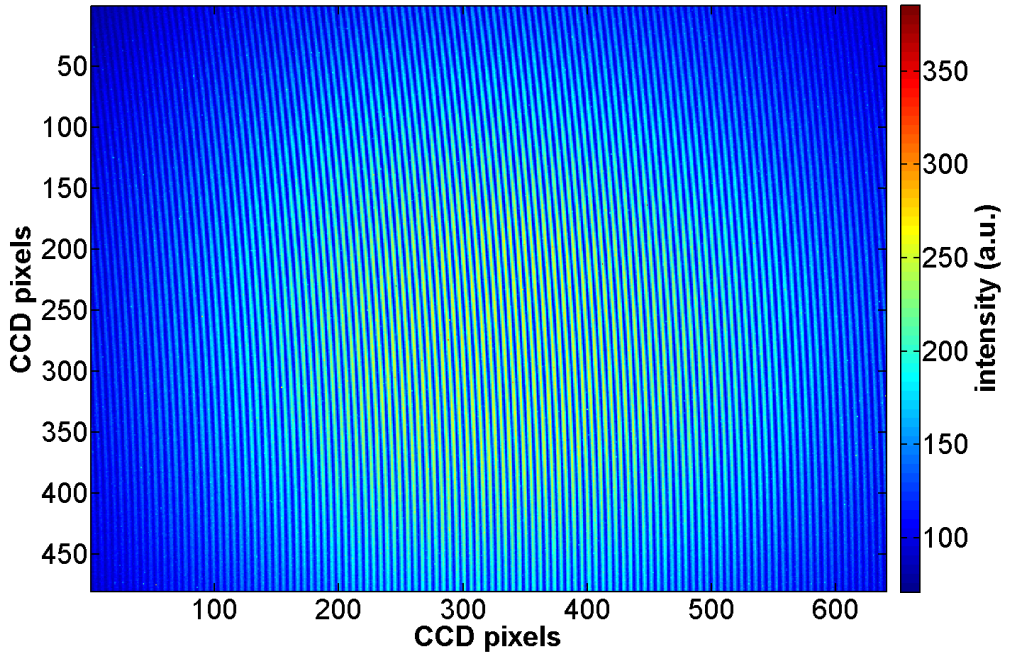

Figure 15 – Measured image from a single atomic emission wavelength with the Doppler CIS system. The fringe structure is dependent on the type of birefringent plate in use. The source is a Zn spectral calibration lamp at 468.014 nm in an Ulbricht calibration sphere.

broadening (connected to plasma temperature), Zeeman splitting (connected to the magnetic field of the plasma experiment) or the Stark effect (due to electric fields in the plasma). A detailed description of these can be found in e.g. [55].

Since its invention and first tests reported in the late 90s ([54]), coherence imaging has been constantly developed and evolved. Until today, two coherence imaging techniques with promising results have been applied and tested in different plasma experiments: the Doppler coherence imaging spectroscopy (Doppler CIS) and the Imaging Motional Stark Effect (IMSE) diagnostic. They are used to measure different physical quantities in laboratory plasmas. The Doppler CIS enables the measurement of the line emission, the central position of a (Doppler-shifted) emission wavelength as well as the broadening of that wavelength (along each line-of-sight of the camera). Thus, in a plasma, where atomic emission lines are emitted by the atomic shells of moving ions, these three quantities could be used to derive the line density, averaged speed of the ions (both along the line-of-sight) as well as the ion temperature (from Doppler broadening). The basic set-up of a Doppler CIS can be seen in Figure 14.
In contrast to the Doppler CIS, the IMSE measures an interference pattern dependent on the wave polarisation as well as the wavelength. This is achieved by removing the first polariser in Figure 14. Due to the polarisation dependence, the magnetic pitch angle of the plasma (in a magnetic confinement experiment) can be determined via the motional Stark effect ([56]).
In the following, the Doppler CIS will be explained and discussed in more detail.

A single emission line from a (low-temperature) plasma is regarded as a quasi-monochromatic spectrum with $\Delta\nu/\nu_0 \ll 1$. The spectral shape $g(\nu)$ of the emission line can be expressed in a reference frame with its centre-of-mass frequency $\nu_0 = \int \nu g(\nu)\mathrm{d}\nu / \int g(\nu)\mathrm{d}\nu$ such that $g(\nu) = g(\nu' + \nu_0)$. Substituted into Equ. (24), the degree of coherence becomes

$$\gamma(\tau) = \exp\left(2\pi i \nu_0 \tau\right) \gamma' \tag{25}$$

where $\gamma'(\tau) = \int g'(\nu) \exp\left(2\pi i \nu \tau\right) \mathrm{d}\nu$ represents the slowly varying envelope of the coherence and $\nu_0\tau$ the phase of the fast varying 'carrier'. It is assumed that $g'(\nu)$ is an even function ($g(\nu_0 + \nu') = g(\nu_0 - \nu')$), thus, $\gamma'(\tau)$ is real. Inserting this into Equ. (22), the interferometer signal S becomes

$$\begin{aligned} S(\tau) &= \frac{1}{2}\left[I_0 + \Re(\gamma(\tau) \cdot I_0)\right] \\ &= \frac{I_0}{2}\left[1 + \Re(\exp(2\pi i \nu_0 \tau)\gamma'(\tau))\right] \\ &= \frac{I_0}{2}\left[1 + |\gamma'(\tau)| \cos(2\pi\nu_0\tau)\right] = \frac{I_0}{2}\left(1 + \zeta \cos\Phi\right) \end{aligned} \tag{26}$$

The interferometer signal S is a set of sinusoidal interference fringes in x-direction (since $x \propto 1/\tau$), as shown in Figure 15. The contrast or visibility of the fringes, $\zeta = (S_{\mathtt{max}} - S_{\mathtt{min}})/(S_{\mathtt{max}} + S_{\mathtt{min}})$, is equal to the degree of coherence $\zeta = |\gamma'|$. Thus, ζ is a measure of the spectral line shape $g'(\nu)$. The carrier phase $\Phi = 2\pi\nu_0\tau$, equal to the phase shift between the ordinary and extraordinary rays at $\nu = \nu_0$ for a given pixel x, is only affected by changes in the centre wavelength $\nu_0 = c/\lambda_0$.

3.2.1 Demodulation

This subsection will explain the extraction of the fringe brightness, contrast and phase shift Φ with the Fourier Transform.
A Fourier Transform is used to mathematically decompose the Doppler CIS interferogram S into three major components in frequency space. From Equ. (26):

$$S(\Phi) = \underbrace{\frac{I_0}{2}}_{I(0)} + \underbrace{\frac{I_0}{2}\zeta\frac{1}{2}\exp^{i\Phi}}_{I(+)} + \underbrace{\frac{I_0}{2}\zeta\frac{1}{2}\exp^{-i\Phi}}_{I(-)} \tag{27}$$

The 2-dimensional, absolute FT of the interferogram of Figure 15 can be seen in Figure 16. Since the fringes in Figure 15 vary in x-direction, the peaks in the Fourier image align in x-direction. There are three major components in the Fourier image, corresponding to Equ. (27). The first one, $I_0/2$, is independent of the radiation wavelength, the peaks to the left and right represent the negative frequency peak $I(-)$ and the positive peak $I(+)$ of the observed atomic

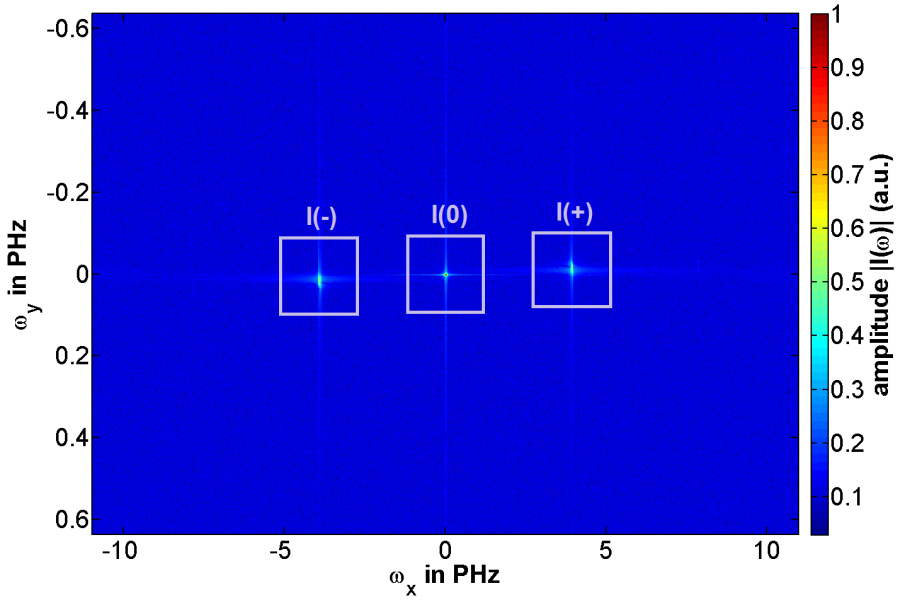

Figure 16 – Absolute of the 2-dimensional Fourier transform of the interference pattern in Figure 15. There are three major peaks for one (narrow) calibration wavelength at 468.014 nm.

emission line. By isolating $I(0)$, $I(+)$ and $I(-)$ in frequency space and taking the inverse 2-dimensional FT of each component separately, ζ, Φ and the spectral emission brightness I_0 can be determined as follows:

$$I_0 = 2 \cdot |I(0)| \tag{28}$$

$$\zeta = 2 \cdot \frac{|I(\pm)|}{|I(0)|} \tag{29}$$

$$\Phi = \tan^{-1}\left(\frac{\Im(I(\pm))}{\Re(I(\pm))}\right) \tag{30}$$

It is equivalent whether $I(-)$ or $I(+)$ are chosen to determine ζ and Φ. To determine these values with inverse Fourier Transform, an area of the Fourier space has to be cut from it. The larger the area, the higher the spatial resolution of the contrast, brightness or phase images will be. Perpendicular to the fringes, the available FT of each peak is limited by the two other peaks that must not contaminate the chosen area, respectively. Therefore, the possible spatial resolution of the Doppler CIS is higher parallel to the fringes (in the example of Figures 15 and 16 in the y-direction). It is therefore desirable to orient the fringes parallel to the steepest gradients expected for the measured plasma properties.

The frequency resolution or Nyquist frequency $\omega_{\mathrm{Nyq}} = 2\pi\nu_{\mathrm{Nyq}} = 2\pi c/\lambda_{\mathrm{Nyq}}$ of the Doppler CIS is determined by the number of pixels a fringe occupies on the CCD chip. The fringe size is determined by the thickness of the birefringent displacer plate and the camera pixel size. The lower the fringe size (either by choosing a thicker displacer plate or using a camera with smaller pixel size), the higher ω_{Nyq} will be and the shorter wavelengths can be resolved. However,

there is an optimal frequency resolution for each camera, since the fringe size should still cover a few pixels to be resolvable (usually at least four or more pixels). The maximum achievable spatial resolution for I_0, ζ and Φ would be gained if the $I(\pm)$ peaks would be positioned at $\omega = 2/3 \cdot \omega N_{\mathrm{Nyq}}/2$ (by choosing the camera pixel size and displacer plate thickness accordingly), placing the components generated of a observed emission line at 2/3 of the distance between the centre and edge of the FT space. This allows the largest selection area for the inverse FT and demonstrates how the spatial resolution of I_0, ζ and Φ is related to the spectral resolution of the Doppler CIS.

Next to the birefringence fringes, fine structures in the background of the image such as tiles of the plasma wall or the grid-like structure of the image fibre bundle pixels (cf. Figure 66, Appendix A.3) can cause high frequency signals that will appear in Fourier space. These additional Fourier elements can mix with the $I(0)$ or $I(\pm)$ components generated by the Doppler CIS fringes, corrupting the values of I_0, ζ and Φ. The objective lens can be defocused slightly to "blur" the image structures out and avoid their elements in Fourier space.
Other corrupting signals in Fourier space can, of course, be generated by additional emission lines that enter through the spectral filter of the Doppler CIS system. It is very important to check whether adjacent emission lines exist close to the observed plasma line and may enter through the selected narrow bandpass filter as well, since two plasma emission lines only a few nanometres distant from each other will appear as one $I(\pm)$ peak in Fourier space and distort each others values for $I(0)$, ζ and Φ.
A third possible mechanism to generate additional elements in Fourier space is related to the image edge. The Fourier peaks in Figure 16 appear crossed by horizontal and vertical lines (or streaks). They are the result of fringes abruptly ending at the measured Doppler CIS image edges (cf. Figure 15). The higher the fringe intensity at the image edges, the stronger these lines will appear in the Fourier image. By this, the inverse FT of each $I(0)$ or $I(\pm)$ component may contain elements of these lines and I_0, ζ and Φ become corrupted. To prevent the existence of such lines in Fourier space, vignetting (that smoothly reduces the entire image intensity near the borders of a measured Doppler CIS image) is favourable in this instance, since then the lines in Fourier space are also diminished.

Figures 18 to 20 show examples of I_0, ζ and Φ determined according to Equ. (28)-(30) from the measured Doppler CIS image in Figure 17. The image was taken in the lower divertor of the plasma experiment ASDEX Upgrade. The experiment, the observed line radiation as well as the view of the Doppler CIS into ASDEX Upgrade will be described in more detail in chapter 7. Figures 17 and 18 reveal the areas of highest radiation (the plasma). There is not only plasma radiation but also light reflection from the plasma vessel walls. In the contrast image (Figure 19), the area of highest fringe visibility is close to the area of highest intensity. A disturbance can be seen in the contrast as well as in the phase image (Figure 20) at the left edge. It arises

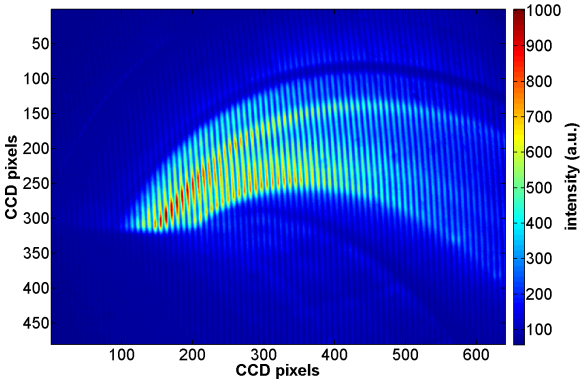

Figure 17 – Measured Doppler CIS image of a plasma emission line at 656.1 nm in the ASDEX Upgrade divertor.

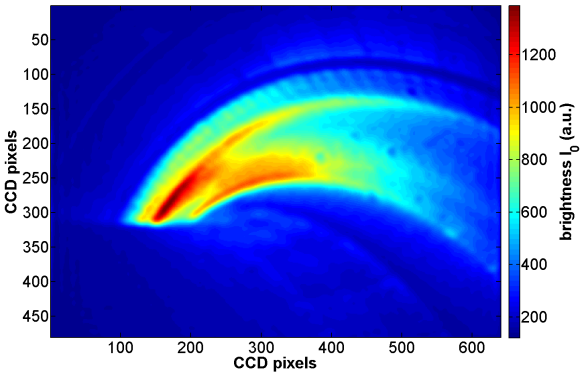

Figure 18 – Emission brightness I_0 recovered with a FT from the measured Doppler CIS image in Figure 17.

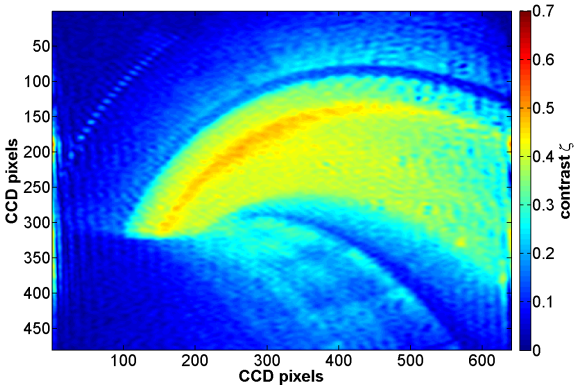

Figure 19 – Fringe contrast ζ recovered from the measured Doppler CIS image in Figure 17.

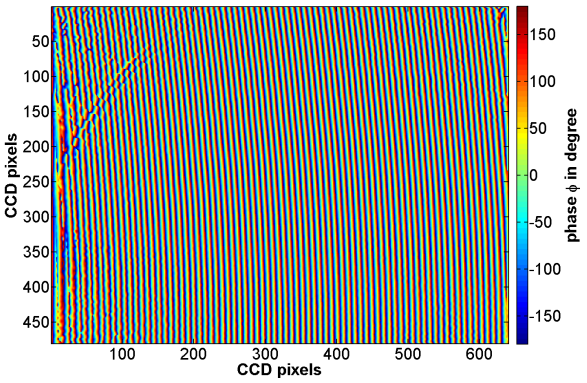

Figure 20 – Fringe phase Φ recovered from the measured Doppler CIS image in Figure 17.

from fine structures in the background image that dominate over the weak fringe signal at that position.

The interferometer signal S is the integral of the different line shapes $g(\nu)$ at all positions along each line-of-sight. However, I_0, ζ and Φ are derived from S with a FT where it is assumed that they are equivalent to the line-averaged I_0 values and intensity weighted line average of ζ and Φ. The assumption may not be true for e.g. lines with distinct areas of very different particle velocities for ζ and Φ, where the equivalent Φs differ on the order of half or an entire wave (this could happen if e.g. the spectral resolution is not large enough for the observed Doppler shifts of the investigated emission line).
In the following, the further analysis of only Φ is discussed, from which the integrated line-of-sight velocity of the light-emitting particles, v, is derived. From ζ, the emitting species temperature T can be determined, however the ζ analysis of the temperature was not covered in this study (and is therefore not commented here). To measure T effectively, the Doppler CIS delay needs to be adjusted to be very sensitive to temperature changes. A rough outline of how T may be derived from the fringe contrast ζ can be found in e.g. ([51]).

3.2.2 Calibration of the central measured emission line wavelength

The fringe phase Φ_D is measured by the Doppler CIS for an observed emission line of the plasma. With Φ_D, the velocity of the moving particles that emit the detected light can be derived, since Φ_D is dependent on the centre-of-mass wavelength of the (Doppler-shifted) plasma emission line λ_D, according to Equ. (26). With λ_D and the centre-of-mass wavelength of the un-shifted emission line, λ_0, the velocity of the plasma particles emitting the observed emission line, v_D, can be derived according to Doppler's law:

$$v_D = c \cdot \frac{\lambda_0 - \lambda_D}{\lambda_0}. \tag{31}$$

It is clear from Equ. (15) that the measured fringe phase from the plasma, $\Phi_D(\lambda_D)$ is dependent on several quantities such as plate parameters, light incidence and the plasma wavelength:

$$\Phi_D = \frac{1}{\lambda_D} \cdot \mathbf{f}\left(L, n_o, n_e, \alpha, \delta, \theta\right) \tag{32}$$

$\mathbf{f}\left(L, n_o, n_e, \alpha, \delta, \theta\right)$ denotes the formula of Equ. (15) without the factor $\frac{1}{\lambda}$. It is not possible to simply calculate Φ_D or to extract λ_D from the measured Φ_D, since the Doppler shift of the emission wavelength, λ_D, is unknown. Additionally, there are many uncertainties concerning the plate parameters, such as the location of the CCD pixel were $\alpha = 0\,^\circ$ (cf. Appendix A.4), the exact thickness L of the displacer and delay plates (possibly varying over their surface) or the effective focal length f of the imaging lens for the observed wavelength[16]. To determine λ_D, it is necessary to calibrate the Doppler CIS set-up with a nearly monochromatic light source at a known wavelength, $\lambda_{\mathtt{cali}}$. In the simple case of $\lambda_{\mathtt{cali}} = \lambda_0$, the calibration phase is then:

$$\Phi_0 = \frac{1}{\lambda_0} \cdot \mathbf{f}\left(L, n_o, n_e, \alpha, \delta, \theta\right). \tag{33}$$

With the measured calibration phase Φ_0 at a known wavelength λ_0, a subtraction of the two phase images is performed:

$$\Delta\Phi_{\mathrm{D}} = \Phi_D - \Phi_0 = \mathbf{f}\left(L, n_o, n_e, \alpha, \delta, \theta\right) \cdot \left(\frac{1}{\lambda_{\mathrm{D}}} - \frac{1}{\lambda_0}\right) \tag{34}$$

The phase subtraction is essential relate an unknown wavelength λ_D to a known one. However, Equ. (34) is valid only if:

1. All physical quantities on which $\mathbf{f}$ depends remain unchanged between the calibration and the plasma measurement.

2. $\lambda_{\mathtt{cali}}$ is close to the measured, Doppler-shifted wavelength, λ_{D}.

[16] The focal length determines the range of the incidence angle α over the CCD chip (cf. Appendix A.4)

The first condition implies that the hardware and illumination of the diagnostic remain unchanged between the calibration and the plasma measurement. The second condition arises due to the fact that n_e and n_0 are in reality also dependent on λ. Small changes in λ cause changes in n_e and n_0 and thus Φ. Only for negligible changes in n_e and n_0 between the plasma measurement and calibration, $\mathbf{f}_D \approx \mathbf{f}_{\texttt{cali}}$. By defining $\lambda_D = \lambda_0 + \Delta\lambda_D$ relative to the stationary plasma wavelength λ_0, and considering the following approximation

$$\frac{1}{\lambda} = \frac{1}{\lambda_0 + \Delta\lambda} = \frac{1}{\lambda_0} \cdot \frac{1}{1 + \frac{\Delta\lambda}{\lambda_0}} \approx \frac{1}{\lambda_0}\left(1 - \frac{\Delta\lambda}{\lambda_0}\right), \tag{35}$$

Equ. (34) results in

$$\Delta\Phi_{\mathrm{D}} = \mathbf{f}\left(L, n_o, n_e, \alpha, \delta, \theta\right) \cdot \frac{\lambda_0 - \lambda_D}{\lambda_0^2} \tag{36}$$

Then, the measured $\Delta\Phi_D$ is directly linked to the Doppler shift λ_D. A simulated wavelength scan is necessary to determine the slope $\Delta\Phi/\Delta\lambda$ for the $\Delta\Phi_{\mathrm{D}} \rightarrow \Delta\lambda_D$-relation in Equ. (36). For this, the Doppler CIS plate parameters $L, n_o, n_e, \alpha, \delta, \theta$ need to be known. But neither Φ_D nor Φ_0 have to be calculated directly for Equ.(36), only the slope $\Delta\Phi/\Delta\lambda$. This is critical since uncertainties in the plate parameters cannot be avoided and even small errors (e.g. $\delta L \approx 0.1\,\mathrm{mm}$, $\delta f \approx 2\,\mathrm{mm}$ or $\delta\alpha \approx 1\,^\circ$) can lead to very different phases $\Phi(\lambda, L, f, \alpha, ...) \neq \Phi(\lambda, L + \delta L, f + \delta f, \alpha + \delta\alpha, ...)$. However, for the slope $\Delta\Phi/\Delta\lambda$, the nominal plate parameters with small deviations from the real values are sufficient, since the offsets between $\Phi_D(\lambda_D, L + \delta L, \alpha + \delta\alpha, ...) - \Phi_D(\lambda_D, L, \alpha, ...) = \delta\Phi_D$ and $\Phi_0(\lambda_0, L + \delta L, \alpha + \delta\alpha, ...) - \Phi_0(\lambda_0, L, \alpha, ...) = \delta\Phi_0$ are almost the same for the measured wavelength shifts on the order of picometres (as in VINETA.II and AUG). The small, systematic error for $\Delta\Phi/\Delta\lambda$ arising due to the plate uncertainties is determined by calculating $\delta\Phi_D$ and $\delta\Phi_0$ directly according to Equ. (15).

Figure 21 shows four different examples of the $\Delta\Phi \rightarrow \Delta\lambda$-relation. The sign of the relation is dependent on the direction of the birefringent axis of the displacer plate (angle θ). It will change if e.g. $\theta = 45\,^\circ$ or $\theta = -45\,^\circ$. It is therefore important to pay attention to the orientation of the displacer plate when it is inserted into the diagnostic plate set-up. Otherwise, without a measured $\Delta\Phi \rightarrow \Delta\lambda$-relation (e.g. by a wavelength scan with a tunable laser), it is difficult to reconstruct the sign of the relation and thus the direction of the flows (either towards or away from the observer). For the Ar II emission line, which was measured in VINETA.II, many thick delay plates were inserted. This was done to achieve a strong dependence of $\Delta\Phi$ on $\Delta\lambda$ in order to resolve relatively small Doppler shifts in the range of a few picometer.
$\frac{\Delta\Phi}{\Delta\lambda}$ defines the wavelength resolution of the Doppler CIS diagnostic. Its unit is usually denoted in °/pm. Important parameters that determine the wavelength are the birefringent plate material and the thickness L of the used (delay) plates. In theory, by increasing the number of delay plates, the wavelength resolution can be increased as much as desired. However, with

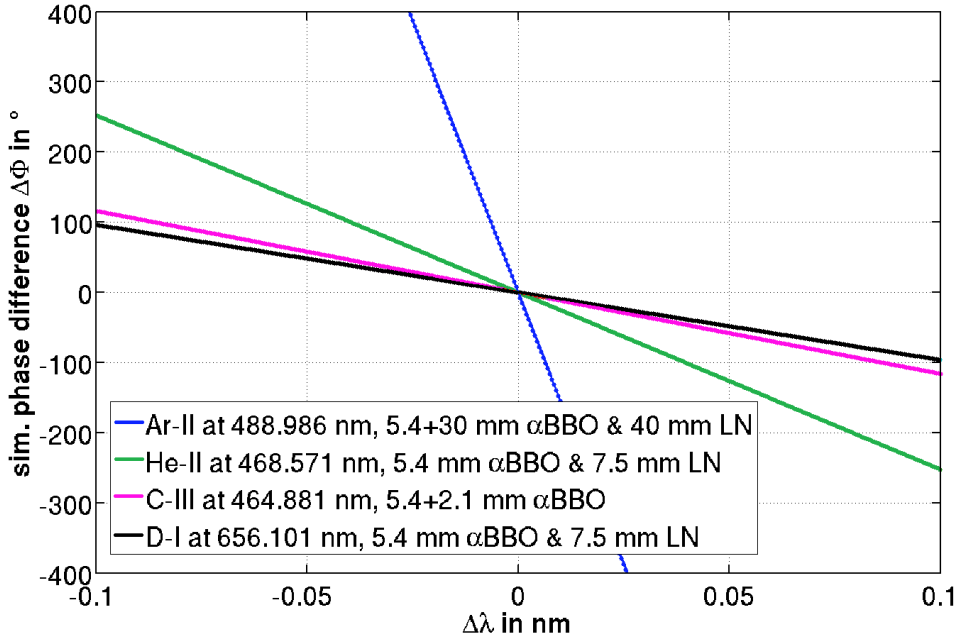

Figure 21 – Simulated phase difference $\Delta\Phi$ over wavelength shift $\Delta\lambda$ at incidence angle $\alpha = 0\,^\circ$ for four different plate configurations used in VINETA.II and ASDEX Upgrade measurements. For each configuration, a 5.4 mm α-BBO displacer plate was considered.

increasing number of plates, the contrast decreases, as will be explained in more detail in the next chapter. Illumination or vignetting effects and the ambient plate temperature dependence increase, too. By the use of Yttrium Vanadate (YVO_4), which has the largest sensitivity to wavelength changes (cf. Figure 13), the potential wavelength resolution could be increased substantially. However, for the flows measured during this work, α-BBO and LN were sufficient.

The desired Doppler shift $\Delta\lambda$ can be derived from the measured phase shift $\Delta\Phi_\mathrm{D}$ according to Equ. (36). However, Equ. (36) is only valid if the plasma emission line has a symmetric spectral shape around its centre-of-mass, λ_0. Most of the intense emission lines in the plasma SOL of a high-temperature plasma experiments are asymmetrical multiplets. They consist of multiple closely spaced line components due to fine structure or Zeeman splitting. An additional phase is generated by each of the lines the multiplet consists of, weighted with the line emissivity. This was first reported in ([51]). The more asymmetric the spectral shape, the larger the multiplet phase difference offset $\Delta\Phi_M$. It can be determined according to:

$$\Delta\Phi_M = \underbrace{\tan^{-1}\left(\frac{\Im(I_{S_M}(\pm))}{\Re(I_{S_M}(0))}\right)}_{\Phi_M} - \Phi(\lambda_0) \tag{37}$$

The interferometer signal S is calculated according to Equ. (26) for each corresponding line wavelength, λ_i, weighted with the relative intensity of the individual multiplet lines, I_i, and added together: $S_M = \sum_{i=1}^{n} I_i \cdot S(\lambda_i)$. With the S_M peaks in Fourier space, $I_{S_M}(\pm)$ and $I_{S_M}(0)$,

the multiplet phase Φ_M can be determined according to Equ. (30). λ_0 is the centre-of-mass of the (un-shifted) multiplet. A table containing all the relevant multiplet line data can be found in Appendix A.2. Equ. (37) was evolved in the frame of this work to estimate the multiplet phase difference offset and originates from the ansatz reported in ([51],(p.30)). Although Equ. (37) is more time-consuming to calculate, it considers effects from the displacer plate (not applied in ([51]) and incidence-angle (α) dependent phase delays.

As an example, $\Delta\Phi_M$ was calculated for the C III multiplet in Figure 22. From all plasma emission lines measured with the Doppler CIS during this work, the C III multiplet had the most asymmetric spectral function. For an α-BBO displacer plate of 5.4 mm and a delay plate of 2.1 mm thickness, $\Delta\Phi_M$ varies between -5 and -20 ° over the camera chip of the Doppler CIS. For the pixel where $\alpha = 0\,°$, the calculated $\Delta\Phi_M$ is in good agreement with the ansatz reported in ([51]).

The relative intensities I_i and wavelengths positions λ_i need to be known accurately to estimate $\Delta\Phi_M$ (and the centre-of-mass of a multiplet) correctly. These parameters are well known theoretically for the investigated multiplets (cf. Appendix A.2). In AUG, the shape of the investigated multiplet lines in AUG agreed well with the theoretical values. A detailed investigation was carried out in MAST ([51]), where the line data was also confirmed. For the Doppler CIS measurements of an ion velocity, an asymmetric modification of the spectral line shape would be critical. Variations of a spectral emission line could be expected in the presence of e.g. strong electric fields, which can lead to asymmetrical Zeeman splitting.

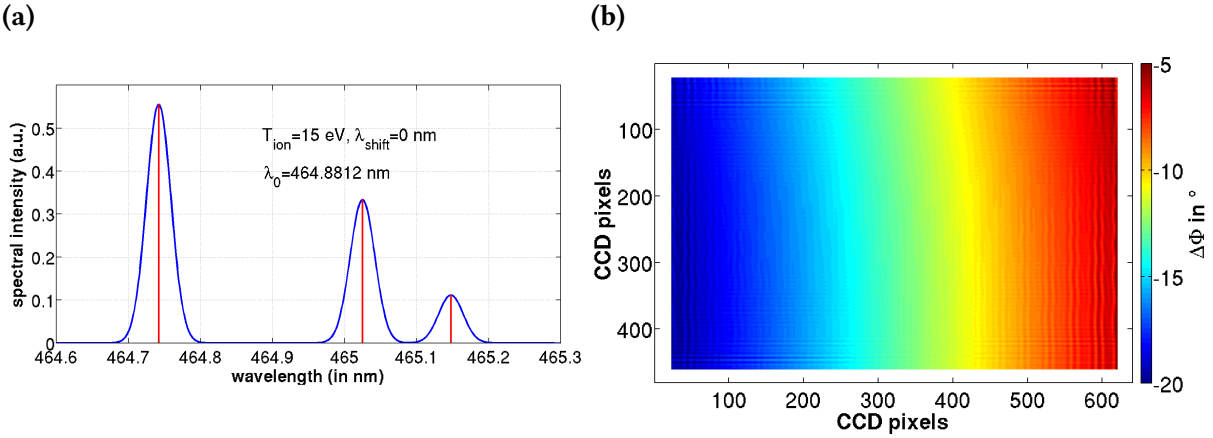

Figure 22 – (a) Simulated spectrum of the asymmetric C-III multiplet at 464.881 nm. (b) Calculated phase difference $\Delta\Phi_M$ for the C-III multiplet.

If $\lambda_{\mathtt{cali}} \neq \lambda_0$, another phase difference is produced that has to be considered in the Doppler CIS analysis. Large wavelength differences (on the order of 0.1 nm meters or more) between $\lambda_{\mathtt{cali}}$ and the un-shifted centre-of-mass of the observed plasma wavelength give rise to a significant phase variation over the CCD camera chip. Figure 23 shows an example of a phase variation generated between the centre-of-mass of the C III multiplet and a calibration line that is about 3 nm separated from it (typical available calibration source). The corresponding fringe measurement image of the calibration is shown in Figure 15. The variation is dominated by

the orientation of the fringe pattern, that is produced by the displacer plate. This phase variation $\Delta\Phi_V = \Phi(\lambda_0) - \Phi(\lambda_{\mathtt{cali}})$ needs to be accounted for, which is why it needs to be calculated.

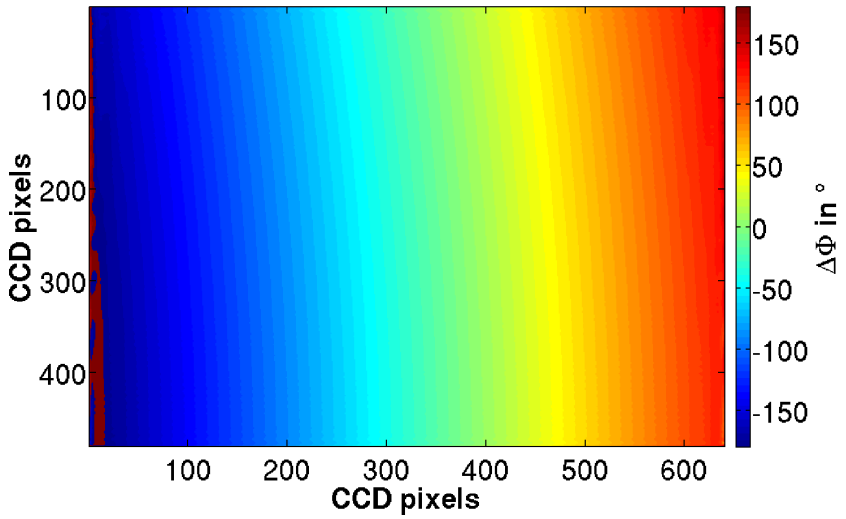

Figure 23 – Calculated correction phase difference $\Delta\Phi_V = \Phi(\lambda_0) - \Phi(\lambda_{\mathtt{cali}})$ image for $\lambda_{\mathtt{cali}} = 468.014\,\mathrm{nm}$ and $\lambda_0 = 464.881\,\mathrm{nm}$.

Considering $\Delta\Phi_M$ and $\Delta\Phi_V$, Equ. (36) needs to be adjusted as follows:

$$\begin{aligned}
\Delta\Phi_D &= \mathbf{f}\,(L, n_o, n_e, \alpha, \delta, \theta) \cdot \frac{\lambda_{\mathtt{cali}} - \lambda_0 + \lambda_0 - \lambda_D}{\lambda_0^2} - \Delta\Phi_M \\
&= \mathbf{f}\,(L, n_o, n_e, \alpha, \delta, \theta) \cdot \left(\frac{\lambda_0 - \lambda_D}{\lambda_0^2} + \frac{\lambda_{\mathtt{cali}} - \lambda_0}{\lambda_0^2} \right) - \Delta\Phi_M \\
&= \mathbf{f}\,(L, n_o, n_e, \alpha, \delta, \theta) \cdot \left(\frac{\lambda_0 - \lambda_D}{\lambda_0^2} \right) + (\Phi(\lambda_0) - \Phi(\lambda_{\mathtt{cali}})) - \Delta\Phi_M \qquad (38) \\
&= \mathbf{f}\,(L, n_o, n_e, \alpha, \delta, \theta) \cdot \left(\frac{\lambda_0 - \lambda_D}{\lambda_0^2} \right) + \Delta\Phi_V - \Delta\Phi_M \qquad (39)
\end{aligned}$$

Thus, the Doppler shift is determined as

$$\Delta\lambda = \frac{\Delta\Phi_D - \Delta\Phi_V + \Delta\Phi_M}{\mathbf{f}\,(L, n_o, n_e, \alpha, \delta, \theta)} \cdot \lambda_0^2 \qquad (40)$$

Since $\Delta\Phi_V = \Phi(\lambda_0) - \Phi(\lambda_{\mathtt{cali}})$ needs to be calculated, Equations (39) and (40) are prone to errors arising from uncertainties of the plate parameters. For the entire analysis procedure, the plate set-up used for measurements needs to be documented carefully. However, it is not easy to measure e.g. for which camera pixel $\alpha = 0\,^\circ$, or the effective thickness L of the used displacer and delay plates in a set-up. The focal length of the CCD lens may vary with observed wavelength and may deviate a millimetre from to the nominal value of the lens. With each change to the hardware of the diagnostic (interference filters, plates or adjustment of the image bundle) some of these parameters might change as well. During the ASDEX Upgrade

measurements, it has been observed that by using the nominal values for the plates (e.g. $\alpha = 0\,^\circ$ at the centre CCD pixel, L as documented by the plate manufacturer etc.), a phase offset $\Delta\Phi_e$ is present in the analysed measurements with the procedure of Equ. (40). Since this offset was not noticed during the measurements, uncertainties in the plate parameters were not measured accordingly.
Interestingly, by comparing a measured calibration image phase, $\Phi_{\mathtt{meas}}(\lambda_{\mathtt{cali}}, L{+}\delta L, f{+}\delta f, ...)$ with simulated calibration phase, $\Phi_{\mathtt{sim}}(\lambda_{\mathtt{cali}}, L, f, ...)$, the effective focal length of the lens in front of the CCD can be fitted accordingly for the measurements. f is fitted to minimize $\delta\Delta\Phi/\delta x$ and $\delta\Delta\Phi/\delta y$. This resulted in a nearly linear phase difference error $\Delta\Phi_e \approx 50\,^\circ$ that remained relatively constant throughout several measurement days. It was different for He II and D-α measurements.
$\Delta\Phi_e$=$\Phi_{\mathtt{sim}}(\lambda_{\mathtt{cali}}, L, f, ...)$-$\Phi_{\mathtt{meas}}(\lambda_{\mathtt{cali}}, L + \delta L, f + \delta f, ...)$ was eliminated by subtracting it from the measured plasma phase $\Delta\Phi_{\mathrm{D}}$:

$$\Delta\lambda = \frac{\Delta\Phi_{\mathrm{D}} - \Delta\Phi_V + \Delta\Phi_M - \Delta\Phi_e}{\mathbf{f}\,(L, n_o, n_e, \alpha, \delta, \theta)} \cdot \lambda_0^2 \tag{41}$$

$$\Delta\Phi_{\mathrm{D}} = \mathbf{f}\,(L, n_o, n_e, \alpha, \delta, \theta) \cdot \left(\frac{\lambda_0 - \lambda_D}{\lambda_0^2}\right) + \Delta\Phi_V - \Delta\Phi_M + \Delta\Phi_e \tag{42}$$

This is the procedure used for the ASDEX Upgrade measurements, where the observed plasma emission lines were multiplets and no calibration source was available at $\lambda_{\mathtt{cali}} = \lambda_0$. With the determination of $\Delta\Phi_e$, absolute calibration of the AUG measurements was possible. Since $\Delta\Phi_e$ is determined by the difference of the simulated and measured calibration images, it does not rely on the measurement itself, only on the calibration.

3.3 Summary

The Doppler CIS measures the plasma image of a (filtered) plasma emission line, that is modulated with an interference pattern. The interference signal is produced by birefringent plates and is dependent on the plate parameters and the spectral function of the observed line. Through Equations (15), (31), (32) and (41), an image of the line-averaged flow velocity, v_D, can be determined from the measured interference image and corresponding calibration image. For the analysis Equation (41), additional terms arise if the observed emission line is not a multiplet or if the calibration line is not equal to the centre-of-mass of the un-shifted emission line wavelength. To correctly calculate these additional terms, highly accurate knowledge of the plate parameters is necessary. If only nominal values of the plate parameters (such as e.g. the manufacturers values of the plate thickness L) are known, a phase offset will arise due to the plate uncertainties. The phase offset was omitted by the subtraction of a simulated calibration image with a measured one.
Absolute flow measurements have also been investigated concurrently and independently by

another group working with the Doppler CIS on the DIII-D tokamak experiment ([57]). They suggest to use a tunable wavelength scan to fit the plate parameters for each plate configuration. This would allow to use calibration lines $\lambda_{\mathtt{cali}} \neq \lambda_0$ and determine $\Delta\Phi_D$ without phase offsets due to simulation errors.

4 Doppler coherence imaging diagnostic

During the course of this work, the diagnostic set-up has been varied and improved several times, first to meet the requirements to measure on VINETA.I and VINETA.II, then on ASDEX Upgrade. In this chapter, the set-up, measurement and calibration procedure that was ultimately used during the later measurements at ASDEX Upgrade will be described.
In ASDEX Upgrade, an image fibre bundle had to be used to guide light from the torus. Since no active or passive plate temperature control was used, a diagnostic set-up was desired that would enable direct calibration before and after each Doppler CIS flow measurement. To meet this requirement, a steerable mirror was included in the set-up of the diagnostic. The main results of this work were obtained with this set-up.

4.1 Set-up

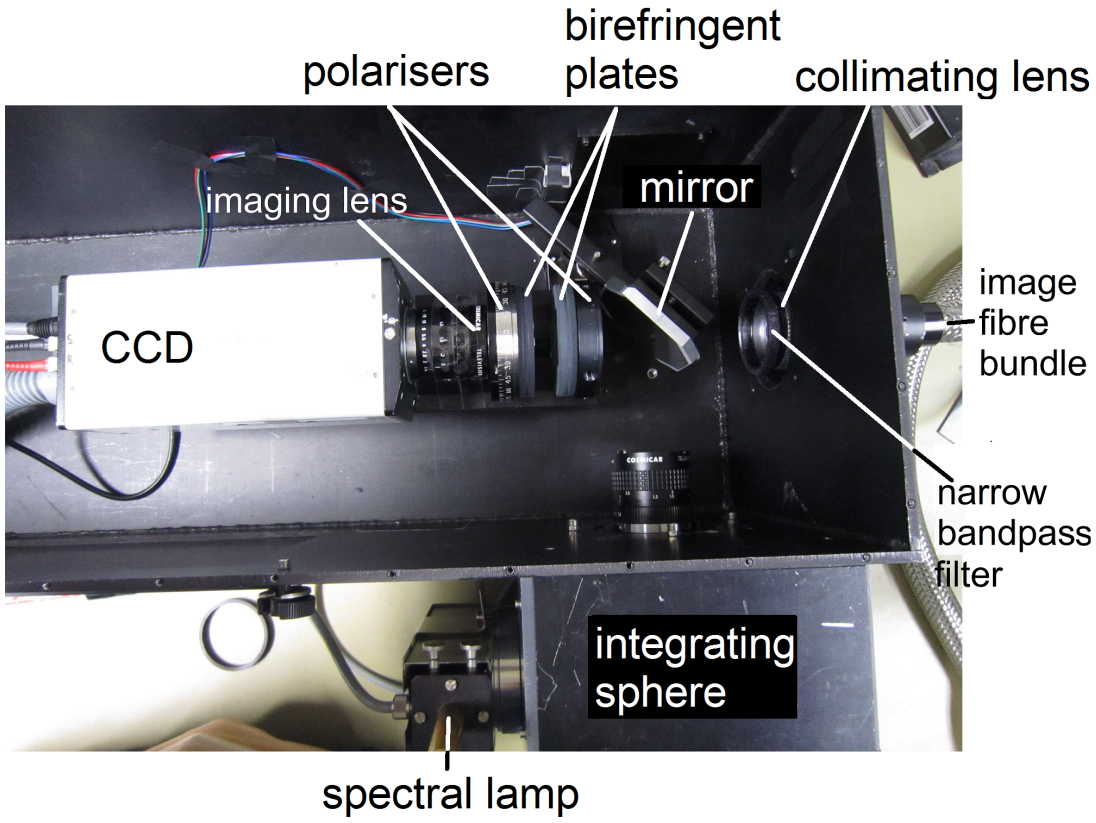

Figure 24 – Overview of the Doppler coherence imaging set-up.

Figure 24 shows an overhead view of the optical components of the Doppler CIS diagnostic for the VINETA.II and AUG Doppler measurements. A 45° displacer plate is used with a combination of varying delay plates, depending on the observed plasma line and desired velocity resolution. They are placed inside a black box in order to avoid stray radiation. The CCD camera, birefringent plates and polarisers are mounted onto a fixed rail inside the box. A mirror is fixed onto a mounting that allows precise alignment and connected to a stepper

motor through an arm. The motor is firmly attached to the box. The movable mirror set-up is preferred to a (fixed) half-reflective mirror in order to maximise the light throughput during plasma measurements.
In the lower part of Figure 24, there is smaller black box containing an Ulbricht sphere for calibration. The sphere is used to homogeneously illuminate the CCD camera chip. Depending on the needed calibration source, either a laser (diode) or a spectral lamp is used as calibration source. In the case of a lamp, it was directly attached to the Ulbricht sphere (as in Figure 24). For lasers, an optic fibre is used to transmit the laser light into the sphere.

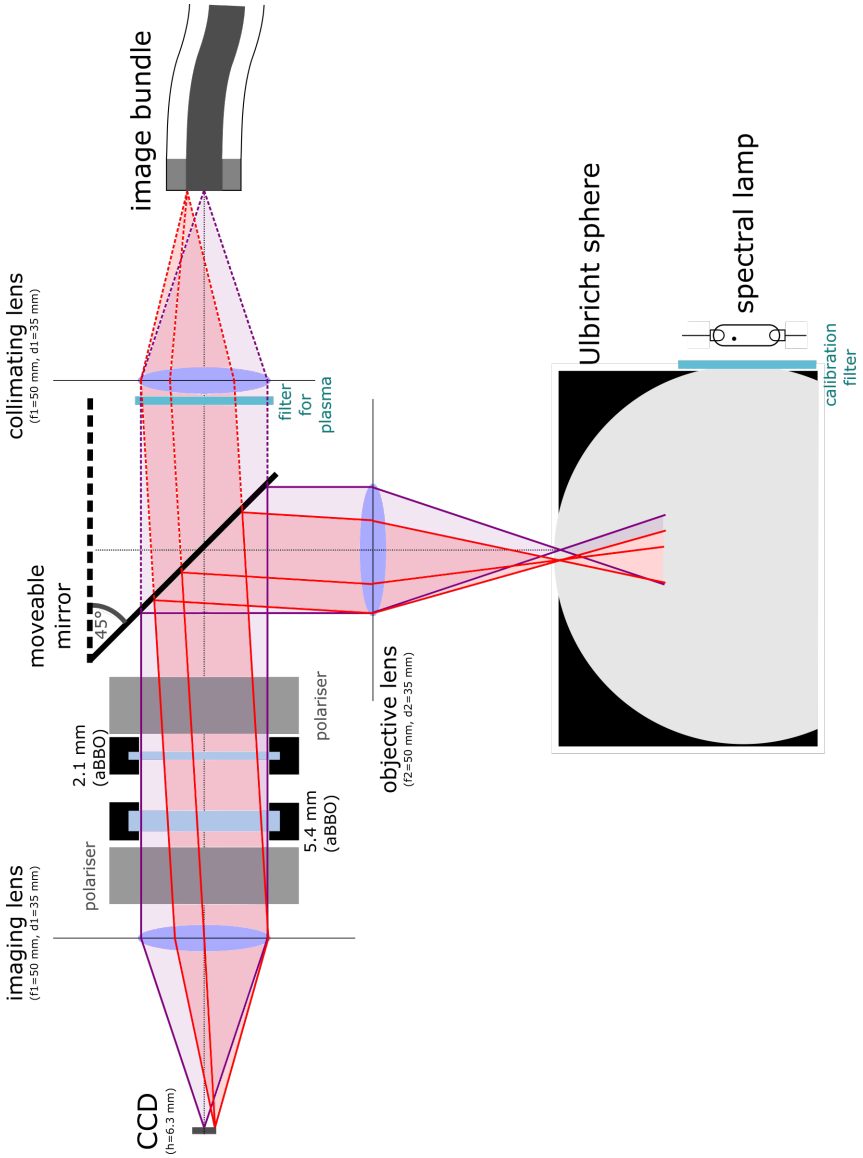

Figure 25 – Schematic of the light paths in the Doppler coherence imaging diagnostic with a moveable mirror.

For the AUG measurements, an image fibre bundle is necessary to transmit light from the plasma volume to the diagnostic. A diagnostic set-up directly in front of a vacuum window (like for the Doppler CIS diagnostics in e.g. MAST [24] or WEGA [22]) was not possible. Using an image fibre bundle is advantageous for the diagnostic set-up, since it reduces problems arising

from vignetting. As is shown in Appendix A.3, the transmitted light through the image fibre bundle leaves each bundle pixel with its original angle of incidence but spreads azimuthally into a cone. Thus, the plates become illuminated more homogeneously in the case of vignetting objects near the plasma than without a bundle. Therefore, the light cone of a bundle is more similar to the calibration path, where the Ulbricht sphere produces a very homogeneous light cone through the birefringent plates.
For the preferred view into VINETA.II, the use of an image fibre bundle eases access to the diagnostic considerably. In Figure 24, one end of the image fibre bundle can be seen in the right part of the image. It transmits the light directly into the CCD camera, for which the mirror is removed out of the path. The use of an image fibre bundle leads to significantly lower transmission, in particular when neutrons degrade the fibres. But an image bundle has the advantage that the diagnostic is further away from the strong magnetic field of AUG. A more detailed report of the used image fibre bundles, their advantages and disadvantages and their neutron degradation is provided in Appendix A.3.

As in the system set-up in Figure 14, a $f = 50\,\text{mm}$ collimating lens is mounted on the end of the image fibre bundle to focus the light transmitted by the image fibre bundle at infinity. The lens is mainly covered in Figure 24 by the mounting that fixes it to the black box. The same lens is also mounted in front of the Ulbricht sphere, in the same distance to the mirror as the lens on the image fibre bundle, to imitate the path of the plasma light with the calibration light as accurately as possible. It is important for the calibration and plasma light to have the same distribution of paths through the birefringent plates for each camera sightline. This is due to the inhomogeneity of the birefringent plates and e.g. having a varying thickness over their surface ([51],[58]). If the light does not travel through the same plate area, a phase offset between the calibration and measurement might arise. For even relatively small differences in the illumination of the plate area very large phase differences can be observed, which lead to unacceptable errors in the calibration. Therefore, the focus and the aperture settings of both lenses need to be the same.
The first lens in front of the CCD camera is necessary to focus the fringes generated by the birefringent crystals. The focus needs to be set very carefully to obtain optimal fringe contrast. There is an optimal focus setting for the fringes, related to the incidence angle of the light through the birefringent plate. Fringe contrast becomes optimal if all light collected in a CCD pixel has passed the birefringent plates under the same incidence angle. For reasons not yet fully understood, the point of optimal focus varies for different plate configurations.
The focal length of the imaging lens determines the fringe size in camera pixel units. One fringe should cover several pixels to be resolvable. For the Doppler CIS measurements presented in this work, this was achieved with a lens of $f = 50\,\text{mm}$[17]. The theoretical optimal fringe resolution for maximal spatial Doppler CIS signal is half of the Nyquist frequency as discussed in chapter 3.

[17]The camera had 480×640 pixels with a size of 9.9 μm.

The narrow-bandpass interference filter to select a single emission line from the plasma is attached directly to the collimating lens at the end of the image fibre bundle. A narrow-bandpass filter between the sphere and the lamp assures that only the intended Zn calibration line is transmitted into the sphere. This arrangement with two filters is necessary to calibrate both plasma emission lines investigated in the blue part of the AUG spectrum with the same calibration source. For the C III line, the Zn I calibration line is not in the range of the C III narrow-bandpass filter.
To avoid Newton interference rings on the analysed Doppler CIS phase images, the interference coating of the spectral filters needs to be applied on one side of the filter surface only. Some filter companies can apply all coatings (there is a narrow-bandpass as well as a broad range coating reaching into the IR) just on one side of the filter. Furthermore, the filters should be very narrow (FWHM $\approx 1 - 2\,\mathrm{nm}$) and have a flat top to avoid a corruption of the spectral intensity function of the observed plasma line. If e.g. a filter with a Gaussian transmission curve is applied, the spectral emission line shape could be altered and the centre-of-mass of the emission line would be shifted and wrongly interpreted as a Doppler shift.

In Figure 25, the path of the light from the plasma (through the image fibre bundle) and the calibration sphere are compared. If the paths do not match, a phase offset would be introduced since the plate is not homogeneous and ideal. Therefore, the mirror needs to be positioned in a 45° position to the path of the plasma light. The mirror and the stepper motor were set-up and aligned in the laboratory before the Doppler CIS was moved into the AUG torus hall. A 532 nm laser source was used to compare the phase difference $\Delta\Phi$ between the plasma light path (through the image bundle) and the calibration path. The precise alignment of the mirror on the stepper motor can be found by minimizing $\Delta\Phi$.
If the optical CIS set-up is altered, the entire functionality of the diagnostic needs to be checked. E.g. if the birefringent plates are exchanged, the fringe contrast can be decreased. Then the focus of the first lens needs to be readjusted. Another example is the exchange of the narrow-bandpass filters. Next to the birefringent plates, that need to be optimised for each observed emission line (explained in more detail in the next subsections), the focus of the objective lenses may also differ in case of large wavelength changes. The focus of the collimating lens on the end of the image fibre bundle was different for plasma emission lines in the blue part of the spectrum (between 460 and 470 nm) and the red part of the spectrum (around 650 nm).

In the next subsections, the pre-measurement preparations, measurement procedure and analysis for the Doppler CIS are presented in detail. Overall, in particular for the Doppler CIS measurements in AUG, this work greatly profited from the experiences reported in the PhD thesis of S. Silburn ([51]).

4.2 Pre-measurement investigations

When choosing a plasma emission line for Doppler CIS measurements, the spectral properties of the line need to be investigated beforehand. The line intensity in the plasma experiment will determine the exposure time of the Doppler CIS camera and thus the temporal resolution of the observed physical flow phenomena. In case of multiplets, the line ratios are necessary parameters for the CIS analysis procedure. An overview of these parameters for the measured multiplets in ASDEX Upgrade can be found in Appendix A.2. It is important to apply the correct intensity ratio of between these lines in Equation (37), otherwise the centre-of-mass of the spectral emission line is reproduced falsely, which would be interpreted as an additional Doppler shift. The observed emission lines in VINETA.II and ASDEX Upgrade are presented in chapters 6 and 7.
A calibration wavelength source in close proximity to the plasma line has to be provided as well. The further separated the calibration and emission line wavelengths are, the more sensitive the analysis becomes to plate parameter uncertainties (see chapter 3.2.2). A calibration source equal to the un-shifted emission line is optimal for analysis. An overview of conventional calibration lamp sources is given in subsection 4.2.1 of this chapter. A lack of suitable calibration sources has limited the investigated ion species for Doppler CIS flow measurements in all existing set-ups so far ([51],[57]).
Furthermore, basic plasma parameters such as the electron temperature or the strength of the magnetic field need to be approximately known in order to estimate line broadening effects such as Zeeman splitting or Doppler broadening. Spectral line broadening will determine the fringe contrast produced with the birefringent plates in the Doppler CIS set-up. The broader the line, the less the fringe contrast and hence the lower the signal-to-noise of the measured flow velocity. In the case of multiplets, the contrast of the observed emission line becomes more complicated. As demonstrated in Equ. (29), the fringe contrast is also determined by the time delay between the ordinary and extraordinary ray. The time delay is dependent on the wavelength and the plate thickness, amongst other plate parameters. Each multiplet line produces its own interference pattern, that overlay with the patterns of the other lines. Depending on the multiplet structure, local minima and maxima of the fringe contrast exist as a function of the plate thickness L[18]. In Figure 26, the simulated spectral multiplets and their corresponding fringe contrast ζ is plotted over the delay and displacer plate thickness for the He II, C III and the D-α lines measured in AUG.

The contrast ζ is determined by simulating a comprehensive Doppler CIS interference pattern with Equ. (26) for the multiplet. For each line, a species temperature of $T_i = 15\,\mathrm{eV}$ is assumed for Doppler broadening[19]. The interference patterns of each multiplet line are summed

[18] These minima and maxima are also dependent on other plate parameters, however L is the parameter most easily varied by adding more plates. This is why only the dependence on L is discussed here.

[19] The contrast is also varying with the particle species temperature, generally being decreased for increasing

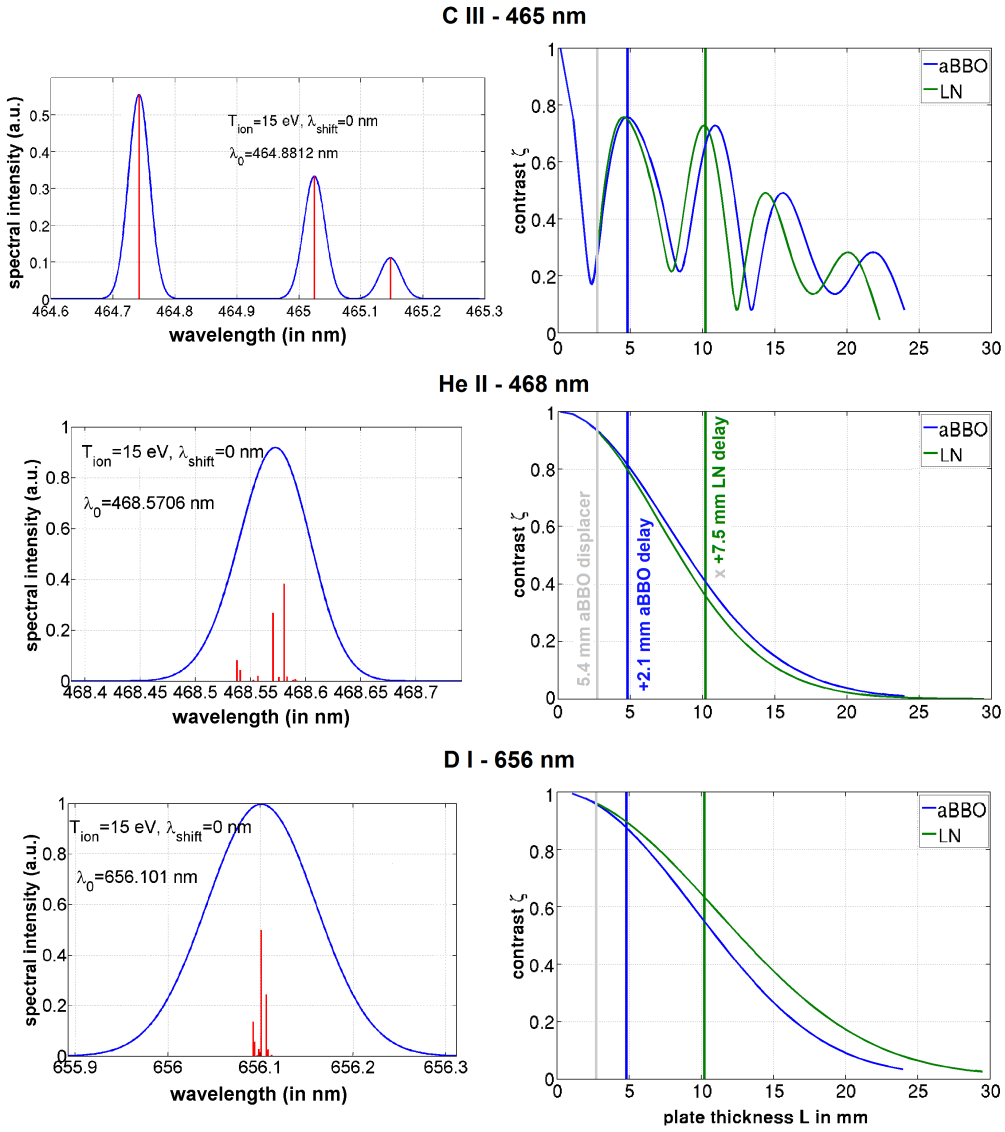

Figure 26 – Comprehensive (blue) and single (red) multiplet line intensity over wavelength (left) and contrast ζ over effective delay plate thickness L for three different emission lines measured with the Doppler CIS in AUG. The delay plates were both added to the 5.4 mm displacer plate, that acts as a 2.6 mm delay plate.

up and weighted with their relative intensity. This ansatz shows very good agreement for the He II and C III contrast behaviour over L with the results obtained in ([51]) (D-α was not simulated by ([51])). An overview schematic of the spectral functions can be found in Figure 22a and the Appendix A.2.

To achieve good fringe contrast for the Doppler CIS measurements, the delay plate thickness is selected close to a global or local ζ maximum (cf. Figure 26). However, the number and thickness of the plates also needs to be optimised for the wavelength sensitivity (or flow resolution). Table 1 presents an overview of the achieved flow velocity and wavelength sensitivity

temperature. An example of the contrast variation with temperature can be found in ([51],p.63)

for different birefringent plate combinations. A phase difference of $\Delta\Phi = 10\,^\circ$ is chosen as a reference for the wavelength sensitivity, since it is typically reasonably above noise levels of the diagnostic signal.

displacer	**delay**	$\Delta\lambda/\Delta\Phi = 10\,^\circ$	$v_{\mathtt{ion}}/\Delta\Phi = 10\,^\circ$	ζ (for He II)
5.4 mm α-BBO		14.9 pm	9.63 km/s	93%
5.4 mm α-BBO	2.1 mm α-BBO	8.6 pm	5.56 km/s	82%
5.4 mm α-BBO	7.5 mm LN	3.9 pm	2.49 km/s	37%
5.4 mm α-BBO	10 mm α-BBO	3.3 pm	2.14 km/s	22%

Table 1 – Multiplet flow and corresponding wavelength sensitivity for $\Delta\Phi = 10\,^\circ$ for the C III multiplet at 465 nm for different plate configurations.

Generally, more birefringent plates result in higher flow resolution, but lower fringe contrast. For e.g. the C III mutliplet in AUG, a $L = 2.1$ mm delay plate was included in the plate set-up giving a total effective $L = 5$ mm, which is in the 2nd maxima of the fringe contrast and has an acceptable flow resolution.

4.2.1 Calibration sources

As mentioned before, the design of the narrow-bandpass filter is essential to isolate a plasma emission wavelength. In theory, each visible, well-isolated emission line of the plasma spectrum can be measured with the Doppler CIS. However, only a limited amount of calibration lines available with conventional calibration lamps (cf. Figure 27) or monochromatic, continuous lasers exist.
For the Doppler CIS calibration, intense monochromatic calibration sources at the same wavelength of the un-shifted emission wavelength are optimal. In practice, these calibration sources are rarely available. This is why for many observed plasma lines, calibration wavelengths, $\lambda_{\mathtt{cali}}$, in the vicinity of a few nanometers to the un-shifted plasma wavelength, λ_0, are used. An example is the C III multiplet at 464.881 nm, for which a Zn I calibration line at 468.014 nm was used. In these cases, the analysis of the $\Delta\Phi \rightarrow \Delta\lambda$-relation becomes more difficult for the Doppler CIS (cf. section 3.2.2).

In practice, many interesting plasma lines are not measured with the Doppler CIS due to lack of calibration sources (cf. chapter 7.3). Some possible solutions to the calibration problem exist, however they are more complex and expensive than a calibration lamp. Tunable laser diodes, as e.g. applied in Laser-induced fluorescence diagnostics, have a variety of laser diodes available nowadays. Or variable, monochromatic laser sources such as Titan-sapphire lasers or optical parametric oscillation (OPO) lasers can be used. A newly developed, tunable laser based on OPO provides continuous-wave, monochromatic emission over nearly the entire visible

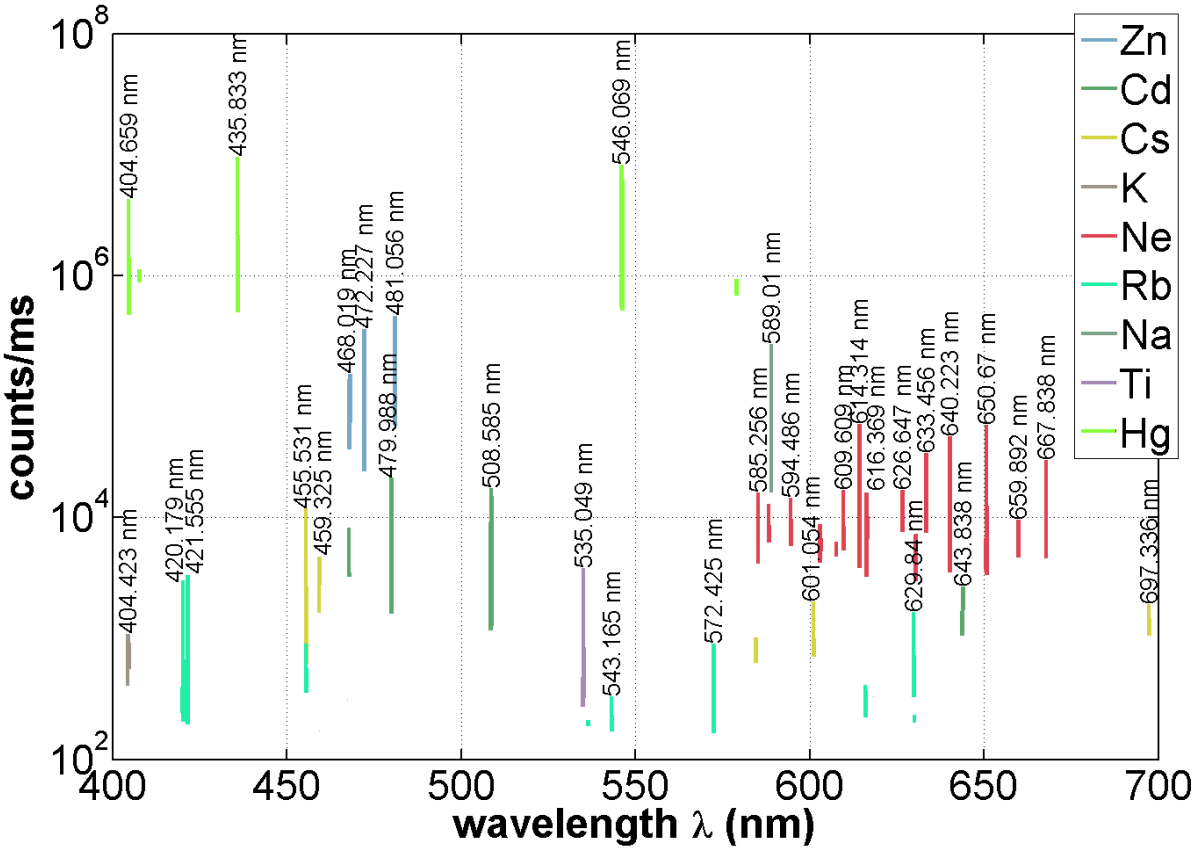

Figure 27 – Calibration wavelengths available with several spectral calibration lamps. The calibration lines were measured with a high-resolution Echelle spectrometer. The Zn I calibration line at 468.014 nm was used for Doppler CIS calibrations in ASDEX Upgrade. With the used camera in the Doppler CIS set-up, an exposure time of 500 ms was necessary for calibration images with good signal-to-noise ratio.

spectrum (450-650 nm) and the near infra-red (900-1300 nm)[20]. Although this in principle solves the calibration issue, it adds significantly to the costs of the CIS system.

4.3 Measurement and calibration procedure

In this subsection, a brief overview is provided on the procedures applied after Doppler CIS measurements.

The variation of the fringe phase is monitored directly before and after each measurement with the calibration source. This can be seen in Figure 28, where the temporal phase evolution of the central camera pixel is illustrated. Over many AUG and VINETA.II discharges, the temporal phase evolution before and after plasma operation demonstrate relatively predictable behaviour, typically decreasing or increasing linearly or remaining constant (as in Figure 28). Phase variations during calibration (where no diagnostic parameter or wavelength are changed) arise due to external parameters such as the ambient temperature at the birefringent plates. If the phase increases or decreases during the calibration (and thus during the measurement as well),

[20] `http://www.hubner-photonics.com/C_WAVE+advanced-p-26.html`

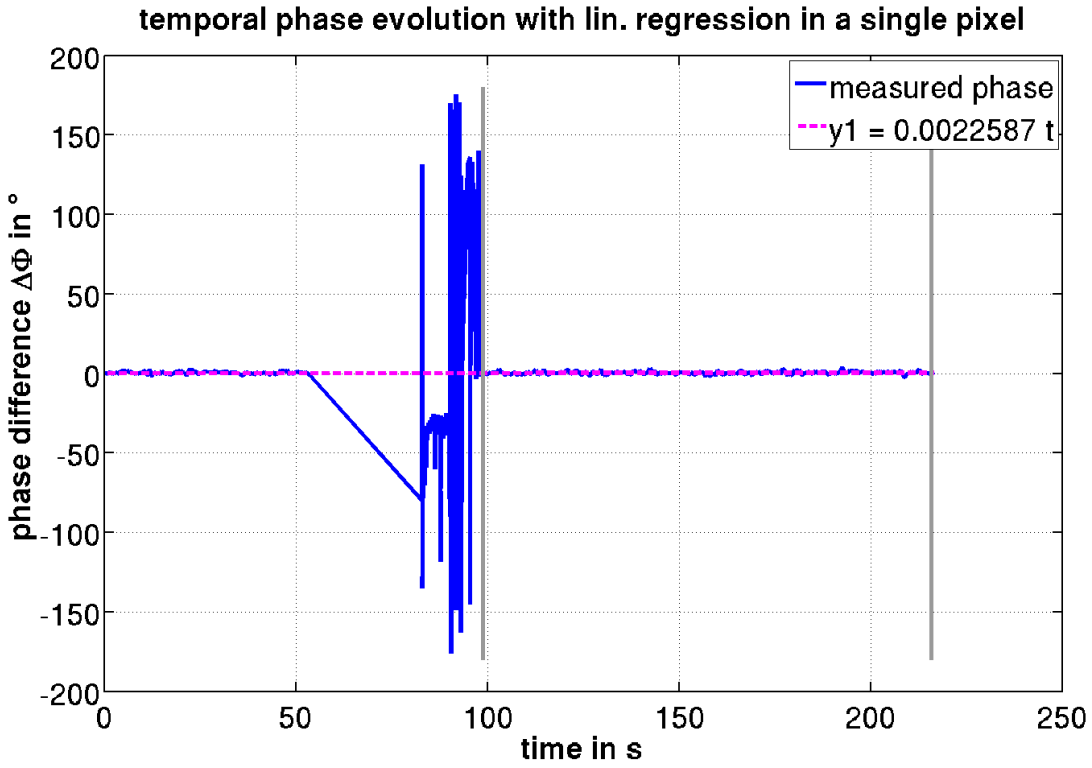

Figure 28 – Temporal evolution of the phase difference $\Delta\Phi$ in the central CCD camera pixel of the Doppler CIS during the first calibration ($t < 50\,\mathrm{s}$), ASDEX Upgrade discharge 33666 ($70 < t < 100\,\mathrm{s}$) and the second calibration ($t > 100\,\mathrm{s}$). For this specific plot, the phase of the first calibration image is subtracted from all following phase images to display the phase difference.

a linear regression is used to estimate the phase change during the measurement and subtract it from the measurement phase. With this method, active or passive temperature control[21] is not necessary to avoid a measurement phase offset due to ambient plate temperatures. The phase errors arising due to this method are $\Delta\Phi \ll 1\,^\circ$. Generally, it is observed that with only α-BBO plates, the phase changes with ambient temperature are much less over e.g. a time of $\approx 200\,\mathrm{s}$ than e.g. with LN. These observations are in agreement with measurements conducted previously [21].
As is suggested by ([51]), single pixel noise caused by radiation (e.g. neutrons) in the AUG Doppler CIS images are removed by median averaging before applying the Fourier transform analysis.

4.4 Summary

For the VINETA.II and AUG Doppler coherence imaging measurements, a diagnostic set-up with a steerable mirror is chosen. This enables to calibrate directly before and after each AUG discharge to eliminate phase offsets due to ambient temperature variations.
When the Doppler CIS diagnostic is prepared for measuring the emission and velocity of a

[21] For passive temperature control, birefringent plates with different signs of $\mathrm{d}n_o/\mathrm{d}T$, $\mathrm{d}n_e/\mathrm{d}T$ are combined to effectively eliminate the temperature dependence of the plates.

certain particle species, the following steps must be taken before measuring:

1. Measure the spectral properties of a plasma emission line to be observed with Doppler CIS.

2. Find an intense calibration source close to the un-shifted emission line.

3. Optimise the contrast if the plasma line is a multiplet by choosing a birefringent plate of optimal thickness.

The effect of phase changes caused by environmental parameter changes is observed and estimated with the calibration images. Furthermore, high intensity peaks in single pixels (attributed to neutrons from AUG) are removed before applying the Fourier transform.

5 Results I: Testing the CIS performance and analysis procedure

To investigate the performance of the described Doppler CIS set-up for VINETA.II and ASDEX Upgrade, three different tests were designed. In this chapter, the results of these scenarios are presented. The three tests were the following:

1. The moveable mirror set-up applied for ASDEX Upgrade was varied in its position.
2. The influence of ambient parameters such as plate temperature and magnetic fields on the measured phase difference during an ASDEX Upgrade discharge was investigated.
3. A Doppler CIS measurement of known Doppler shifts was conducted (tunable wavelength scan).

The main intention of the last arrangement was to validate the entire measurement process, including the analysis procedure for the measured phase difference images involving Equation (36). This equation is used to translate the measured phase difference $\Delta\Phi$ of the diagnostic into a wavelength shift $\Delta\lambda$. A detailed description of this analysis is provided in chapter 3.2.2. With the test measurements, a comparison between measured and simulated Doppler shifts was made, thereby testing the operation and understanding of the entire diagnostic hardware and procedure.

5.1 Alignment of the mirror

In the Doppler CIS set-up applied for the ASDEX Upgrade measurements, a full-reflective mirror was connected to a stepper motor. The stepper motor moves the mirror into the path for the calibration and removes it during the plasma measurements (cf. section 4.1). Exact positioning of the mirror and stepper motor is necessary in order to match the path of the calibration light through the plates with that of the plasma. Next to the precise alignment of the mirror, there is a further concern: that the stepper motor might miss one or a few steps when used to move the mirror. To determine how strongly $\Delta\Phi$ is influenced by a misalignment of the mirror, the position of the mirror was varied. For the set-up in the AUG torus hall, a Zn I calibration line at 468.014 nm was used to monitor $\Delta\Phi$ for different positions of the mirror, this can be seen in Figure 29b. As reference or calibration image, the 45 ° orientation of the mirror, which was recorded over the first 10 s, was used (cf. Figure 29a). Each 10 s, the position of the mirror was varied for 2 steps or 0.25 °. This was done 10 times. After that, the position of the mirror was driven back 20 steps (at $t = 130$ s).

In Figure 29b, $\Delta\Phi$ changes rapidly with varying mirror position. The change is not the same for each area in which $\Delta\Phi$ was averaged. In the central (red) and area of the image, $\Delta\Phi$ varies

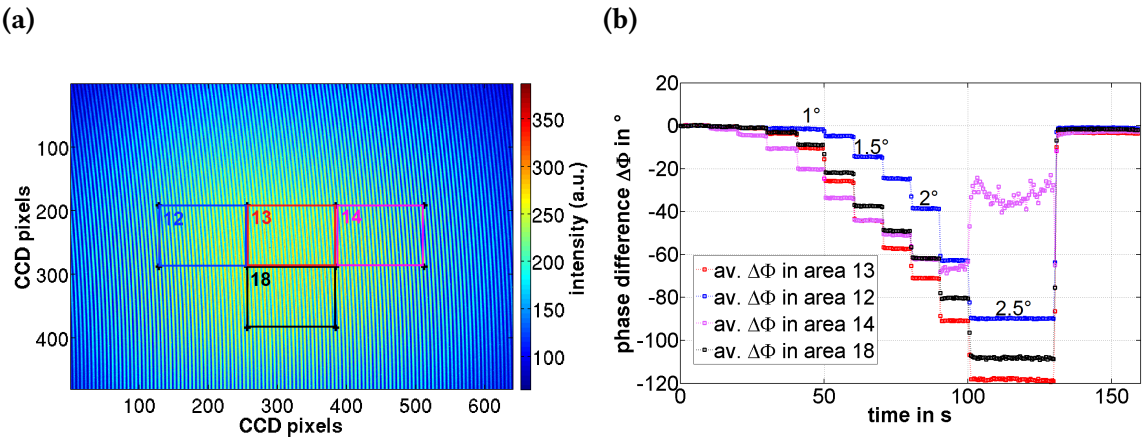

Figure 29 – Observation of the phase difference change $\Delta\Phi$ for $0.25\,^\circ$ steps of the mirror angle in calibration mode (right image). $\Delta\Phi$ was averaged in 25 areas covering the entire measurement image (4 of those are illustrated). As example, the reference image at the ideal mirror position of $45\,^\circ$ is shown (left image). The exposure time for each image was set to 500 ms.

more strongly than in the left or lower averaging areas. This was also tested (but not shown) with smaller averaging areas on the image. For different mirror positions, the illumination paths of the light collimated on a single CCD pixel change through the birefringent plates. In some averaged areas on the CCD chip, $\Delta\Phi$ becomes noisy over time, since the illuminated area was shifted out of the right part of the image. $\Delta\Phi$ did not change strongly for 2 missed steps out of the nominal position, but the more the mirror is out of position, the stronger the $\Delta\Phi$ offset becomes (e.g for $1.25\,^\circ$, there is a considerable deviation of $\Delta\Phi > 20\,^\circ$ for three of the selected areas of the image). After driving back in the initial position after the mirror misalignment, the average phase differences varied between $\Delta\Phi \approx -3\,^\circ$ and $-1\,^\circ$, due to slight temperature variations and possibly a miss of 1 step by the steering program of the mirror.

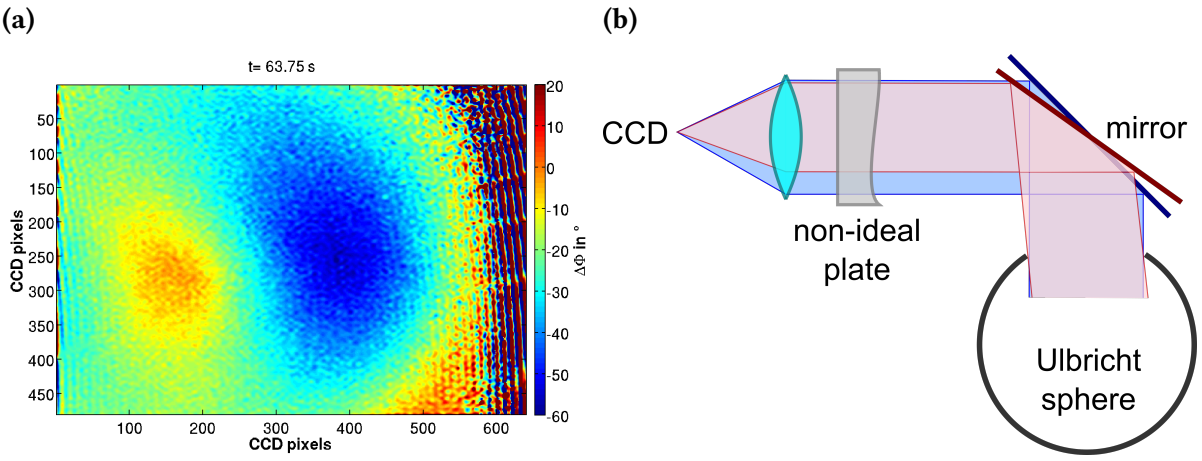

Figure 30 – Left image: $\Delta\Phi$ offset at a mirror position $1.5\,^\circ$ off the $45\,^\circ$ standard position. Right image: schematic of the Doppler CIS system with the correct mirror position (blue) and a misaligned one (red).

An image of the $\Delta\Phi$ offset due to an incorrect mirror position can be seen in Figure 30. In the left half of the image, $\Delta\Phi$ changes less strongly than in the right part. The change of $\Delta\Phi$

for different mirror positions should not be encountered in the case of ideal birefringent plates (uniform plate thickness and homogeneity over the entire surface). The measured phase offsets are an indication that the plates are not homogeneous. By the misalignment of the mirror, the light takes a different path through the birefringent plate's volume (cf. Figure 30b). If the plate has e.g. a varying thickness over its entire volume, then the phase will become different at the same pixel for the same wavelength for another path through the birefringent plates.

The procedure showed a reproducibility sufficient to induce an error of less than 3 ° in the calibration phase. Given this sensitivity, to ensure that the mirror always hits the 45 ° calibration position, a mechanical stop was added to the Doppler CIS set-up. Each time the stepper motor drove the mirror into the calibration position, a few more steps were added than actually necessary. This was done to prevent the motor missing the correct position in case that some steps are not performed.

5.2 Doppler CIS performance prior, during and after AUG discharges

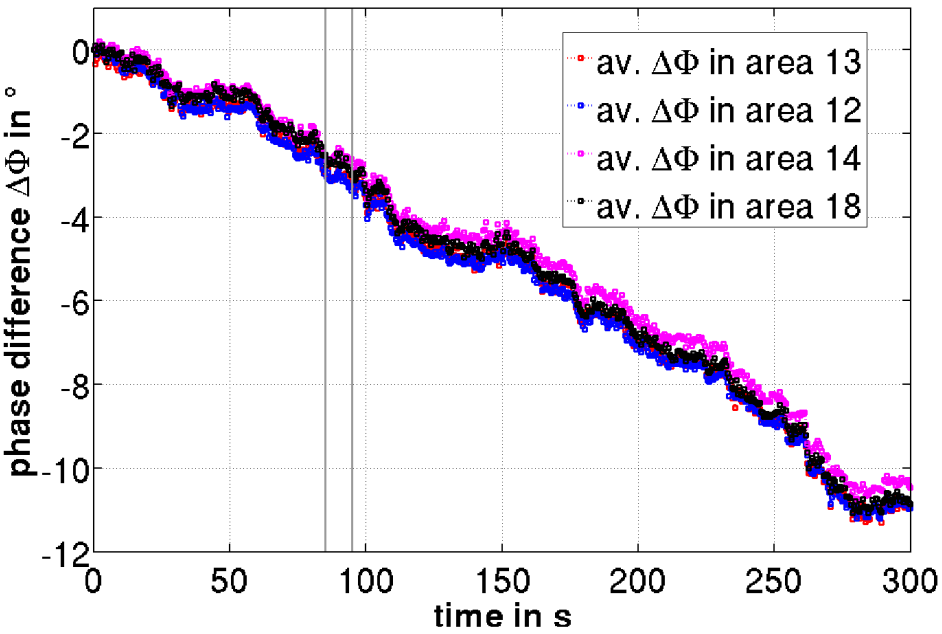

Figure 31 – Temporal change in $\Delta\Phi$ measured from the Zn calibration source before, during and after ASDEX Upgrade discharge 33582. The phase Φ of the first measurement image was used as a reference image. The mirror was in calibration position. The recorded $\Delta\Phi$ during the AUG discharge is marked by two grey lines. $\Delta\Phi$ was averaged in the 4 areas as in Figure 29.

The ambient diagnostic (air) temperature was observed and reported to have a large influence on the performance of the Doppler CIS diagnostic [21]. To estimate the influence of this and possible other external effects on the birefringent plates (such as maybe a change of the

magnetic field before and after a discharge), an investigation of the temporal $\Delta\Phi$ evolution before, during and after an AUG plasma discharge was made for a fixed observed wavelength. With the Zn spectral lamp line at 468.014 nm, Doppler CIS images were measured in calibration mode. In Figure 31, the averaged temporal $\Delta\Phi$ evolution is shown. There is a roughly linear $\Delta\Phi$ drop over time of $\frac{\partial(\Delta\Phi)}{\partial t} \approx 0.04\,^\circ$/s. This decrease is most likely caused by an ambient temperature change of the surrounding air and the birefringent plates. Shortly before and after, as well as during the ASDEX Upgrade discharge, the temporal $\Delta\Phi$ change seems not to be affected by any additional rapid process (such as the magnetic field ramp up/down). Furthermore, the temperature-induced $\Delta\Phi$ changes are rather homogeneous over the CCD image. There is only a small variance of about $\Delta(\Delta\Phi) = 0.5\,^\circ$ for the averaging areas in the image.
There are some short, temporary periods with faster changes in Figure 31, interestingly all decreasing. This might possibly be temperature sources caused by ASDEX Upgrade operation. However, $\Delta\Phi$ is well approximated by a linear change during the measurement and calibration process of the diagnostic. Thus, the before/after calibration method is sufficient for this work.

5.3 Tunable diode laser scan

An important assumption for the applied Doppler CIS analysis in this work is that the change of $\Delta\Phi_{\mathtt{meas}}$ for a certain Doppler shift $\Delta\lambda$ can be accurately predicted with the Equation (36). This requires the birefringent indices n_e, n_o to be accurately known. Furthermore, diagnostic parameters such as L, θ, the pixel where $\alpha = 0\,^\circ$ and focal length f of the CCD lens are only known to a certain degree, but not with ultimate precision (cf. chapter 3.2.2). These small uncertainties cause phase offsets that might affect how $\Delta\Phi_{\mathtt{meas}}$ changes for a given Doppler shift $\Delta\lambda$.
The observed Doppler shifts in VINETA.II and ASDEX Upgrade are up to 3 pm and 40 pm, which correspond to particle velocities of 2 km/s and 25 km/s, respectively[22]. To test the simulated $\Delta\Phi_{\mathtt{meas}}/\Delta\lambda$ dependence(s), a monochromatic light source with a wavelength tunable in the picometer range is necessary. This can be achieved with a cavity diode laser. For the test performed here, an cavity diode laser in Littman configuration was used[23]. These systems enable high output power on the order of 200 mW as well as low linewidth (<$2 \cdot 10^{-6}$ nm) in continuous operation mode and with a tunable wavelength. The laser is part of a laser-induced fluorescence (LIF) diagnostic and therefore abbreviated with LIF laser. Figure 32a shows is a photo of the tunable diode laser interior. A commercial laser diode with a broad emission spectrum of roughly 20 nm serves as the laser's light source. A temperature control unit needs

[22]The flow sensitivity of the Doppler CIS diagnostic is appropriately adjusted by the use of more or less birefringent delay plates.

[23]Technical Details: TEC-420-0670-0500 LION Tunable Littman/Metcalf External Cavity Diode Laser by Sacher Lasertechnik GmbH (`https://www.sacher-laser.com/home/scientific-lasers/tapered_amplifiers/amplified_tunable_laser/mopa_amplified_tunable_diode_laser_system_servalplus.html`)

to be used to keep the laser diode and amplifier diode at a constant temperature. With a diffraction grating, a distinct wavelength is selected from the laser diode's spectrum. By the application of a piezo element, the grating and thus the selected wavelength can be steered by applying a voltage. This is shown in Figure 32b. Approximately 10% of the laser light are separated from the main optical path by a half-reflective mirror. A fibre was used to direct this light into a wavemeter to record the exact tunable diode laser wavelength. The remaining 90% of the output light was directed to the Doppler CIS calibration sphere, from where the image fibre bundle directed the light to the optical set-up of the diagnostic.

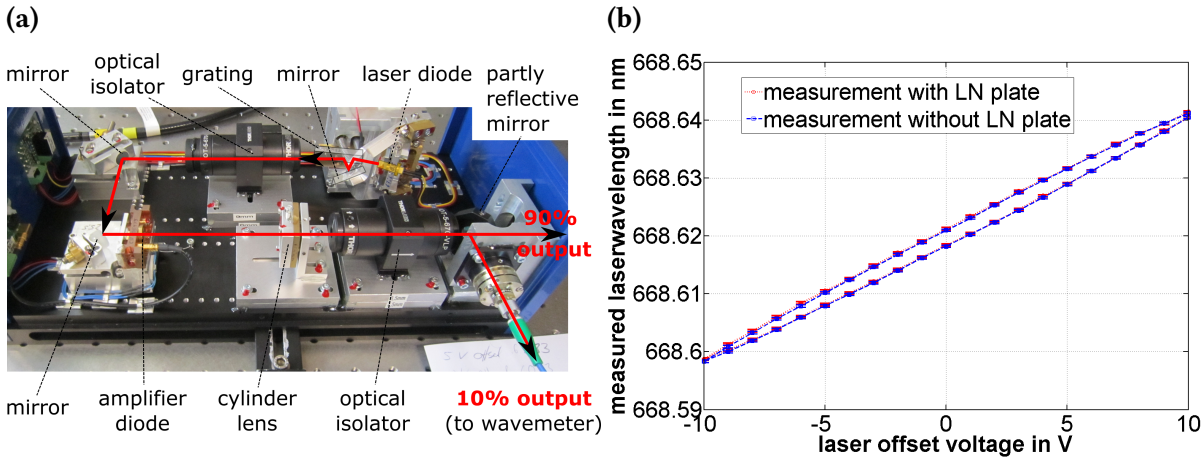

Figure 32 – Left image: interior view into the LION tunable diode laser. The path of the laser light is schematised in red. The grating, first mirror and the laser diode were distinguished schematically for better identification. Right image: measured tunable diode laser wavelength as a function of piezo voltage for two performed scans with the Doppler CIS.

With the LIF laser, a comparison between the measured phase differences for precisely known laser wavelengths and the simulated phase differences for the same wavelengths was conducted. The LIF laser wavelength was varied between 668.6414 nm and 668.5987 nm. Since the LIF laser line is very monochromatic, its wavelength could be measured to an accuracy of ± 0.1 pm with a wavemeter. The wavelength was decreased and increased again in order to separate the actual $\Delta\Phi$ dependence on $\delta\lambda$ from other $\Delta\Phi$ time dependencies such as on the ambient temperature. As can be seen in Figure 32b, the LIF laser wavelength was not the same during the decrease and increase of the applied laser voltage. This is caused by the automatic regulation of the laser voltage and temperature control unit, that behaves differently for different tuning paths. However, this is irrelevant due to the wavemeter measurements.
During first attempts of the LIF laser scan with the Doppler CIS diagnostic, an ambient temperature-caused drift of the measured phase difference was observed. Since the Doppler CIS set-ups on VINETA.II and ASDEX Upgrade did not involve a temperature cell for the birefringent plates, no temperature cell was used during the LIF laser scan either. To assess the (assumed) temperature effects on the measured phase difference, the following actions were taken:

1. Each wavelength was measured for 10 s to keep the overall measurement time (and thus temperature drift) low.

2. An additional (fixed) wavelength was simultaneously measured during the LIF laser scan to monitor the temperature effect on the measured phase difference.

As additional fixed wavelength, an Ar laser line at 488 nm was used. Two distinct wavelengths can be successfully measured with the same Doppler CIS camera at the same time if they form two separable peaks in Fourier space. The simultaneous measurement of two wavelengths goes at the cost of spatial resolution, since the area in Fourier space becomes smaller. The distance of two peaks in the Fourier space depends on the wavelengths (and the fringe size). The fringe size in pixel units depends on the displacer plate thickness, the wavelength and the size of the CCD camera pixels. The same CCD camera and displacer plate were used in all measurements presented in this work. For their settings, a wavelength difference on the order of 100 nm was typically necessary to generate two separated peaks in the Fourier image.[24]
In Figure 33a, the interferometer signal generated by the two monochromatic laser wavelengths is shown. It consists of two overlaying modulation patterns. The corresponding Fourier transform image is in Figure 33b. The Fourier peaks appear relatively broad because many delay plates were used resulting in strong fringe curvature and frequency shear.
The LIF laser scan was performed twice, for two different plate configurations. The first configuration consisted of a 5.4 mm α-Barium Borate (α-BBO) displacer plate, three 10 mm α-BBO delay plates and a 7.5 mm Lithium Niobate (LN) delay plate. For the second plate configuration, the 7.5 mm LN delay plate was removed.

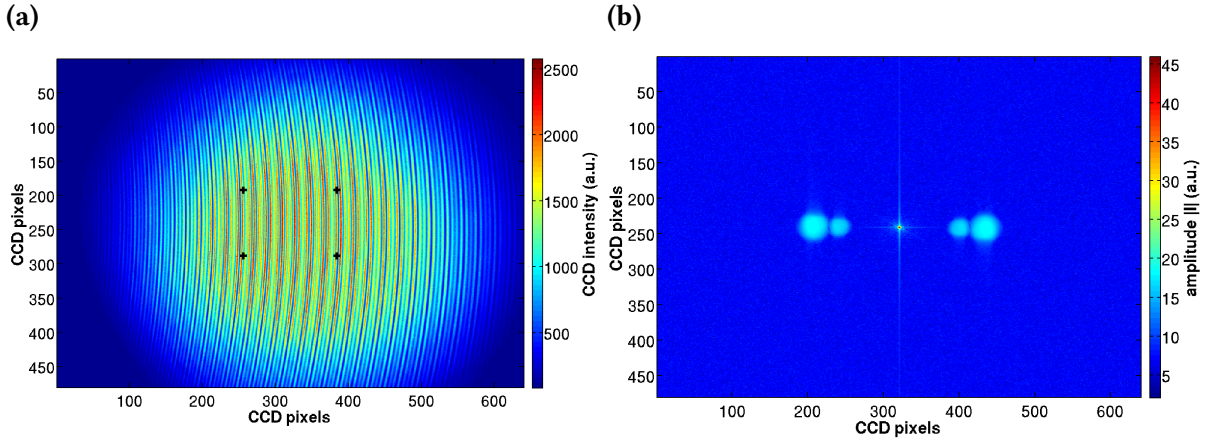

Figure 33 – Doppler CIS interferometer signal recorded with the tunable LIF laser (668.6412 nm) and the Ar ion laser (487.986 nm) (left) and its Fourier transform image (right). The black markers in the interference image indicate the area in which the phase difference was averaged.

In Figure 34, the temporal evolution of the LIF laser phase difference and the Ar laser phase difference are shown for both plate configurations. The LIF laser wavelength was first decreased

[24]The separability is also dependent on the spectral broadening, information content of the images and number of delay plates in use. All of them influence the broadening of the Fourier peaks and they might overlap, depending on the mentioned conditions.

and then increased every 10 s for about 2 picometers. This is why the temporal evolution of the LIF laser phase difference appears like a pyramid. For the plate configuration including the 7.5 mm LN delay plate, the overall phase difference was larger. The Ar ion laser line, λ_{Ar}, remained unchanged throughout the entire measurement. However, the temporal evolution of the Ar signal phase difference shows a nearly linear decrease for both plate configurations. This is due to an ambient temperature change that induces a change of the birefringent indices. The temperature-caused phase difference drift is stronger for the plate configuration including the LN delay plate. This has also been reported and investigated in other Doppler CIS set-ups [21]. The LN plates have a much stronger dependence on the ambient temperature than the α-BBO plates. With the LN plate, the temperature drift corresponds to $\Delta\Phi_{\mathtt{drift}} \approx 50\,^{\circ}$, without it is only $\Delta\Phi_{\mathtt{drift}} \approx 7\,^{\circ}$ for the Ar laser wavelength. Furthermore, the temperature induced $\Delta\Phi$ drift is less strong for the LIF laser (668.6 nm) than for the Ar laser line (at 488 nm). It is due to the temperature drift that $\Delta\Phi_{\mathtt{meas,LIF}}$ does not equal a value close to 0 for the last set LIF laser wavelength, despite that the last set laser wavelength was only 1 pm from the first set wavelength of the scan.

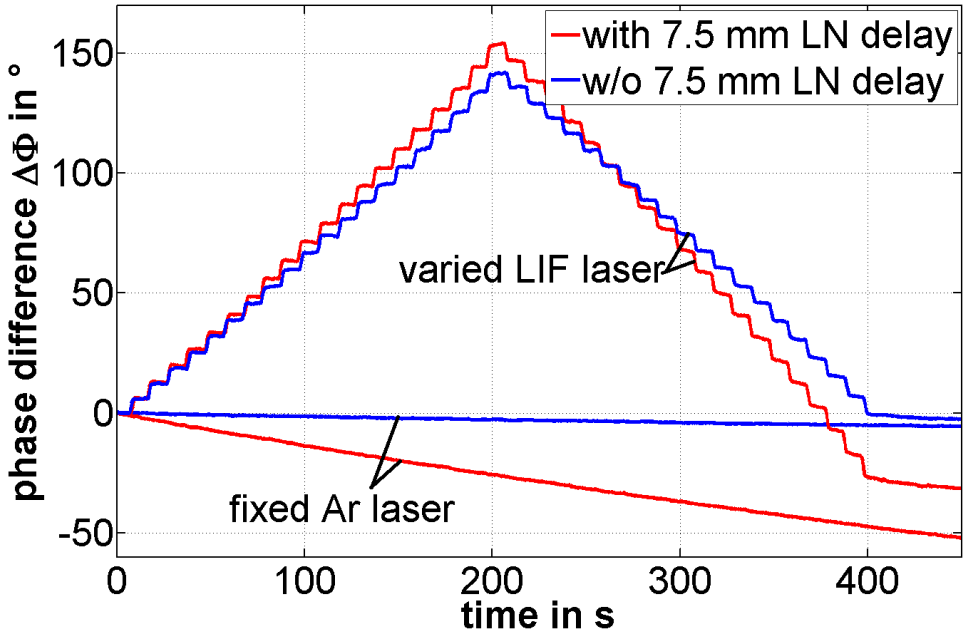

Figure 34 – Tunable laser wavelength scan of the Doppler CIS set-up used in VINETA.II and AUG. The measured phase differences $\Delta\Phi$ for two different plate configurations (different colors) and two different laser wavelengths (one fixed, one varied) are shown, averaged in the central area of the Doppler CIS images (marked in Figure 33a). Both plate configurations included a 5.4 mm α-BBO displacer and three 10 mm α-BBO delay plates. As reference image, the first measurement image was taken for both wavelengths, respectively.

To eliminate the temperature drift in the measured phase difference of the LIF laser, $\Delta\Phi_{\mathtt{meas,Ar}}$ was subtracted from $\Delta\Phi_{\mathtt{meas,LIF}}$. Since the temperature-dependent $\Delta\Phi$-drift is in general wavelength-dependent and different for the two laser lines, the ratio of $\Delta\Phi_{\mathtt{meas,LIF}}$

and $\Delta\Phi_{\mathrm{meas,Ar}}$ was determined. For this calculation, it is assumed that the effect of the ambient temperature T on the birefringence B at the two wavelengths has a fixed ratio. It was determined by the mean of the last adjusted LIF laser wavelength between $t = 400 \ldots 450\,\mathrm{s}$. Thus, the measured LIF laser phase difference was corrected as follows:

$$\Delta\Phi'_{\mathrm{meas,LIF}} = \Delta\Phi_{\mathrm{meas,LIF}} - \Delta\Phi_{\mathrm{meas,Ar}} \cdot \frac{\sum_{t=400\mathrm{s}}^{450\mathrm{s}} \Delta\Phi_{\mathrm{meas,LIF}}}{\sum_{t=400\mathrm{s}}^{450\mathrm{s}} \Delta\Phi_{\mathrm{meas,Ar}}} \tag{43}$$

The corrected $\Delta\Phi'_{\mathrm{meas,LIF}}$ as well as the simulated phase difference $\Delta\Phi^*$ are plotted in Figure 35a. There are small deviations of up to $\approx \pm 3\,^\circ$ between $\Delta\Phi'_{\mathrm{meas,LIF}}$ and the simulated phase difference $\Delta\Phi^*$ (cf. Figure 35b) for both plate configurations. This corresponds to a wavelength shift of $\pm 0.8\,\mathrm{pm}$ (for plate configuration including the LN plate) and $\pm 0.6\,\mathrm{pm}$ (only α-BBO plates). They are most likely due uncertainties in the plate parameters and maybe also variations of the LIF laser, that were not recorded. The deviation is consistent with and without LN plate in separate runs. The LIF laser wavelength was sometimes varying about $\pm 0.2\,\mathrm{pm}$ around its set value because of the automatic regulation of the laser diode temperature. However, this suggests it's a systematic error and not due to random error changes. There is a good agreement between $\Delta\Phi'_{\mathrm{meas,LIF}}$ and $\Delta\Phi^*$, demonstrating the accuracy of the diagnostic (described in detail in chapter 3.2.2). The variation of $\Delta\Phi$ over $\Delta\lambda$ can be described with Equ. (15) and known birefringent indices, although some parameters (such as plate inhomogeneities and the exact effective focal length of the CCD imaging lens) are not known precisely.

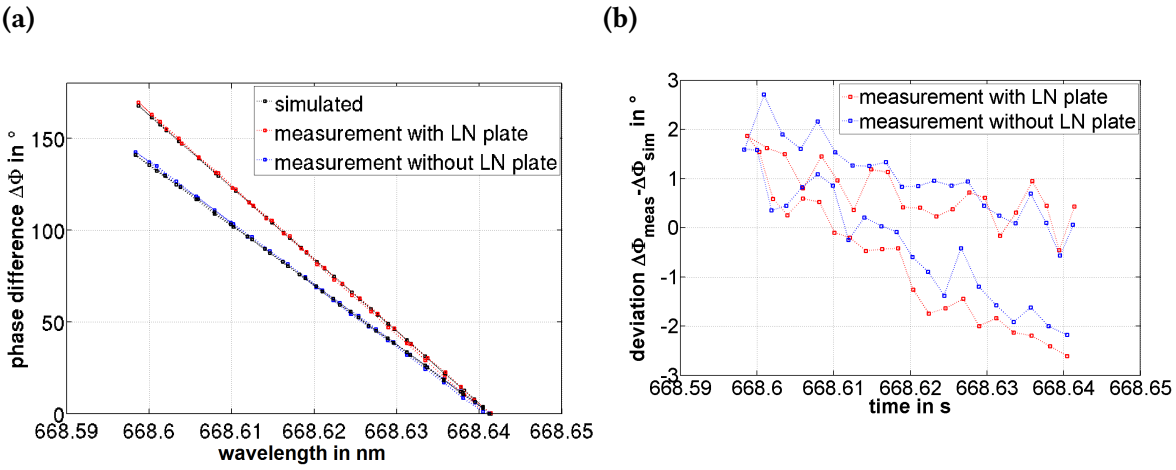

Figure 35 – (a) Corrected $\Delta\Phi'_{\mathrm{meas,LIF}}$ (red and blue) and simulated (black) $\Delta\Phi^*$ for two different plate configurations during the tunable wavelength scan, averaged in the central area of the image. Both plate configurations included a 5.4 mm α-BBO displacer and three 10 mm α-BBO delay plates. The red line included an additional 7.5 mm LN delay plate. (b) Subtraction of measured and simulated $\Delta\Phi$ to highlight the deviations.

5.4 Summary of Doppler CIS test measurements

Test measurements of the Doppler CIS diagnostic were conducted to quantify the accuracy and performance of the Doppler CIS operation. The variation of the half-reflective mirror position in calibration mode demonstrated a $\Delta\Phi$ offset for the mirror in case of a misalignment. This is due to birefringent plate inhomogeneities, as was systematized in Figure 30b. It resulted in a precautionary measure to make sure that the mirror is always in the correct position during calibration.

A test calibration measurement was performed before, during and after an ASDEX Upgrade discharge. This was done to check if there are $\Delta\Phi$ offsets due to e.g. the presence of the ASDEX Upgrade magnetic field or sudden temperature changes. No additional offsets could be measured and the before/after calibration method was shown to be sufficient to compensate observed temperature drifts.

A tunable diode laser wavelength scan was performed to test the accuracy of the Doppler CIS demodulation and simulation routines. A deviation of about $\pm 2^\circ$ per $L = 32.2\,\text{mm}$ of delay plate material was observed when comparing the simulated and measured phase differences over a wavelength range of 40 pm. This deviation is presumably caused by plate parameter uncertainties and possibly a temperature drift of the applied tunable laser. For AUG measurements, this means an error estimation of less then 1° for the $\Delta\Phi$ dependence on $\Delta\lambda$ for a cumulative delay plate thickness of $L < 5\,\text{mm}$ for the expected wavelength shifts (30-40 pm, corresponding to 20-25 km/s). However, additional $\Delta\Phi$ offsets to that relation could be added by additional terms in the analysis (such as offsets due to multiplet structures or calibration lines further away from the un-shifted plasma emission line, cf. section 3.2.2).

An additional (fixed) laser line was measured simultaneously with the Doppler CIS to estimate temperature drift effects on the measured phase differences. The ambient temperature considerably distorted the measured phase difference during the length of the laser scan. To the knowledge of the author, a successful simultaneous measurement of two wavelengths has not been performed with the Doppler CIS diagnostic before and could be a technique worth developing for dual wavelength measurements in plasmas. The simulated and measured variation of the phase difference with wavelength shifts were found to match each other convincingly well.

In the next two chapters, the Doppler CIS measurements in VINETA.II and ASDEX Upgrade are presented.

6 Results II: VINETA.II flows

VINETA.II is a linear plasma experiment dedicated to the study of driven magnetic reconnection [59]. One goal of this thesis was to investigate whether ion dynamics during a magnetic reconnection event could be observed with the Doppler CIS in VINETA.II. To understand the underlying basic ion dynamics in VINETA.II (without reconnection) and to estimate which equipment for the diagnostic is necessary for the detection of flows produced by the driven magnetic reconnection, Doppler CIS measurements were performed without magnetic reconnection.
The research and comprehension of magnetic reconnection is of interest for astrophysical phenomena, where it is thought to play an important role in e.g. solar flares and the Earth's magnetosphere. In magnetic confinement fusion research, some plasma dynamics such as sawtooth instabilities are connected to magnetic reconnection as well. However, despite intense research on the topic in the last decades, existing models are insufficient to predict magnetic reconnection in nearly collisionless plasmas [60]. One major unresolved issue is exactly how magnetic energy is converted to kinetic energy of the electrons and ions during the process [59],[61]. The study of ion dynamics during a magnetic reconnection event could improve understanding of the process in general, e.g. how much magnetic energy is converted to ions, as well as be used for the validation of existing models. This is why it is investigated whether the Doppler CIS could be used for the study of magnetic reconnection in a near-collisionless, low-temperature plasma experiment or not.

The Doppler CIS enables the detection of very small ion flows on the order of hundred meters per second ([21]). It collects a large amount of spatial information and is a non-invasive method to measure the ion flow. This is why it is very attractive for the study of ion dynamics during a driven magnetic reconnection cycle in VINETA.II, where the flows induced by magnetic reconnection are expected to be small. However, even in a small linear plasma experiment like VINETA.II, ion dynamics are a compound of several drifts that need be assessed individually first in order to differentiate them. Some of these ion dynamics are related to the magnetic reconnection process and some of them are not.
In the next subsections, a basic overview of the VINETA.II experiment and its plasma parameters will be provided. Spectral measurements to determine the plasma emission lines in VINETA.II were made to investigate which lines can be observed with the Doppler coherence imaging diagnostic. In section 6.3, plasma parameters measured with Langmuir probes will be presented, followed by an estimation of the expected ion flows in VINETA.II during an electron cyclotron resonant heating (ECRH) discharge without the reconnection drive. They are compared with the Doppler CIS measured ion flows in VINETA.II. At the end of this chapter, an outlook on the necessary equipment for a Doppler CIS measurement during a magnetic reconnection event is presented. An overlook of the different ion drift effects in VINETA.II is given as well.

6.1 Overview of the VINETA.II Experiment

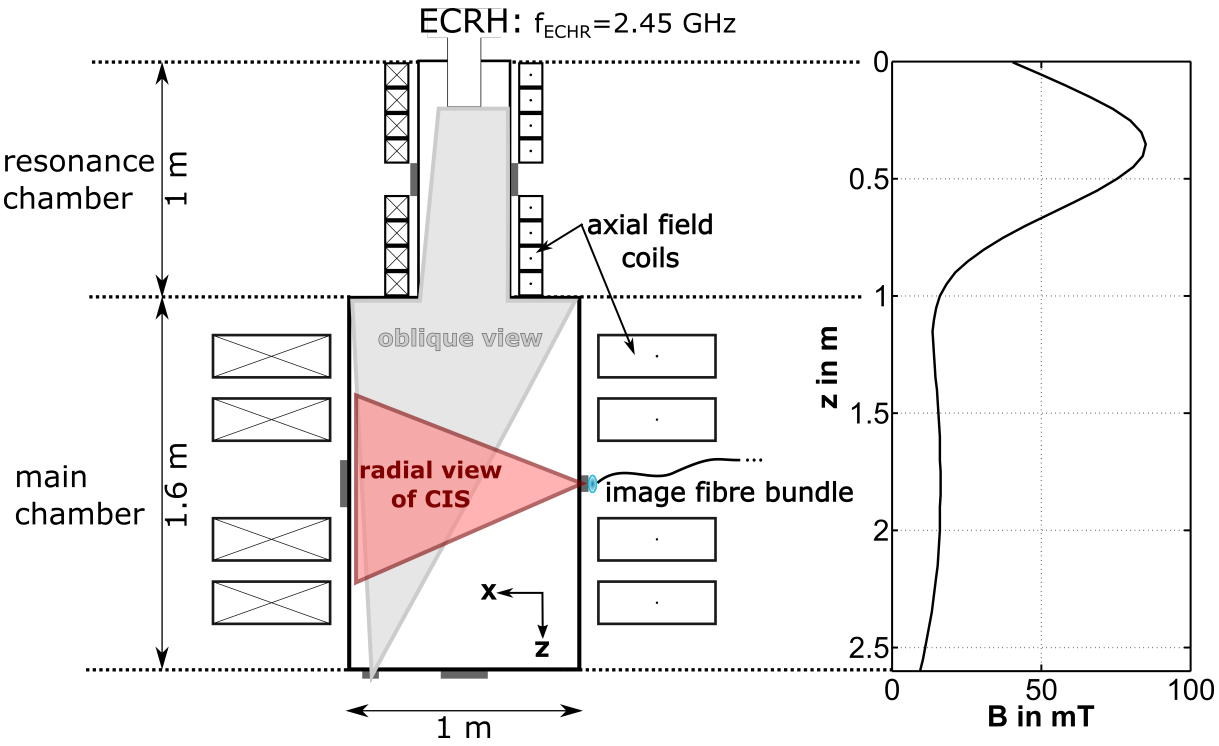

Figure 36 – Schematic view from above on VINETA.II (left) and the magnetic field component along the z-axis generated by its coil system (right). The red viewing area was used for spectral and Doppler CIS measurements. The views into VINETA.II presented in Figure 38 correspond to the grey viewing area.

VINETA.II is a linear magnetized plasma experiment which consists of a large cylindrical stainless steel vessel with a diameter of 1 m and a length of 1.6 m, referred to as the main chamber in this work. In the main chamber, a nearly homogeneous axial magnetic guide field is generated by a set of four large coils.
For plasma generation and heating, an electron cyclotron resonant heating (ECRH) source with a total power of 5 kW is used. For ECRH application, an additional smaller cylindrical vacuum chamber with 0.4 m diameter and a length of 1 m is used. The magnetic coils of the additional chamber generate a magnetic field that the ECRH waves are resonant to, therefore this chamber is denoted as resonance chamber. An overview of the current VINETA.II set-up and its axial magnetic field component is provided in Figure 36.

In its current design, VINETA.II is operated with a 2.45 GHz microwave ECRH source. By applying the ECRH, higher electron temperatures at lower densities could be achieved compared with previous heating sources (a spiral and a helicon RF antenna). Continuous plasma operation with total heating powers from $P_{\mathrm{ECRH}} = 1$ up to 5 kW is possible. The initial gas pressure may range from $p_{\mathrm{gas}} = 1$ to 0.01 Pa with the ECRH. As operation gas, mostly argon is used. An overview of the current VINETA.II parameters with ECRH operation is provided in Table 2. Depending on the ECRH power and gas pressure, different plasma densities, electron

temperatures and emission lines are observed in this set-up of VINETA.II. They were studied in more detail with an echelle grating spectrometer and a Langmuir probe. These measurements will be described in more detail in the next two subsections of this chapter.

parameter	**value**
guide B-field	$\leq 15\,\mathrm{mT}$
argon pressure	$0.01 - 1\,\mathrm{Pa}$
plasma density	$10^{17} - 10^{19}\,\mathrm{m}^{-3}$
electron temperature	$1 - 10\,\mathrm{eV}$
ion temperature	$\approx 0.03\,\mathrm{eV}$
ECRH frequency	2.45 GHz
ECRH power	1-5 kW

Table 2 – Operation parameters of VINETA.II with an ECRH plasma source.

6.2 Line Spectrum of the VINETA.II discharges

Spectral investigations of the VINETA.II plasmas were made to determine which plasma emission lines are available for the Doppler CIS at different operation parameters.
In VINETA.II, the following noble gases are available for plasma generation: argon, helium and neon. All three elements were spectrally investigated for possible CIS measurements. The preferred discharge gas in VINETA is argon, as it has the lowest first ionization energy (15.8 eV) in comparison with helium (24.6 eV) and neon (21.6 eV). The application of a non-noble gas like hydrogen is not allowed in VINETA, since it requires a laboratory license.
The spectral investigations presented in this subsection[25] demonstrate that only in the case of argon ion emission lines can be observed and this only for a restricted set of plasma operation parameters.

Figure 37 shows an overview spectrum of an argon discharge in VINETA.II. For low-temperatures, a dense bulk of Ar I and Ar II emission lines can be observed in the spectral range between 350 and 500 nm. In the red part and the near infrared of the spectrum, there are a few intense Ar I emission lines. Overall, VINETA.II argon plasmas appear violet, as in Figure 38.

The spectral plasma parameters vary considerably over the operation range of VINETA.II. In Figures 38 and 39, argon plasmas at two different operational settings can be distinguished.

[25] A broadband echelle spectrometer (type ESA 3000 of LLA instruments GmbH) [62] was used for most spectral measurements. This spectrometer allows for emission spectra in the range from 200 to 800 nm with a spectral resolution of several picometers. The spectrometer exposure time can be varied between some nanoseconds up to 90 ms. For the VINETA.II plasmas, exposure times in the range between 10 ms to 90 ms were needed to get a good signal-to-noise ratio.

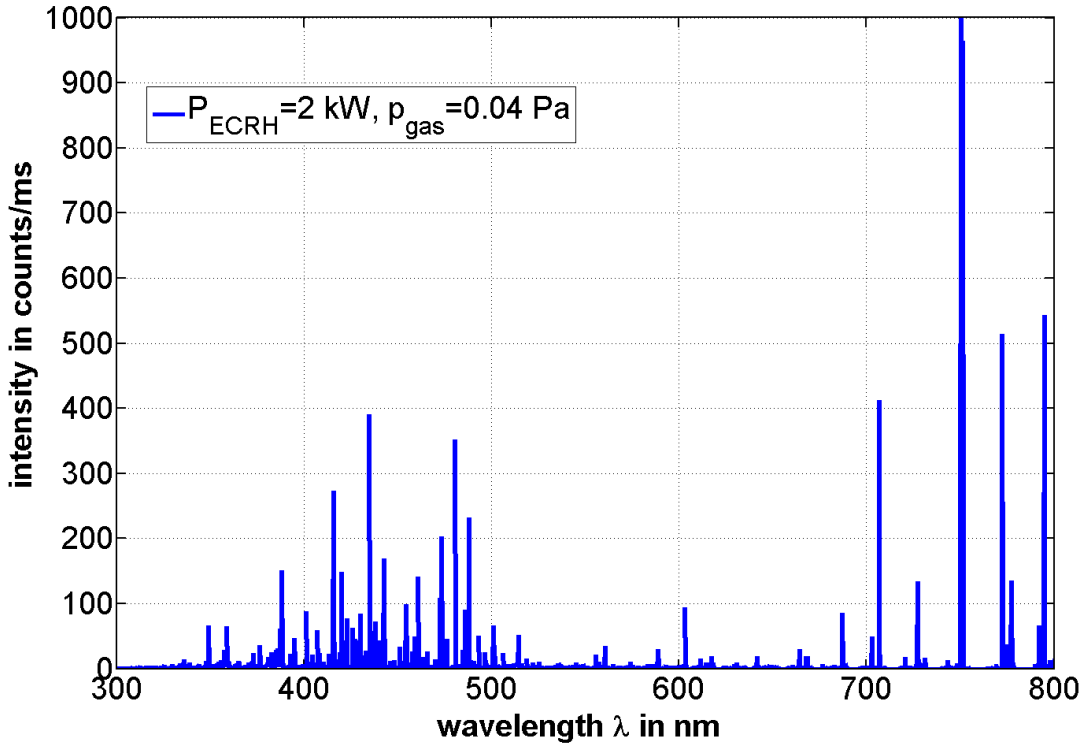

Figure 37 – Emission spectrum in the visible range from an argon plasma in VINETA.II measured with a broadband echelle grating spectrometer. The spectrometer was modified to block several small spectral intervals in the range between 550 until 800 nm, including Balmer H-α line ($\lambda = 656.2$ nm) that tends to oversaturate the spectrometer CCD chip in hydrogen plasmas.

The main parameters that can be modified in VINETA.II discharges are the ECRH power P_{ECRH} and the initial neutral gas pressure p_{gas}. The magnetic field strength in the main chamber may also be varied. This sometimes requires a rearrangement of the coils around the resonance chamber (in order to avoid a magnetic well between the resonance and the main chamber).

Depending on the applied ECRH power and initial neutral gas pressure, different line intensities as well as line compositions are emitted by the plasma. Figure 39 gives an overview of a part of the visible spectrum for two different cases of operation parameters. In the case of low ECRH power and moderate initial gas pressure, the plasma line radiation in the main chamber is low. The spectrum consists only of neutral argon atom line radiation (Ar I). In the case of higher ECRH power and lower initial gas pressures, a spectrum consisting of Ar I and Ar II line radiation can be observed. In this case, the plasma column along the magnetic axis appears more homogeneous and most line intensities in the main chamber are considerably higher. Sufficient line intensity in the main chamber is important for the Doppler CIS, since it determines the signal-to-noise ratio and exposure time for the measurement images. Furthermore, ion dynamics can only be observed if Ar II lines are present. Thus, higher ECRH powers and low neutral gas pressures are required for Doppler CIS measurements in VINETA.II. There are intense Ar II lines in the blue and turquoise part of the spectrum at 434 nm, 480 nm

(a) (b)

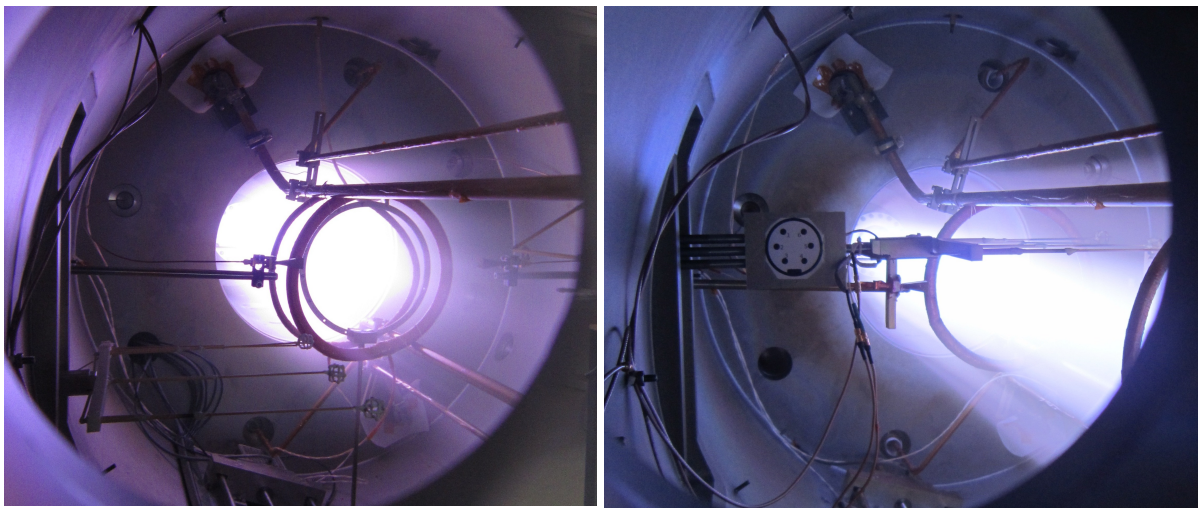

Figure 38 – View into the VINETA.II device during an argon discharge with (a) low power $P_{\mathrm{ECRH,\,abs.}} \approx 900\,\mathrm{W}$ and moderate pressure $p_{\mathrm{gas}} = 0.12\,\mathrm{Pa}$ and (b) moderate power $P_{\mathrm{ECRH,\,abs.}} \approx 2000\,\mathrm{W}$ and low pressure $p_{\mathrm{gas}} = 0.04\,\mathrm{Pa}$. The viewline through the main and resonance chamber is schematically indicated in Figure 36.

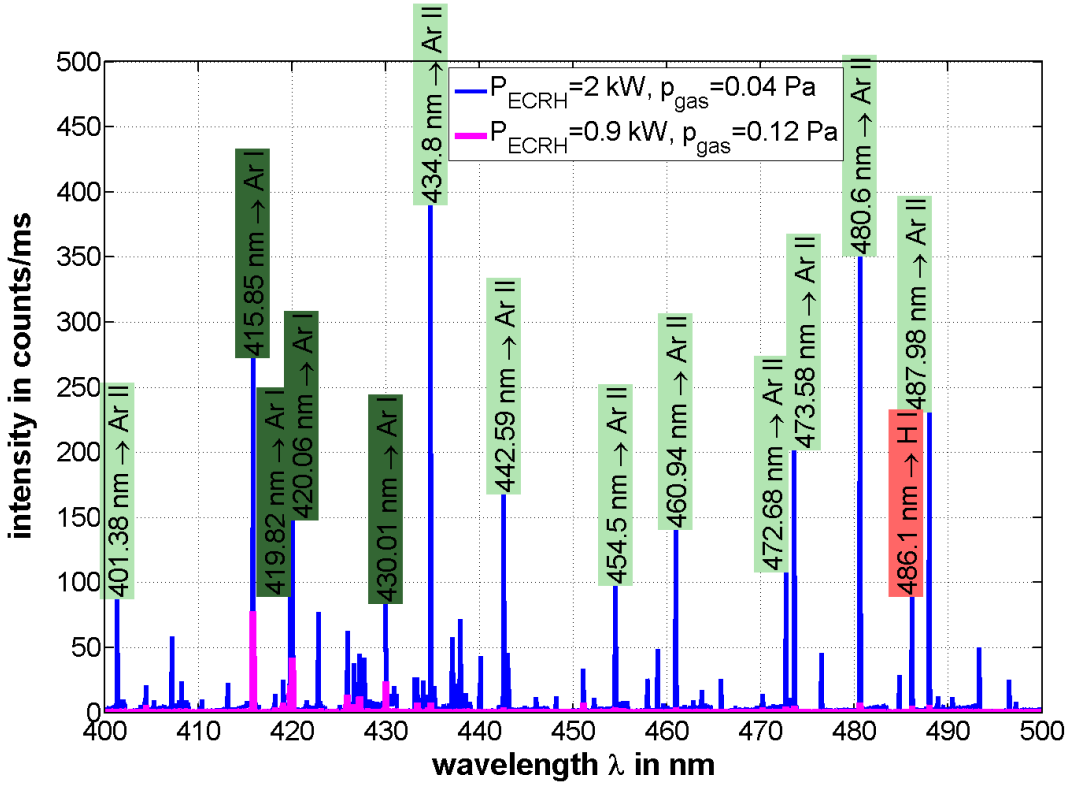

Figure 39 – Argon emission spectra in the main chamber of VINETA.II between 400 and 500 nm. Low ECRH power (magenta) and moderate gas pressure (corresponding to Figure 38a) and moderate power and low pressure (blue, Figure 38b). Intense observed emission lines are generated by argon neutrals (dark green background), argon ions (light green) and hydrogen (red). The spectrum was measured with an echelle grating spectrometer.

and 488 nm. In the argon plasma emission spectrum (Figure 39), a hydrogen line at 486 nm can be observed, too. This is the result of hydrogen out-gassing from the inner device walls. The radiation intensity of this hydrogen line, which is the H-β-line from the Balmer series, is usually higher after VINETA.II was opened (e.g. for repairs or diagnostic rearrangements). During an opening, the main chamber is flooded with surrounding atmosphere and water molecules present in the air some of which might be contained by the inner chamber walls.

In spectral investigations of helium discharges in VINETA.II, no He II emission lines could be observed in the operation range of these experiments. For neon, only one weak Ne II emission line could be excited in high power discharges, at $\lambda = 332.37$ nm. Overview emission spectra of helium and neon discharges in VINETA can be found in the Appendix A.5.
Due to the lack of intense He II and Ne II emission lines, no Doppler CIS measurements were performed for these elements. Ions are present in VINETA's helium and neon discharges. However, there are no (intense) ion emission lines because the excitation energies for the emission lines in the visible spectrum are too high for helium and neon (in contrast to argon). A list of the first and second ionisation energies as well as the required and measured excitation energies for all three noble gases can be found in Table 3.

	1st ionisation energy	**2nd ionisation energy**	**excitation energy in 1st ionisation stage**	**range of observed excitation energies**
helium	24.59 eV	54.42 eV	> 50 eV	22-24 eV (He I)
neon	21.56 eV	40.96 eV	> 30 eV	31.5 eV (Ne II) 18-21 eV (Ne I)
argon	15.76 eV	27.63 eV	> 19 eV	19-21 eV (Ar II) 14-16 eV (Ar I)

Table 3 – Ionisation and excitation energy data for observed discharge emission lines in VINETA.II. For the excitation energies, the energy level of the upper population state of the transition is meant. Each energy is in relation to the ground state of its ionisation state. The data was extracted from [63] and [64].

The observed emission lines in VINETA's helium, neon and argon discharges demonstrate that VINETA's electron temperature can be high enough to excite atomic states in the range between 14 and 24 eV by faster electrons in the tail of the distribution function. In these instances, the electron temperature ranged between 5 and 8 eV, sufficient to ionize all three elements.

6.3 Ion Dynamics in VINETA.II

To explore basic ion dynamics in VINETA.II, the simple case of no magnetic reconnection drive was investigated with the Doppler CIS. To observe any ion dynamics dependent on the magnetic field, the ions need to be magnetized in the linear plasma column of VINETA.II. This

is not always the case in small, low-temperature plasma experiments.
Ions as well as electrons are magnetized, or confined to the magnetic field lines, if their motion is dominated by gyrations around the magnetic field lines instead of e.g. random walk induced by collisions. Only then, they are influenced by magnetic drift effects induced e.g. by magnetic curvature, $\vec{E} \times \vec{B}$ or diamagnetic drifts. Electrons are usually confined to the magnetic field lines due to their small mass.

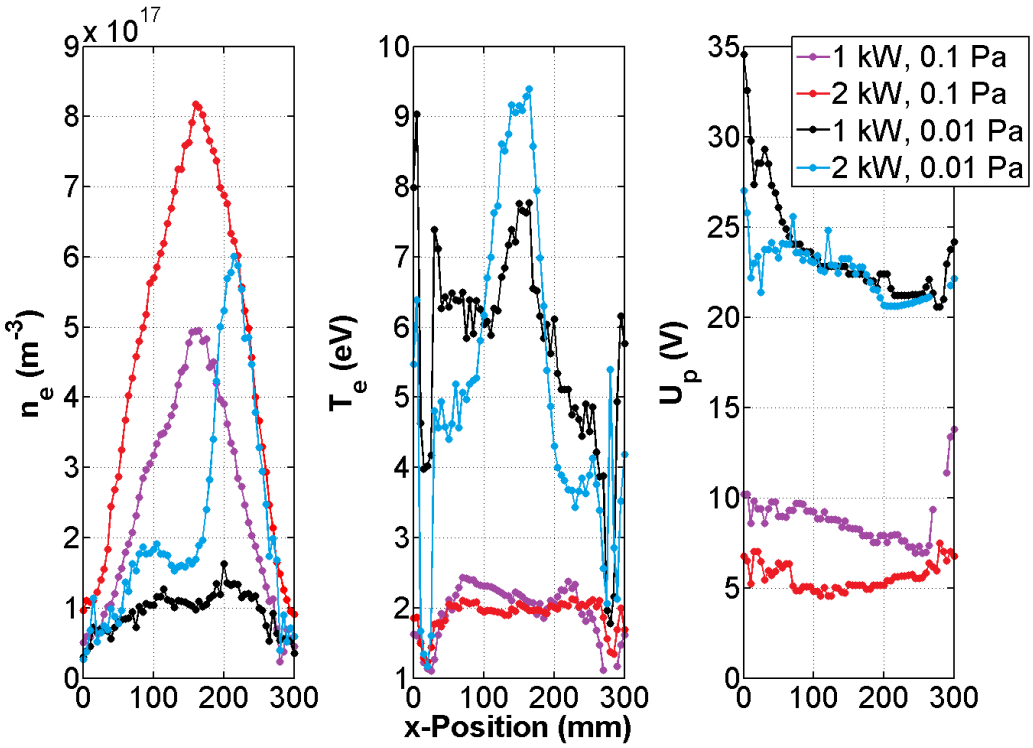

Figure 40 – Radial profiles of electron density n_e, temperature T_e and plasma potential U_p measured with a moveable langmuir probe in the main chamber of VINETA.II. The centre of VINETA's plasma column is at $x \approx 150\,\text{mm}$. The magnetic guide field strength is 15 mT.

To determine whether there is a radial electric field and if the ions are magnetized, some basic plasma parameters were measured in VINETA.II with a Langmuir probe. In Figure 40, recorded values for plasma potential U_p, electron density n_e and temperature T_e are shown for different operation parameters. The data was measured in the centre of the main chamber of VINETA.II, along the x-axis displayed in Figure 36. In general, the probe measurements reveal that the lower the initial gas pressure, p_{gas}, the higher the electron temperature T_e in VINETA.II. There is a gradient in the plasma potential, U_p, for these high-temperature cases. However, the measured plasma potential is not peaked, as is expected for a linear plasma column axially ending on conducting walls (cf. chapter 2.2). It is not clear why the measured Langmuir probe potentials are not peaked. Peaked plasma potentials have been measured in VINETA.I ([65], p.44), where plasma parameters are similar to VINETA.II.
For high neutral gas pressures ($\approx 0.1\,\text{Pa}$), the electron temperature remains low ($T_e \approx 2\,\text{eV}$). Further Langmuir probe measurements, which are not shown here, were conducted for different

magnetic guide fields.

Due to the availability of spectral argon ion lines (Ar II), the usual VINETA.II operation settings were an initial neutral argon gas pressure, p_{gas}, between 0.01 Pa and 0.04 Pa, a magnetic guide field of $B_z = 15\,\mathrm{mT}$ and a total ECRH power between 2 kW and 3.5 kW for the Doppler CIS measurements. The corresponding case in Figure 40 is that of high ECRH power and low initial gas density (2 kW, 0.01 Pa). For these settings, the highest electron temperature of $T_e \approx 9\,\mathrm{eV}$ was recorded. This is in agreement with spectral observations presented in the previous subsection. The electron density is peaked and is on the order of $n_e \approx 6 \cdot 10^{17}\,\mathrm{m}^{-3}$ at maximum. It is not clear why the electron density profile is asymmetric in Figure 40, whereas the others are not. Since ECRH is used and the electron-ion collision is low, the ion temperature, T_i, is expected to be at room temperature (293 K or 0.025 eV) in VINETA.II. It is assumed that $n_i \approx n_e$. In Table 4, there is an overview of derived plasma quantities for these observed parameters.

parameter	**value**
debye length $\lambda_{D,i}$	$1.6\,\mu$m
ion gyro frequency $\nu_{i,g}$	5.8 kHz
ion-neutral collision frequency $\nu_{i,n}$	0.9 kHz

Table 4 – Derived ion parameters during Doppler CIS measurements with an initial neutral gas pressure of $p_{\mathrm{gas}} = 0.01\,\mathrm{Pa}$ and absorbed ECRH power of $P_{\mathrm{ECRH,\,abs.}} = 2\,\mathrm{kW}$ in VINETA.II. The neutral gas pressure translates into an initial neutral density of $n_g = 2.5 \cdot 10^{18}\,\mathrm{m}^{-3}$. For the ion-neutral collision frequency $\nu_{i,n} = \bar{v}_i/(n_g \sigma_i)$, a combined elastic scattering and charge transfer cross-section of $\sigma_i \approx 10^{-18}\,\mathrm{m}^2$ was taken.

The ions in VINETA.II are expected to be magnetized for the operation settings during Doppler CIS measurements, since the ion-neutral collision frequency is about five times smaller than the ion gyro frequency.
In the following subsection, an estimation of the expected ion flows is made for the plasma parameters during the Doppler CIS measurements ($P_{\mathrm{ECRH,\,abs.}} = 2\,\mathrm{kW}$, $p_{\mathrm{gas}} = 0.01\,\mathrm{Pa}$). The estimated flows will be compared with the Doppler CIS flow measurements.

6.3.1 Expected ion flows in VINETA.II

A radial electric field is generated due to the presence of a varying plasma potential in the plasma column. Charge separation occurs close to the (conducting) end plates of the vessel, due to the larger mobility of the electrons. According to the Boltzmann relation, the plasma potential U_p is dependent on the electron temperature as well as the density, to a lesser extent: $U_p \propto T_e \cdot \ln(n)$. A more detailed explanation of this process is provided in chapter 2. In the case of conducting end walls (as in VINETA.II), the plasma potential should be peaked similarly to the electron temperature profile and the resulting radial electric field is directed outward.

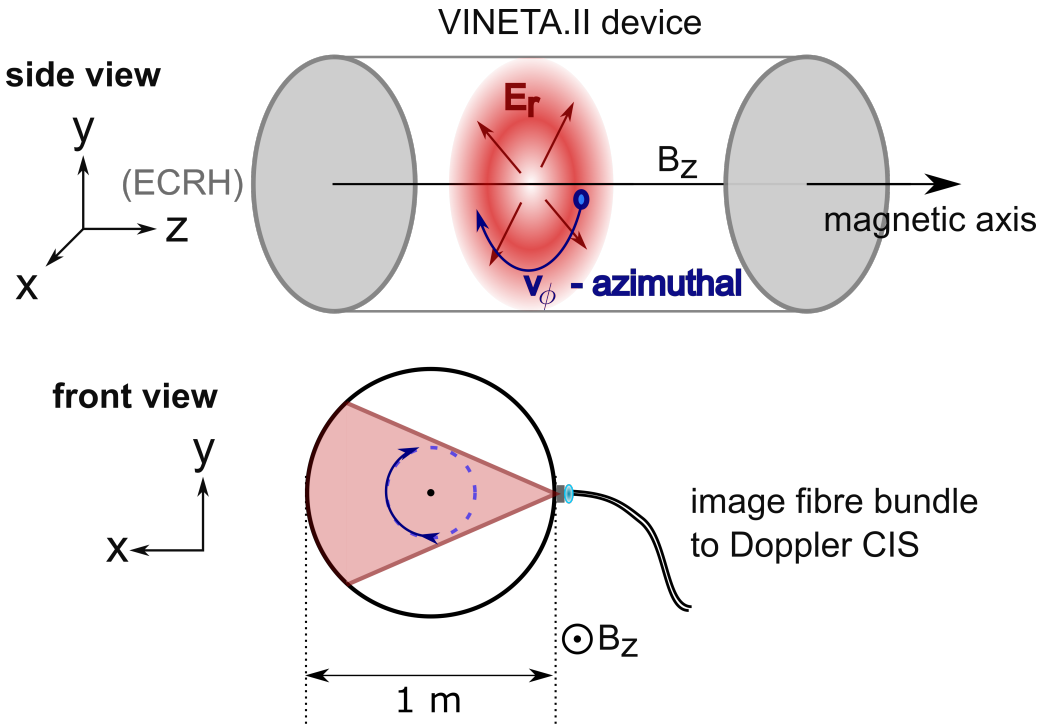

Figure 41 – Schematic side and front view on VINETA.II. The red area in the lower schematic marks the Doppler CIS viewlines (as in Figure 36). An azimuthal ion drift is expected due to a radial electric field $\vec{E_r}$ and the linear magnetic guide field $\vec{B_z}$.

Figure 41 shows an overview of the directions of $\vec{E_r}$ and $\vec{B_z}$ in VINETA.II. The cross-product of B_z and E_r leads to an azimuthal ion drift, $\vec{v_\phi}$, around the magnetic axis according to:

$$\vec{v_\phi} = \frac{\vec{E_r} \times \vec{B_z}}{B_z^2} \tag{44}$$

$$v_\phi = \frac{E_r}{B_z} \tag{45}$$

To estimate the speed of the azimuthal ion drift, the radial electric field is determined from the measured plasma potential in VINETA.II (by the langmuir probe, cf. Figure 40) according to:

$$E_r = -\frac{dU_p}{dr}. \tag{46}$$

The measured plasma potential has a gradient over r. Over a length of $r = 0.2\,\mathrm{m}$, it varies by about $\Delta U_p = -3\,\mathrm{V}$. The corresponding radial electric field is $E_r = 15\,\mathrm{Vm}^{-1}$. Inserted into Equ. 45, and for a magnetic guide field of $B_z = 15\,\mathrm{mT}$ in the main chamber, the estimated ion flow speed due to $\vec{E} \times \vec{B}$ is $v_{\mathrm{ion}} = 1000\,\mathrm{m/s}$.

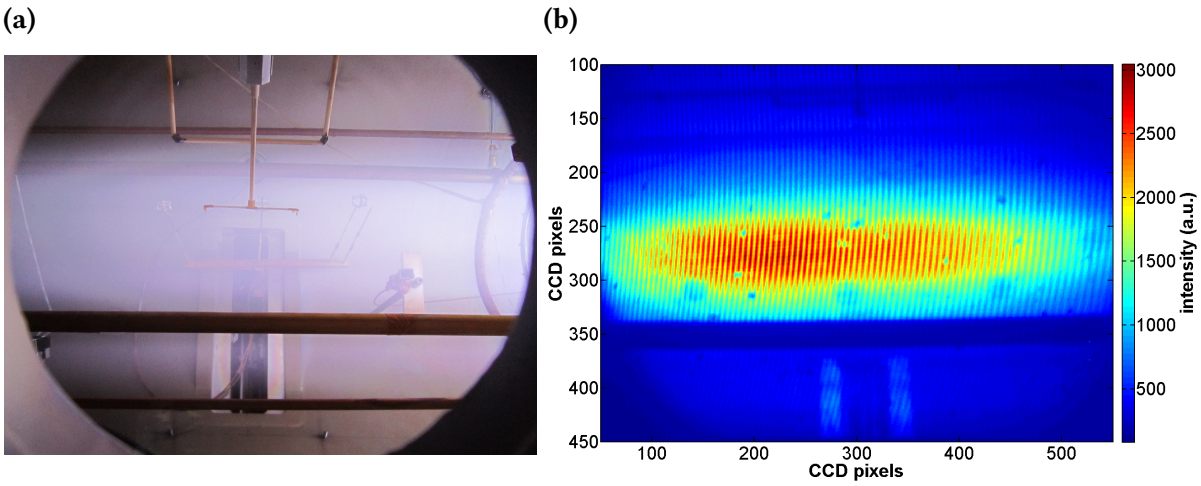

Figure 42 – Radial view into the VINETA.II main chamber during an argon discharge (schematically indicated in Figure 36). (a) View into the VINETA.II main chamber. (b) Doppler CIS camera image through the image fibre bundle of the same view. It is mirror-inverted due to the use of the mirror in the set-up of the Doppler CIS.

6.3.2 Doppler CIS ion flow measurement in VINETA.II

All presented measurements in this chapter were made for the Ar II line at 487.986 nm. For this line, an argon ion laser with the same wavelength was used as calibration source. A 2 nm narrow-bandpass filter at 488 nm was applied to suppress all other light from the plasma. The used Doppler CIS set-up is similar to the set-up described in chapter 4.1. An image fibre bundle was used to observe a radial view onto the guide field in the main chamber of VINETA.II. However, as this was prior to the development of the moveable mirror, a half-reflective mirror was used.
To be sensitive to ion flows on the order 100 m/s, a large set of delay plates were used in the VINETA.II Doppler CIS set-up. A 5.4 mm α-BBO displacer, three 10 mm α-BBO delay and two 20 mm LN delay plates were inserted into the Doppler CIS. With all these plates, a phase shift of $\Delta\Phi = 5\,^\circ$ corresponds to a wavelength shift of $\Delta\lambda = 0.3\,\mathrm{pm}$ (cf. Figure 21 in chapter 3.2.2) or a flow speed of $v_{\mathrm{ion}} = 215\,\mathrm{m/s}$ for the 488 nm Ar II line.

In Figure 42, the viewing area of the Doppler CIS into the main chamber of VINETA.II is shown. With the applied lenses, about 40 cm of the central column of the VINETA.II plasma could be observed. With the radial view, ion flows moving in the plane perpendicular to the magnetic guide field axis can be measured. Only moderate to high ECRH powers $P_{\mathrm{ECRH,\,abs.}} > 2\,\mathrm{kW}$ and low initial neutral gas pressures ($p_{\mathrm{gas}} < 0.04\,\mathrm{Pa}$) were set for Doppler CIS measurements in order to excite the Ar II line, as discussed previously.
In Figure 43, a flow measurement of the azimuthal ion rotation in VINETA.II is presented. Positive flows mark red-shifted light and negative flows blue-shifted light. The image fibre guide end on VINETA.II was rotated differently for many of these measurements, to check that the ion flow pattern would rotate accordingly and rule out symmetric effects in the diagnostic.

In Figure 43, the image bundle was rotated by roughly 30 °. A different second lens was used than in the Doppler CIS picture in Figure 42, which is why the plasma column appeared larger. In Figure 43, the argon ions flow towards the observer view in the upper part of the image and away in the lower part. This is consistent with the $\vec{E} \times \vec{B}$-drift that causes an azimuthal flow rotation as described previously. The flow direction is caused by a radially outward pointing electric field, indicating that the plasma potential must have been peaked (as is expected by for conducting walls). The flow speed is zero in the vicinity of the magnetic axis. The measured flow speeds ranged up to ± 2000 m/s in the shown example, the highest recorded in VINETA.II in the course of this work. Additional Doppler CIS flow measurements (cf. Figure 44) show speeds ranging from ± 1500 m/s to only a few hundred meters per second. Furthermore, in some measurements, no azimuthal ion rotation could be observed at all despite sufficient Ar II line radiation.

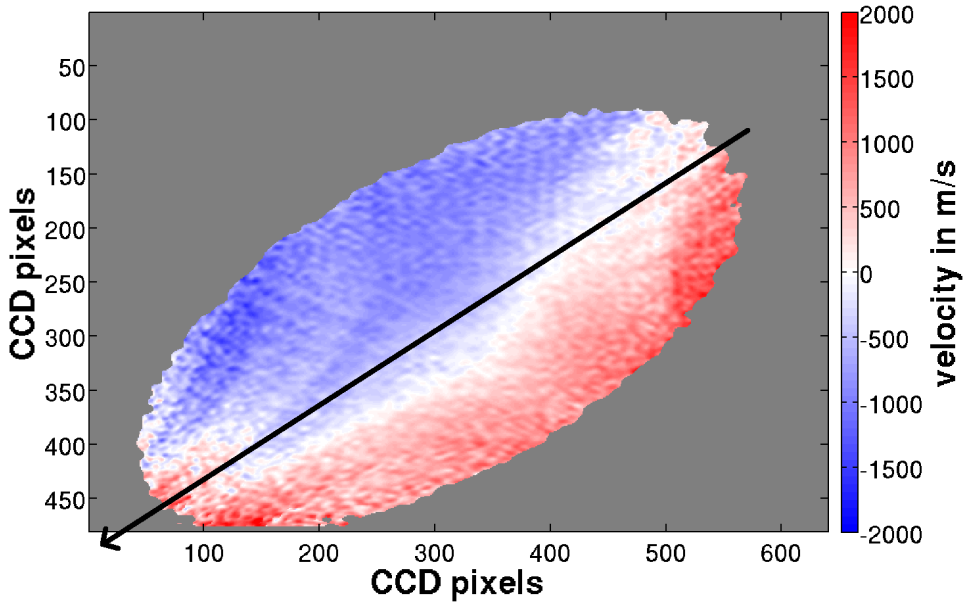

Figure 43 – Argon ion flow in the main chamber of VINETA.II, measured with the Doppler CIS for $P_{\mathrm{ECRH,\,abs.}} = 3$ kW and initial gas pressure $p_{\mathrm{gas}} = 0.012$ Pa. Image areas, where Ar II line emission was below 20% of the maximum value were greyed out. The plasma column is tilted to nearly 30 °. The magnetic axis is indicated by a black line for orientation. The exposure time of the camera was 300 ms.

Since the Doppler CIS measurements are restricted to a small operational window of ECRH power and neutral gas pressure settings, the large variation and occasional total absence of ion rotation speeds was unexpected. The strong variations were observed for comparable initial operation settings in the months during which the VINETA.II measurements were conducted[26]. In some discharges, the measured ion flow speed stayed nearly constant, whereas during other measurements, it globally decreased during the discharge. This is demonstrated in Figure 44. At the beginning of the discharge, an ion rotation could be observed. However later, the ion

[26]The Doppler CIS measurements in VINETA.II were conducted between June 2015 and November 2015.

rotation vanished, although the Ar II line intensity was about the same for both measurement images.

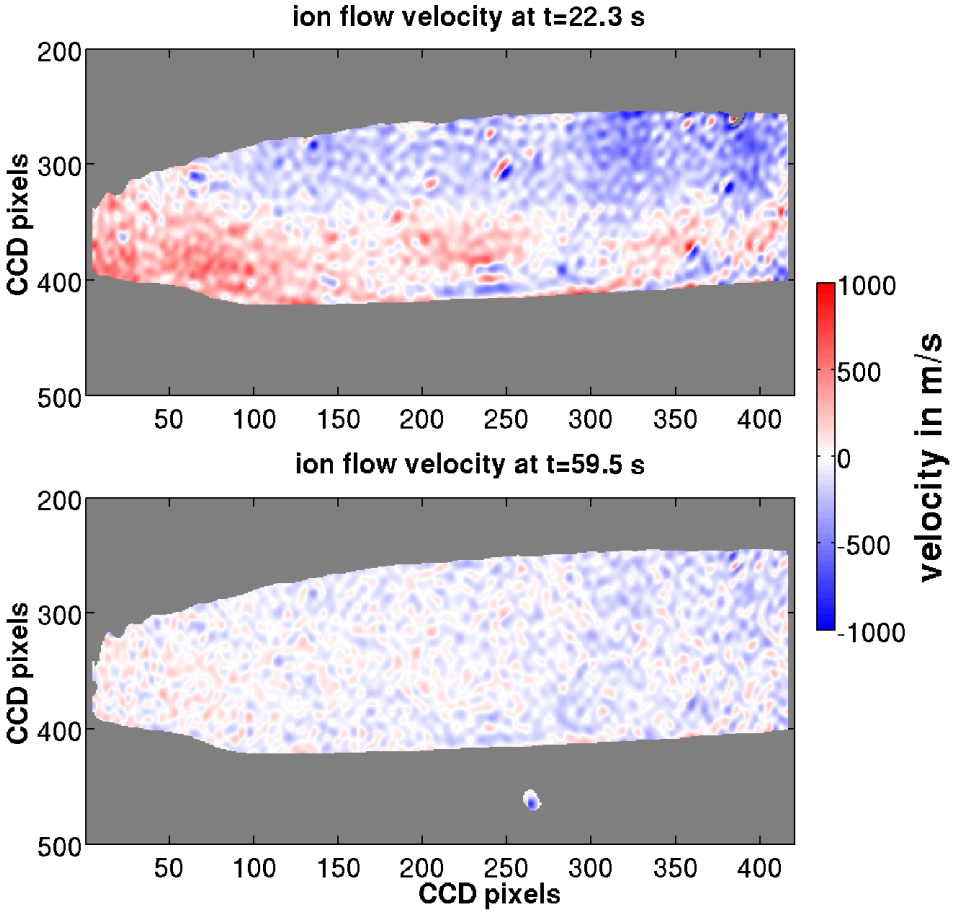

Figure 44 – Argon ion flow in the main chamber of VINETA.II, measured with the Doppler CIS for $P_{\mathrm{ECRH,\,abs.}} = 3.3\,\mathrm{kW}$ and $p_{\mathrm{gas}} = 0.012\,\mathrm{Pa}$. Although being taken during the same discharge and external settings, the ion flow varied at different times during the discharge. Image areas, where Ar II line emission was below 20% of the maximum value are greyed out. Positive flows indicate flow away from observer.

To investigate the cause of this variation, the emission spectrum was recorded during these discharges. In Figure 45, the temporal evolution of the spectral intensity of four different argon lines (including the observed Doppler CIS line at 487.986 nm) and two neutral hydrogen lines from the Balmer series, H-α at 656 nm and H-β at 468 nm, are shown. At the beginning of the discharge, there is a stabilization period of the ECRH system lasting about 20 s. During this time, the reflected ECRH power is automatically regulated and minimized, here until $t \approx 39\,\mathrm{s}$. Until $t = 90\,\mathrm{s}$, the spectral line intensities of the Ar II lines and the H-I lines vary considerably. The hydrogen lines increase and the Ar II lines decrease, whereas the neutral argon line intensity remains constant. This indicates a stable argon density, but a decreasing electron temperature due to a rising hydrogen density. The source of the hydrogen neutrals is out-gassing from the device walls, that heat up during the discharge. Openings happened several times during the

Doppler CIS measurement period in VINETA.II. Due to decreasing temperature, the electric field generated by the electron temperature gradient drops as well, diminishing the argon ion flow in the process.

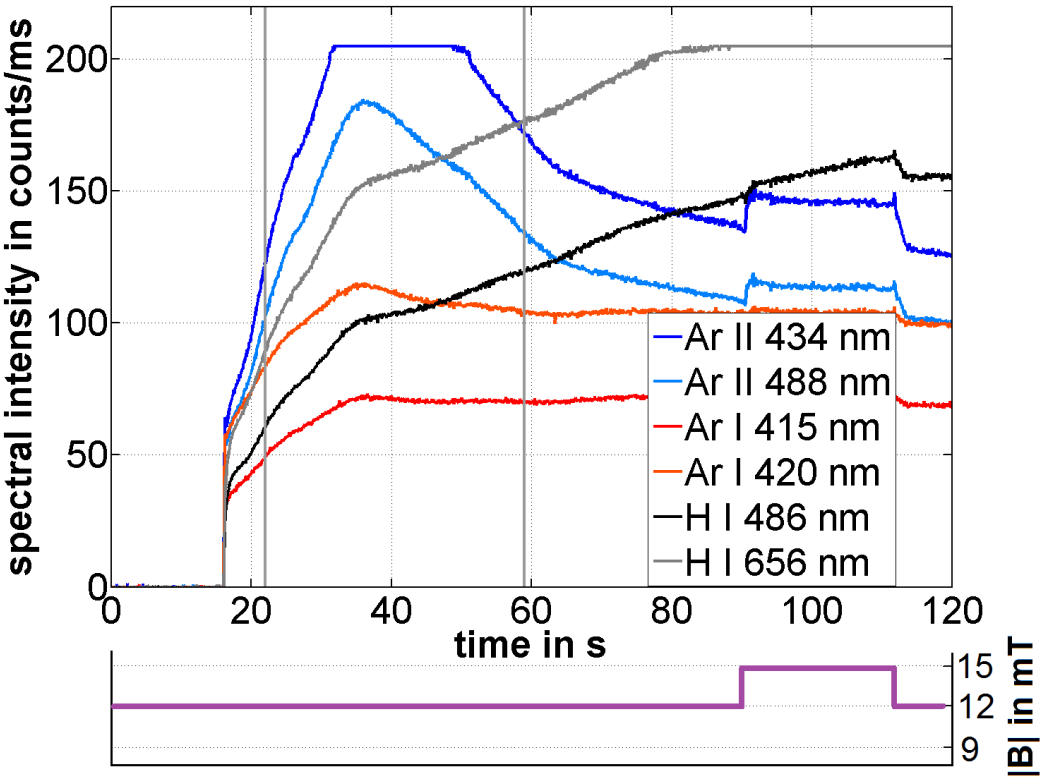

Figure 45 – Temporal evolution of the spectral intensity of six different lines emitted by the VINETA.II plasma. The VINETA.II discharge was powered by continuous ECRH operation. The plasma was started at $t = 17$ s. The magnetic guide field was varied during the discharge. The grey vertical lines mark the time points where the two Doppler CIS measurements in Figure 44 were made.

6.4 Summary of VINETA.II results

First Doppler CIS measurements have been conducted to investigate the ion dynamics in VINETA.II and to assess conditions for the possibility of a Doppler CIS measurement during a driven magnetic reconnection event. In this linear, low-temperature plasma experiment, spectral ion flow measurements can only be made for a limited range of operation parameters. This is due to the visibility of the Ar II ion lines, that appear only for high deposited ECRH power (> 2 kW) and low initial neutral gas densities (< 0.04 Pa).

The first Doppler CIS ion flow measurements in VINETA.II demonstrated an azimuthal flow pattern around the magnetic guide field axis, with flow speeds of up to 2000 m/s. The ion motion is generated by a poloidal $\vec{E}_r \times \vec{B}_z$-drift rotation. The observed flows indicate a radially outward electric field, which is expected in VINETA.II. Furthermore, the measured flow pattern and speed is in good agreement with a recent Doppler CIS ion flow measurement reported in a

similar linear experiment, MAGPIE ([21]). Although the flow results are structurally not in agreement with the measured plasma potential profile of a Langmuir probe, the Doppler CIS measurements are more consistent with the expected potential.
The azimuthal ion flow in VINETA.II was observed to vary, even if no external operation settings were changed. This is most probably due to an influx of hydrogen (cf. Figure 45) by outgassing from the inner device walls. Spectral measurements indicate that due to the increasing hydrogen density, the electron temperature drops considerably during these discharges. The azimuthal ion flow decreased and vanished in these circumstances. It is concluded that the overall electron temperature decrease leads to a decrease of the plasma potential gradient and thus radial electric field.
In the next subsection, an outlook is given on the requirements for a Doppler CIS measurement during a magnetic reconnection event in VINETA.II. Such a measurement could not be conducted within the time frame of this work, but some considerations were made for a future set-up.

6.5 Outlook: Flow measurements during a magnetic reconnection event

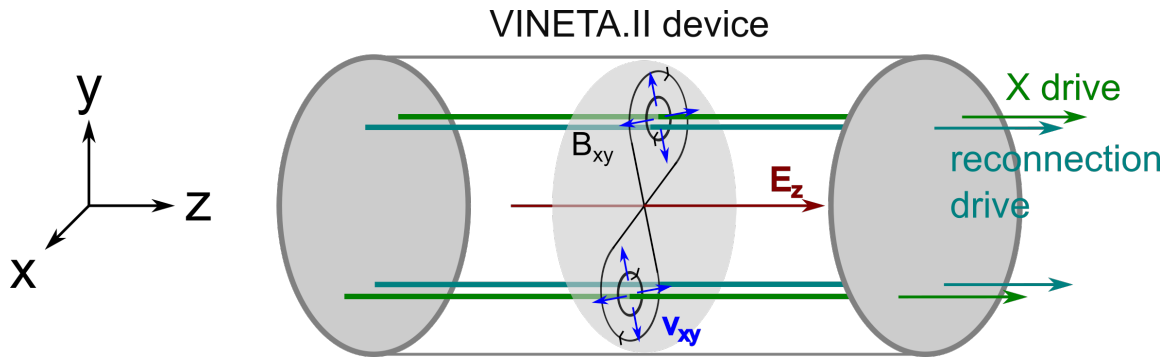

Figure 46 – Schematic side view on VINETA.II including the reconnection and X wires (in turquoise and green, respectively). A stationary current driven through the X wires generates a magnetic field (black) with an X-point topology in x and y direction. In the reconnection wires, a time-varying sinusoidal current varies the magnetic field and induces an electric field $\vec{E_z}$ (dark red). An ion drift (blue) is generated in the x,y-plane.

VINETA.II is a small plasma experiment dedicated to the study of driven magnetic reconnection [59]. Figure 46 shows a schematic overview of the VINETA.II experiment including its reconnection and X-drives. They generate a time-varying magnetic field with an X-Point topology in the plasma column. The X-drive carries a stationary current, whereas the reconnection drive is supplied with a sinusoidal current with a frequency of 6 kHz. This corresponds to a reconnection cycle duration of 167 μs.
Due to the sinusoidal time-variation of the magnetic field, an axial electric field is induced by

the reconnection drive:

$$\begin{aligned} E_z &= -\frac{\partial A_z}{\partial t} \\ \vec{B} &= \vec{\nabla} \times \vec{A} \end{aligned} \tag{47}$$

The orientation of the induced electric field E_z varies over the sinusoidal cycle. In the presence of the induced electric field and the X-point topology, an additional ion drift, v_{xy}, is generated in the x,y-plane:

$$v_{xy} = \frac{\vec{E_z} \times \vec{B_{xy}}}{B_{xy}^2} \tag{48}$$

In Figure 47, v_{xy} was integrated over eight sightlines of a simulated Doppler CIS diagnostic in the radial view position (as used for the measurements presented in subsection 6.3.2). The simulation demonstrates that counter-flows along the line-of-sights don't cancel out. The mean ion flow velocities are on the order of several thousand metres per second, which is in the same order of magnitude as the measured flows without magnetic reconnection drive. The overall flow structure should appear like a flow rotation to the Doppler CIS, similar as in Figure 43, but with increasing flow magnitudes in the centre of the image. In the vicinity of the X-point, however, the $\vec{E_z} \times \vec{B_{xy}}$ ion flow is expected to be much weaker since B_{xy} diminishes.
There are additional ion flows and local ion temperature increases expected by in-plane electrostatic fields during magnetic reconnection ([61]), which should be included in the simulation. However, it is already sufficient to see that some flows could be observed.

Since one magnetic reconnection cycle takes about 160 μs in VINETA.II, the Doppler CIS camera exposure time needs to be adjusted to such a fast timescale. The measurement time is limited at most a half reconnection cycle of 80 μs, since the flows are counter-directed during the second half.
A shutter with a high frequency needs to be applied to expose the camera (running with a long exposure time) in the same phase of repeated reconnection events. Empirical values of transmitted Ar II intensity into the Doppler CIS were roughly 500 counts in 500 ms exposure time (for the set-up including the image fibre bundle). To reach the same number of counts (or signal-to-noise ratio) with the same Doppler CIS set-up for one magnetic reconnection measurement, an image exposure for over 6000 magnetic reconnection cycles is required. Since each cycle includes a charge process of about 1 s (to recharge the reconnection drive capacitor), an overall Doppler CIS exposure time of 104 minutes is necessary for one measurement image.

To measure the ion dynamics with the Doppler CIS over such a long measurement time would be very difficult. A heat cell would be required for Doppler CIS birefringent crystals to keep the plate temperature constant. Furthermore, it is suggested to monitor the plate temperature over the course of a such a measurement.

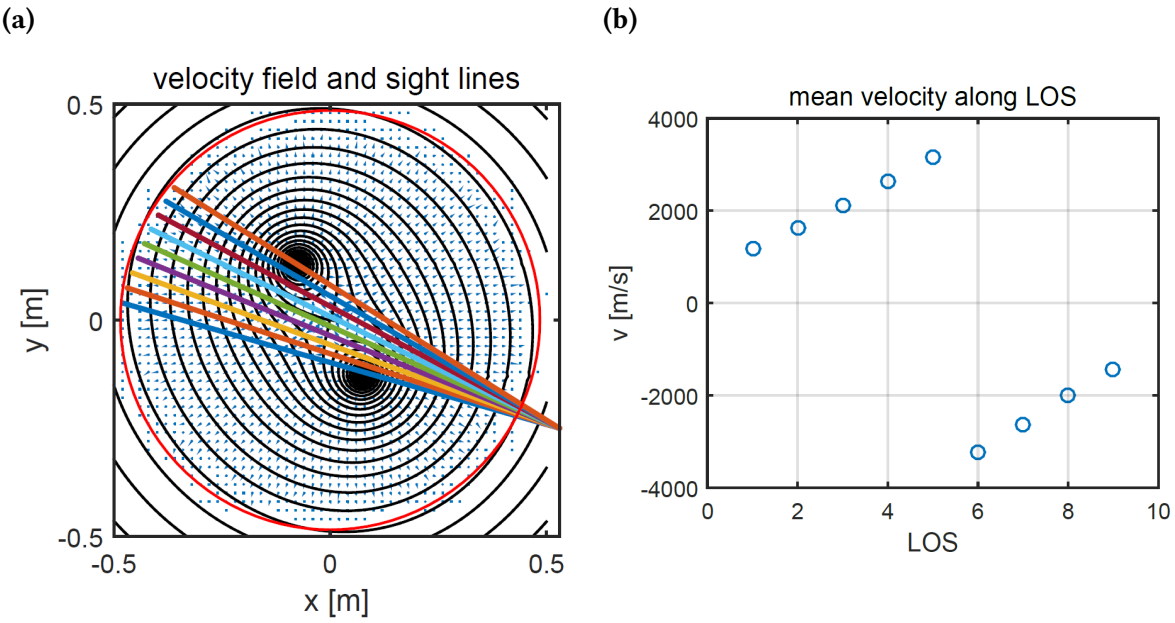

Figure 47 – (a) Poincaré plot of the X-point topology (black) in VINETA.II during magnetic reconnection experiments. The sightlines of the Doppler CIS in the radial view position (cf. Figure 36) into the main chamber of VINETA.II are marked in different colors. The wall of the main chamber is marked in red. (b) Line-of-sight-integrated particle velocities along the eight sightlines displayed in (a). Figures provided by Adrian von Stechow.

Overall, to measure the ion drift caused by the $\vec{E_z} \times \vec{B_{xy}}$-drift and possible additional magnetic reconnection drifts with the Doppler CIS, the following conditions need to be met in VINETA.II:

- A high ECRH heating power ($> 2\,\mathrm{kW}$) and a low initial neutral gas pressure ($< 0.04\,\mathrm{Pa}$) need to be set for the Ar II ion lines to be present.
- The ions have to be magnetized.
- Time-varying effects such as hydrogen out-gassing need to be negligible or constant throughout the magnetic reconnection measurement in order to keep the internal plasma conditions in VINETA.II constant. Thus, the hydrogen needs to be reduced to allow sufficient density control, e.g. by baking the vessel.
- A new camera and fast shutter needs to be added to the current Doppler CIS set-up.
- A heat cell needs to be included in the Doppler CIS set-up to keep the measured phase difference $\Delta\Phi$ independent of the plate temperature.
- A trigger loop to couple the shutter and the magnetic reconnection drive.

Although the technical requirements of a Doppler CIS flow measurement during a driven magnetic reconnection event VINETA.II is very challenging, there is no fundamental reason why such a measurement shouldn't work out. Fast synchronous imaging of high-frequency plasma fluctuations has been proven to work on H-1NF before ([66]).

7 Results III: ASDEX Upgrade flows

Impurity ion and neutral deuterium flows were measured with the Doppler CIS in the divertor of the tokamak experiment ASDEX Upgrade (AUG). Flow velocities in the divertor and scrape-off-layer (SOL) are of particular interest for the understanding of the plasma exhaust and edge impurity transport of high-temperature plasma experiments. These are critical areas of study for future plasma experiments and fusion reactors such as ITER and DEMO, since exhaust heat fluxes on the target plates are expected to high and impurity transport from the SOL into the core can have important implications for the general plasma performance. By investigating ion dynamics of impurities (and the main plasma species), general understanding of the SOL physics can be improved and codes such as SOLPS or EMC3-Eirene could be validated.

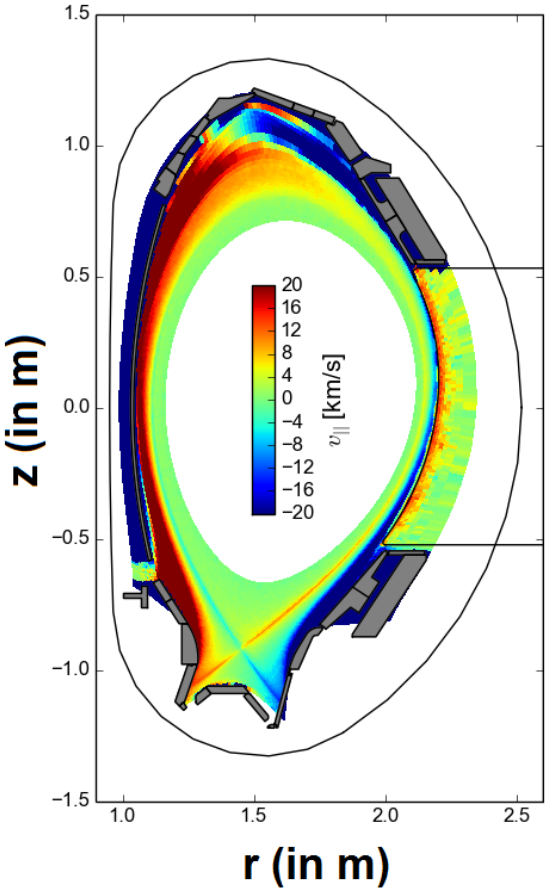

Figure 48 – Simulated parallel main ion flow for AUG by the EMC3-Eirene code.

Plasma dynamics are far more complex in divertor topologies than in linear, low-temperature plasma experiments such as VINETA.II. The Bohm sheath criterion determines the ion flow only very close to the divertor plates and ion flows with high Mach numbers are observed far away from the plates in the SOL ([13],[20]). There are different mechanisms that drive bulk plasma and impurity ion flows in the SOL and divertor of tokamaks, making good diagnosis

critically important to identify e.g. the dominant physics. An overview of these mechanisms is provided in chapter 2.
Several computational codes are used for the prediction of ion flows and other plasma parameters in the edge and SOL, e.g. UEDGE ([67],[36]), SOLPS ([68]) or EMC3-Eirene ([69],[70]). These codes solve the Braginskii fluid equations that describe the parallel heat transport for plasma electrons, ions and impurities, but also rely on kinetic approaches for the various neutral particle collision processes and for radiation transfer. EMC3-Eirene can simulate the plasma edge and SOL for three-dimensional topologies, applicable for stellarators or tokamaks operating with resonant magnetic perturbations (RMPs), however radial drifts due to e.g. electric fields are not included in it at the time of writing. Radial drifts are necessary to explain some phenomena, e.g. power asymmetries between the HFS and LFS divertor target plates ([43]). In contrast, UEDGE and SOLPS solve the plasma equations only for 2D-axisymmetric geometries but include drifts and therefore are able to simulate not only parallel plasma properties, but also e.g. perpendicular bulk flows. An example of a simulated parallel main ion flow in the edge of AUG is shown in Figure 48. Due to the opposite magnetic field pitch angle, opposite flows are expected in the high- and low-field side of the divertor and SOL. In the presented EMC3-EIRENE simulation, the SOL flow is directed towards the plates on both sides. Under certain conditions, a reversal of the flow directions is expected, e.g. when the toroidal magnetic field is reversed or for certain SOL parameters ([71],[72]). However, these conditions were not present during the AUG discharges investigated with the Doppler CIS.

The comprehensive measurement of ion flows is difficult in the complex divertor geometry for conventional flow diagnostics. For example, Mach probes measure in one local area of the SOL and a comprehensive overview requires many probes. Furthermore, they can't differentiate between the plasma and the various impurity ion species. The Doppler CIS is a powerful tool to help solve this issue, since it provides a large number of sightlines. It can measure the flow of any selected ion or neutral species where it emits light.
In the following subsections, the Doppler CIS flow measurements made in the divertor of AUG will be presented. Impurity ion species and neutral deuterium flows have been measured in the frame of this work. The measurement of main ion plasma flows is not possible in case of hydrogen or it's isotopes due to the non-existence of ion emission lines. After an overview of AUG and the diagnostic view into the torus, the radiation properties observed in the AUG divertor will be discussed in subsection 7.3. The flow measurements follow in 7.4 as well as a analysis of the flow components in parallel and perpendicular direction.

7.1 Overview of ASDEX Upgrade

ASDEX Upgrade (AUG) is a medium-sized tokamak operated by the Max-Planck-Institute for Plasma Physics in Garching. An overview of important device parameters is listed in

Table 5. Its predecessor was ASDEX (Axial-Symmetric Divertor EXperiment), the first plasma experiment to use a divertor and where the H-Mode was discovered in neutral beam heated divertor discharges [73]. AUG started plasma operation in 1991, adapted for conceptual studies for an experimental fusion reactor. It's main goals are research for the preparation of the ITER operation and the design of a prototype fusion reactor, DEMO. 16 field coils generate the toroidal magnetic field with a typical strength of $2.5\,\mathrm{T}$ in the plasma centre. The poloidal magnetic field, needed to confine the plasma, is generated by a plasma core current of up to $1.6\,\mathrm{MA}$ that is mainly induced by a central transformer coil. Additional coils are used for plasma stabilisation, positioning and shaping. The plasma pulse length of AUG is technically limited to about $10\,\mathrm{s}$, which is a multiple of the typical global confinement time $\tau \approx 100\,\mathrm{ms}$.

parameter	**value**
B-field on axis	$2.5\,\mathrm{T}$
major radius	1.65 m
minor radius	0.5 m
plasma volume	$14\,\mathrm{m}^3$
plasma current	0.8 MA
pulse length	$10\,\mathrm{s}$
total ECRH power (max.)	4 MW
total ICRH power (max.)	6 MW
total NBI power (max.)	20 MW

Table 5 – Operation parameters of ASDEX Upgrade.

Several external heating schemes are used in AUG: neutral beam injection (NBI), electron and ion cyclotron resonance heating (ECRH and ICRH) as well as ohmic heating from the plasma current. Core plasma temperatures can reach up to $25\,\mathrm{keV}$ and the plasma densities are in the range between 10^{19} and $10^{20}\,\mathrm{m}^{-3}$. The normal mode of plasma operation is the H-Mode. The main plasma species is usually deuterium, but sometimes hydrogen or helium are used. Deuterium plasmas are of higher interest for fusion and plasma research, since they allow the study of isotope effects on e.g. transport and erosion as well as to enhance the energy confinement in tokamaks. Tritium is not used in AUG for several reasons. The most important one is that the fusion α-particles would not significantly contribute to the overall heating power of AUG. Furthermore, neutrons from the D-T reaction would damage and activate machine components, thus impeding access to AUG. However, a small number of neutrons are generated in AUG with pure deuterium plasmas due to some D-D fusion reactions in the interaction zone of the plasma with the neutral beam injection.

The magnetic field topology usually is a divertor configuration, where the open field lines

of the SOL end on the divertor target plates. Three magnetic configurations with only the lower, the upper or both poloidal field divertors can be applied in AUG. The lower divertor is able to withstand higher heat fluxes, however it is not possible to operate it with reversed B-field (which is why no reversed field measurements were performed with the Doppler CIS, that was only in view of the lower divertor). Most Doppler CIS measurements on AUG were performed in the lower divertor configuration, since it is the most common divertor configuration. An overview of the AUG interior including the lower divertor is provided in Figure 49.

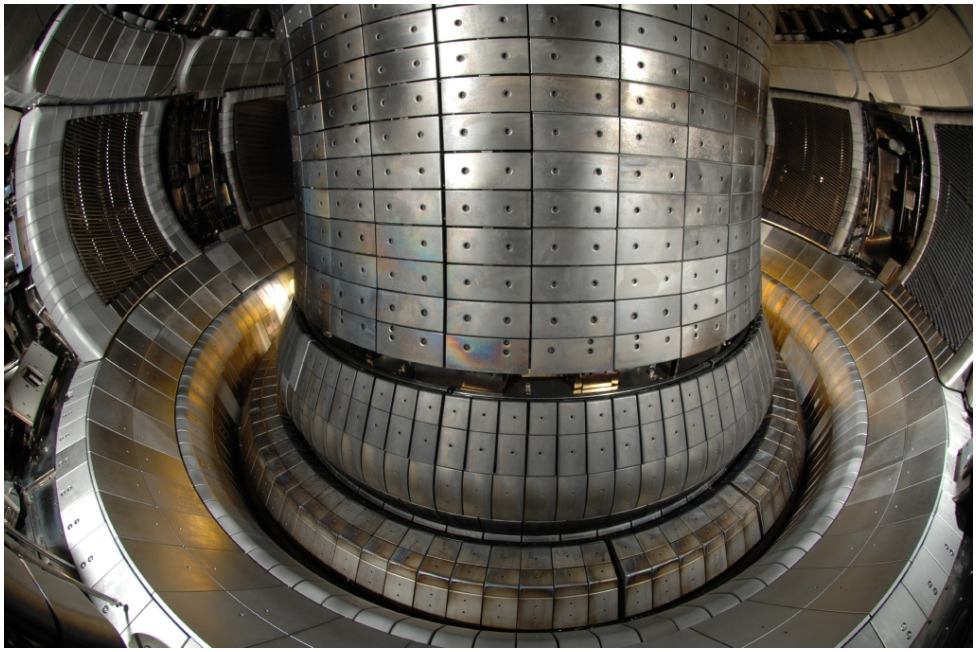

Figure 49 – View inside ASDEX Upgrade. The first wall surface is almost entirely tungsten-coated. Behind the inner wall in the centre, there is the transformer coil for inducing the plasma current. The outer wall includes several ports, ICRH antennae and other diagnostic parts. The divertor is in the lower part of the device.

In comparison to other tokamaks, AUG is characterized by a high heating power per volume, a first wall almost completely consisting of tungsten-coated surfaces (since 2013) and a magnetic field topology that is also foreseen for ITER.

7.2 Doppler CIS set-up on AUG and plasma view

For AUG Doppler CIS measurements, only one viewing location was used for all measurements presented in this work. It allowed a wide view into the device. As mentioned in chapter 4, an image fibre bundle was required to transmit light to the Doppler CIS CCD camera. This was due to space restrictions and the inaccessibility of the ports between the magnetic coils during the measurement campaign. By the use of an image fibre bundle some advantages and disadvantages arose, that are described in more detail in Appendix A.3.
Figure 50 shows a top view of AUG and the installed Doppler CIS system. One end of the image fibre bundle was attached to the Doppler CIS box and the other end was attached to an

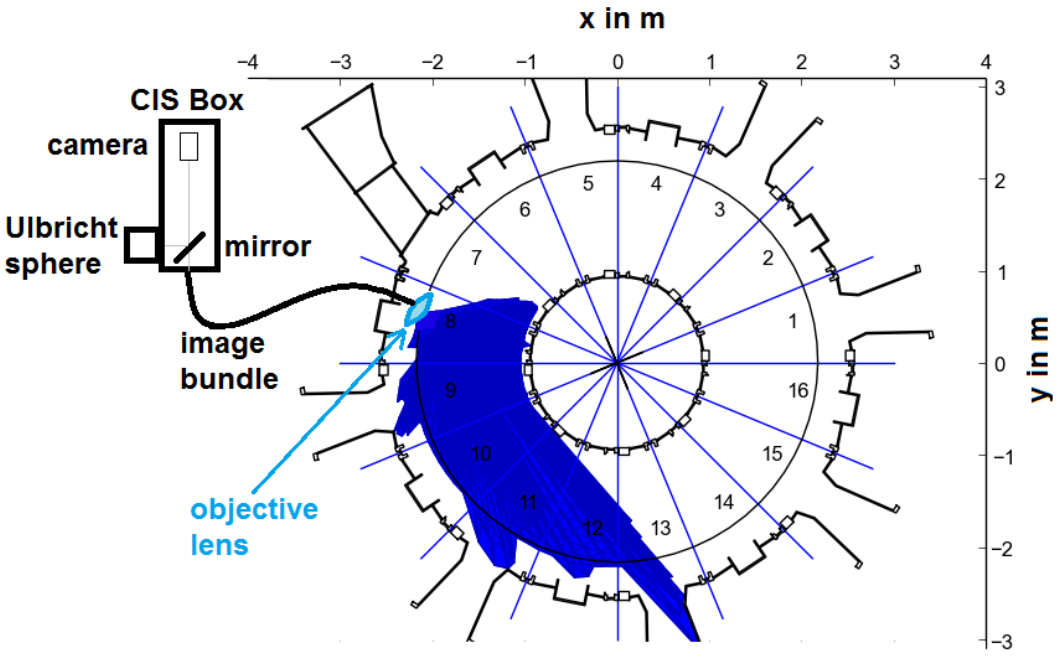

Figure 50 – Schematic of the Doppler CIS set-up and its toroidal view on AUG. Blue: coverage of first wall by Doppler CIS (all lines-of-sight).

$f = 8$ mm objective lens, which was placed inside a 2 m immersion tube that has a vacuum window at its end. The window is in the upper half of the vacuum chamber, close to the tiles of the upper divertor on the outboard side. The view from this window into the plasma chamber can be seen in Figure 51. The sightlines provide an overview of the lower divertor and first wall on the high-field side.

For comparisons with simulations and analysis of the observed line radiation pattern, the camera view was reconstructed. With a CAD model of AUG, selected pixels in the camera images were assigned to the known x, y, z-values of the components recognized in the image. A 2D cubic transform was then performed to calculate the direction vectors of the line-of-sight for each pixel in the camera image. In Figure 52, the sightlines in (R,Z)-projection to where they intersects a first wall element are shown.
The plasma image taken by the diagnostic camera could change by re-adjustment of the image fibre bundle on the diagnostic end. This was e.g. the case when the narrow-bandpass interference filter was changed and the focus settings of the second lens needed to be adjusted. Thus, e.g. the deuterium flow measurements required a new reconstruction of the sightlines.

Since the view of the image fibre bundle is obliquely down from the upper part of the device in the lower divertor, the sightlines have parallel as well as perpendicular components to the magnetic field. The magnetic field direction, that varies temporally over each discharge, is provided by CLISTE, an equilibrium reconstruction code ([74]). The viewing direction of the sightlines in relation to the magnetic field was analysed and the results of this analysis are

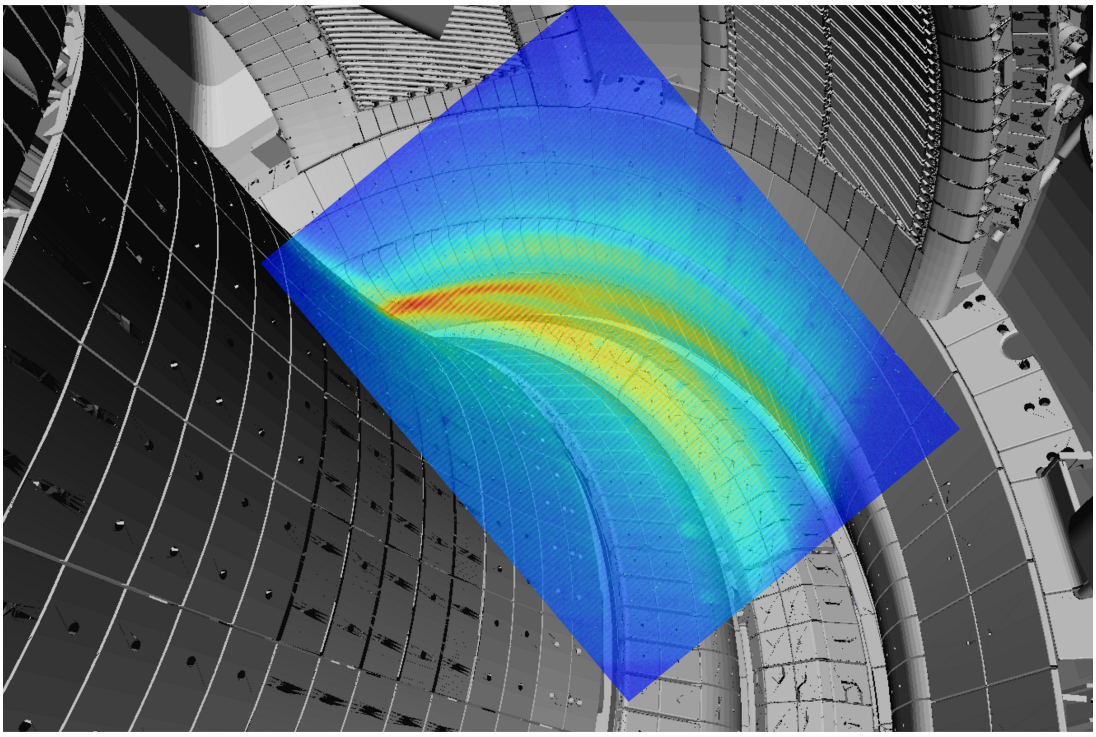

Figure 51 – CAD view of the Doppler CIS coverage inside the torus of AUG. A Doppler CIS measured CCD camera picture is transparently blended in for orientation.

presented in subsection 7.5.

7.3 Visible radiation in the divertor of AUG

In high-temperature plasma experiments such as ASDEX Upgrade, electromagnetic radiation is emitted in many forms, e.g. thermal radiation at the divertor tiles, electron cyclotron emission and X-rays from the hot core region or bremsstrahlung and atomic line emission from the Infra-Red to the Ultra-Violet. This subsection is only concerned with the large number of visible spectral plasma lines emitted by neutrals or impurity species (in hydrogen isotope plasmas). For low-Z elements such as hydrogen, helium or carbon, visible lines are intrinsically emitted by plasmas with rather low electron temperatures (between 1...100 eV). These electron temperatures are present in the plasma edge (scrape-off-layer and divertor). In the plasma core, the electron temperatures are too high for low-Z elements to emit spectral lines from electron transition, however high-Z impurities such as tungsten might. Thus, visible plasma radiation is mainly observed in the SOL and plasma-wall interaction zone[27].

Various elements are present in the SOL and divertor. From the main plasma component, the Balmer series emitted by neutral hydrogen or deuterium can be observed in the visible. The most prominent of them is the H-α-line at 656.2792 nm or D-α at 656.101 nm.

[27] An exception to this is e.g. the interaction zone of the neutral heating beams with the plasma core or injected probes, pellets etc..

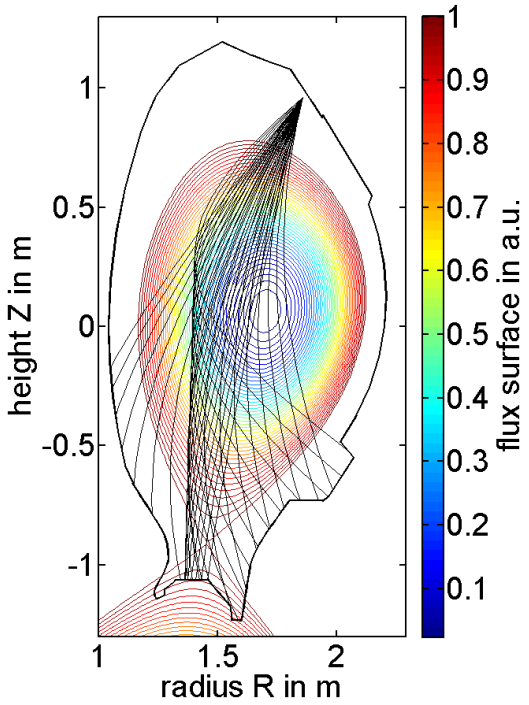

Figure 52 – Poloidal cross-section of AUG first wall and (R,Z)-projection of the magnetic flux surfaces up to the separatrix in lower divertor configuration. Some of the Doppler CIS camera sightlines in the central column and central row of the 640x480 camera image were projected into the cross-section.

To provide insight on ion dynamics with the Doppler CIS, lines of impurity species need to be used. Table 6 presents an overview of investigated impurity lines in AUG with the Doppler CIS. With the available calibration sources. only two of them and the D-α-line could be calibrated and thus successfully be measured during the course of this work. However, some impurity lines that seemed suitable for Doppler CIS measurements (but could not be measured due to lack of narrow-bandpass filters or calibration sources) are mentioned for future applications in the table.
Intrinsic impurities usually present in AUG discharges are tungsten and carbon, which are elements of the first wall components. All previous carbon tiles were replaced by either full tungsten tiles (divertor), Eurofer steel tiles (partly in the inner first wall) or tungsten-coated tiles with carbon layers underneath (in the first wall and limiter elements). By low energy neutral deuterium bombardment of residual carbon layers on metallic surfaces or carbon tile back sides in remote areas, sources of carbon still exist even in a completely tungsten-coated machine [75]. Carbon has some very well-known prominent emission lines listed in Table 6.

Another impurity that can be frequently observed in AUG is helium. The helium content in AUG varies strongly, however a small concentration is often present. Helium is often used in glow discharges to clean the device of impurities in between shots. The helium content is also relatively high after boronisations, where a combination of helium and boron is injected into the

device and a glow discharge conducted. Boronisations are a method to intermediately coat the wall surfaces with a thin boron layer to suppress wall recycling and chemical erosion. This is why after a boronisation, intrinsic impurities such as carbon remain only in low concentrations for some days and can only be measured with relatively high exposure time settings. Usually a week of operation after a boronisation, a reasonable amount of carbon has returned, whereas the boron and helium concentrations decrease.

ion species	spectral line (centre-of-mass)	number of lines
B II	412.192 nm	6
N II	462.324 nm	6
N III	463.855 nm	3
C III	**464.881 nm**	**3**
He II	**468.57 nm**	**13**
Ar II	**472.687 nm**	**1**
B II	478.421 nm	6
N II	**500.52 nm**	**3**
N II	**504.501 nm**	**3**
Ar II	**506.204 nm**	**1**
C II	**514.186 nm**	**7**
C II	657.966 nm	2

Table 6 – A selection of relatively intense spectral impurity lines present in the AUG divertor according to spectroscopic measurements. All lines that were test-measured with the Doppler CIS are marked bold.

In AUG, nitrogen is puffed regularly for radiation scenarios (e.g. to achieve complete detachment ([33])). Argon is puffed less regularly and is e.g. used during massive gas injections for disruption mitigation. In contrast to all other observed lines listed in Table 6, the argon lines did not radiate in the divertor area, but rather homogeneously from the confined region close to the separatrix. However, the discharge time in which argon radiated strongly was very short during massive gas injection experiments.

The three successfully calibrated emission lines for the Doppler CIS at AUG are listed in Table 7. The D-α-line is the most intense atomic emission line and thus required the lowest possible camera exposure time. Figure 53a shows a low-pass filtered emission intensity image of the D-α emission taken by the Doppler CIS camera (i.e. without fringes). Since D-α has a very low excitation energy (cf. Table 7) and neutral deuterium is recycled at the wall, it radiates very close to the divertor plates in attached regimes. The radiation pattern is less dependent of the magnetic field topology than for ion species.

Figure 53b shows the C III emission image at the 464.881 nm line. As helium, carbon is a low-Z impurity that mainly radiates in the divertor region of AUG, but further away from the target plates than D-α. Since He II and C III are ionized particles, they have a distinct radiation pattern dependent on the magnetic flux topology. Many camera images either reveal two or three stripes of emission maxima that appear near the strike lines in the camera images (as in Figure 53b). However not all of these lines are really strike points where the plasma hits the wall (or is 'attached'), as later analysis in subsection 7.4 will demonstrate. The emission locations will also be further discussed there.

ion	central wavelength	multiplet lines	excitation energy (averg.)	CCD exp. time	calibration source
C III	464.881 nm	3	32.2 eV	30-100 ms	Zn I (468.014 nm)
He II	468.57 nm	13	51 eV	30-100 ms	Zn I (468.014 nm)
D I	656.101 nm	8	12.1 eV	1 ms	650 nm diode (variable)

Table 7 – Atomic lines measured with the Doppler CIS in AUG.

An important feature that is revealed in the emission images in Figure 53 is reflection. Light reflection is apparent since it reveals the tile structure of the first wall (e.g. at pixels $x = 200$ and $y = 200$ in Figure 53b). It shows that these reflections could play a significant role in the quantitative analysis of the flows, especially in regions of lower plasma radiation. This is one reason why areas with emission values of lower 10% (than that of the maximum emission value) were not included in the analysis and all other areas are assumed to be dominated by real emission and, for a first order assessment of the diagnostic, reflection is neglected.

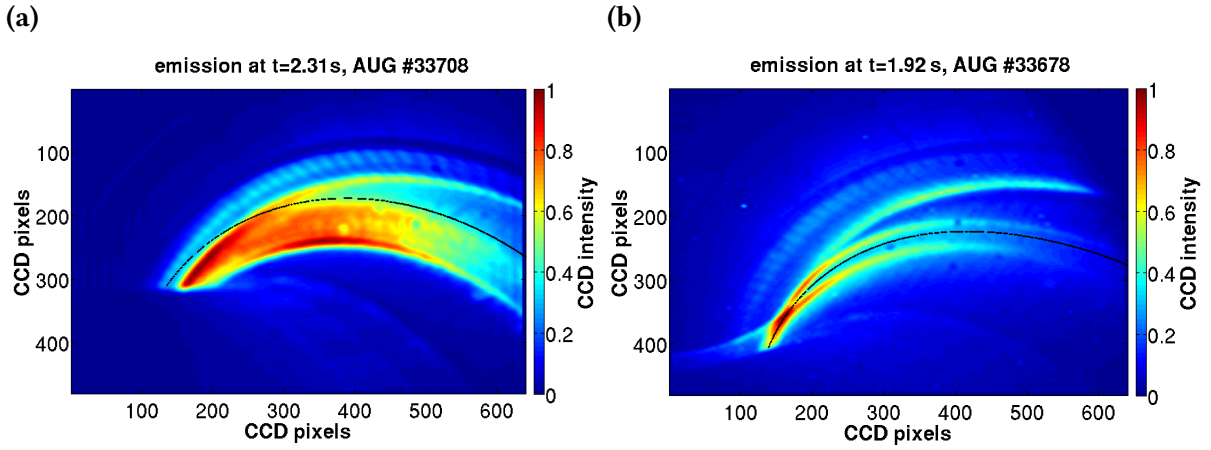

Figure 53 – Doppler CIS emission images of (a) the D-α-line and (b) the C III line at 465 nm measured during AUG discharges 33708 and 33678. The brightness data was extracted with the FFT low-pass-filter (the fringes were removed). The black line indicates the position of the X-Point.

Generally, the time resolution of the Doppler CIS was set on the order between 1-100 ms to obtain satisfactory signal-to-noise ratio. This is determined by the radiation intensity of

spectral emission lines in the AUG divertor as well as the diagnostic set-up. A major factor decreasing the light transmission in the diagnostic is the image fibre bundle (cf. Figure 68 in Appendix A.3). With the reported time resolution, general radiation or flow developments can be observed. However, the influence of short-time phenomena such as e.g. edge localized modes (ELMs) cannot be distinguished in most cases. The measured ion flows and line emission are likely to be strongly influenced by ELMs during H-Modes, that occur in the span of a few milliseconds. A camera with higher quantum efficiency and image bundles with higher transmission would need to be used in future work to isolate ELM-driven behaviour.

7.4 Survey and first observations of Doppler CIS flow measurements in AUG

The first Doppler CIS flow measurements in AUG were made during only a few short measurement periods. The amount of successfully absolutely calibrated flow data was therefore limited, since suitable calibration lines were only available during the last two periods. All of these discharges were analysed, and some of them will be presented in this subsection. The analysed flows revealed interesting features in the divertor of AUG.
The majority of flow measurements were made for He II[28] and C III[29]. A few flow measurements for neutral deuterium were performed as well, from which one will be presented here, too.

Impurity ion flow measurements

An example of a C III ion flow measurement is shown in Figure 54a. Two major counter-flow areas can be seen: the carbon ions are moving towards the observer (negative flows/blueshifted wavelength) on the HFS and away from the observer in the outer divertor (LFS). The counter-flow structure is due to the magnetic field line topology in the divertor. At the very left side of the image, the sign of the flow flips above and below the X-Point. In this region, the particle bulk velocity is integrated from both emission areas on the HFS and LFS (cf. emission image in Figure 61a), resulting in a complex mixing of the two. This is an effect from the viewing geometry, since the two emission lines overlay with each other in the diagnostic view. The point of zero observed flow in the image is close to the X-point for the majority of the discharge, which is seen as a verification for the successful calibration of the diagnostic, since a change of flow sign is expected between the two divertor legs. The flow speeds range up to $\pm 20\,\mathrm{km/s}$.
An overview of the magnetic field directions can be seen in Figure 54b. On the HFS, the poloidal magnetic field B_p is pointing upwards and on the LFS downwards. This means that for the particles to flow towards the target plates, they would need to flow towards the camera on the LFS and away from camera on the HFS. However, on both the HFS and LFS, the flows point away from the divertor plates, indicating that the measured C III flow was directed away from

[28] During AUG discharges 33349, 33351, 33352, 33354, 33356.
[29] During AUG discharges 33665, 33666, 33668, 33669, 33672, 33678, 33694, 33695, 33696, 33699, 33700.

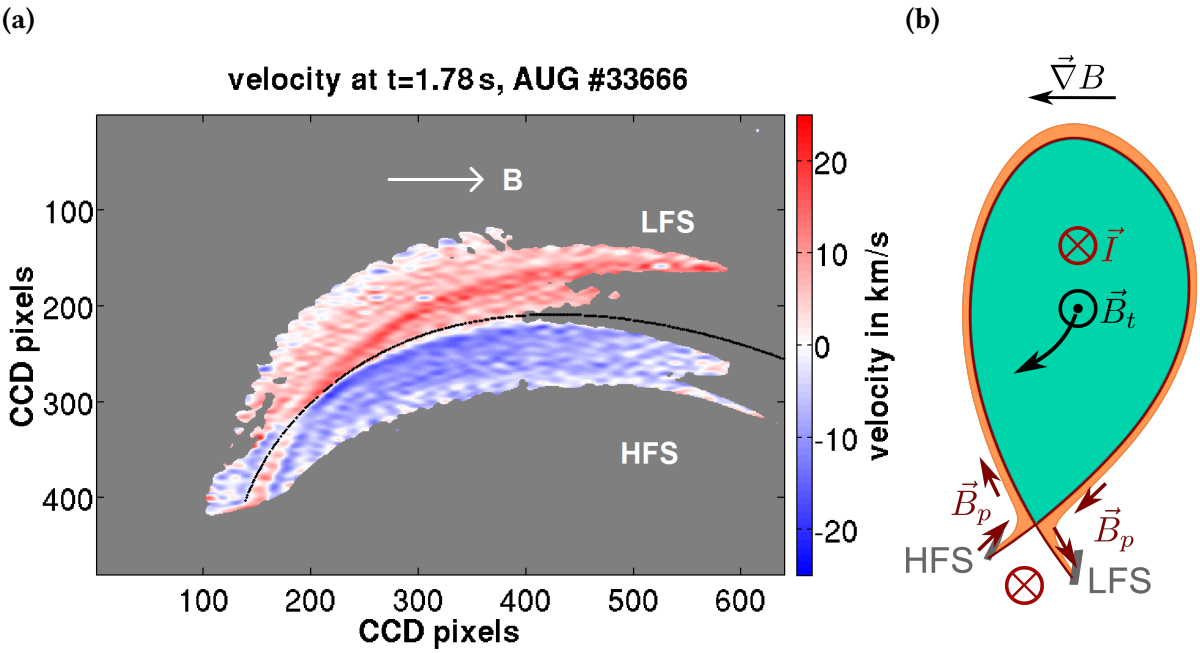

Figure 54 – (a) Measured C III flow pattern in the lower divertor of AUG. The corresponding emission image is in Figure 61a. The black line indicates the position of the X-Point. The image is greyed out where the emission intensity is below 10% of the maximum. An image exposure time of 30 ms was applied for this measurement. (b) Schematic of the magnetic field directions, black indicates the toroidal field and dark red the poloidal field (see Figure 51 for orientation).

the target plates. This is an important and interesting result, since measurements (e.g. [20]) and simulations show that the divertor main ion flow is typically towards the target plates, on both HFS and LFS (with only some rare exceptions of flow reversal, which were not the case in the AUG discharges with Doppler CIS measurements). Impurities can be entrained in the main ion flow due to friction forces (cf. Equ. (13)), however a thermal ion temperature gradient force (cf. Equ. (12)) as well as the impurity pressure force (cf. Equ. (14)) act against the friction force. Depending on the divertor regime parameters as well as the impurity distribution in the SOL, the impurities can either flow towards the divertor plates or away from it. The Doppler CIS measurement in the low-recycling regime indicates that the impurity pressure and ion thermal gradient force dominated over the friction force for the C III impurity, resulting in a flow away from the target plates.

Figure 55a shows the temporal evolution of the carbon ion flow throughout AUG discharge 33666. The flow is extracted from the sightlines that meet the divertor targets along an approximately radial line, at constant toroidal angle (illustrated in Figure 62a). For the first second of the discharge, the intensity is too low to produce a fringe pattern that can be analysed. The low signal-to-noise ratio is due to the low radiation in the divertor area because in this time interval, the magnetic configuration is bounded by the limiter and the plasma is heated ohmically. As can be seen in Figure 55b, at $t = 1$ s, the NBI and ECRH are turned on to heat the plasma and the C III line radiation increases significantly in the divertor. More NBI power is injected at $t = 1.5$ and 2 s, but doesn't change the measured flow noticeably. Between 2 and 7 s, all core

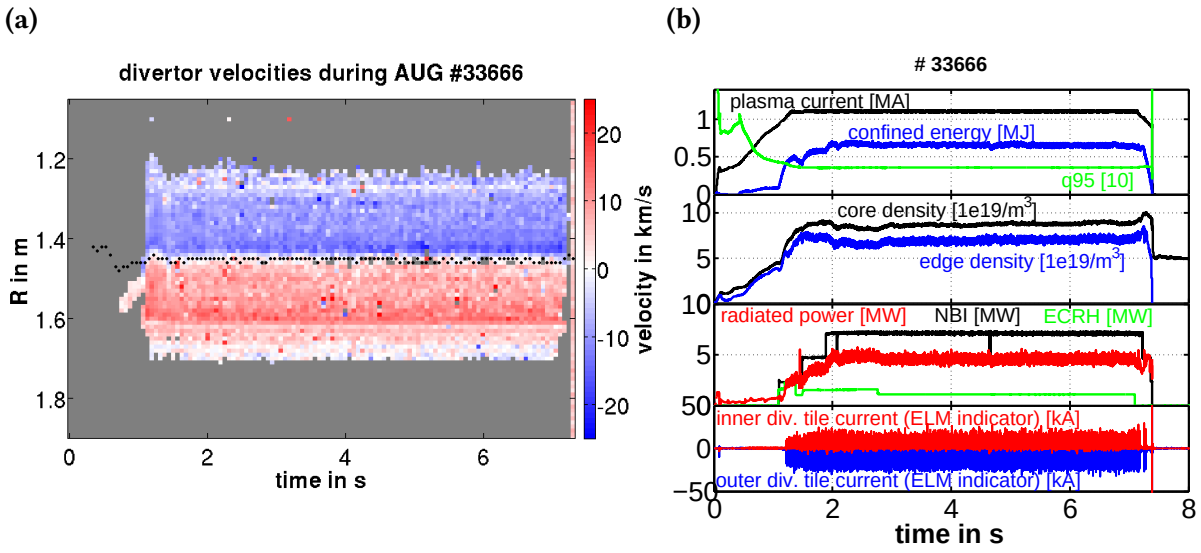

Figure 55 – (a) Line-integrated ion flow measured in the divertor by the Doppler CIS over the radius (toroidal angle constant, along the magenta line in Figure 62a) and time during the discharge for the C III line at 465 nm. The black dots indicate the position of the X-point. (b) Temporal evolution of some basic plasma parameters during AUG discharge 33666.

plasma parameters and the flow are stable.

Discharge 33666 is a relatively typical discharge in AUG, the external heating power was about 8 MW and the plasma operated in H-Mode with type-I ELMs[30]. No impurity injection was made. According to Langmuir probe data, this discharge (and all other of the successfully calibrated Doppler CIS ion flow measurements in AUG except discharge 33678) was in the attached, low-recycling divertor regime.

Discharge 33678 allows a comparison between the low-recycling and high-recycling regimes. Figure 56 shows the C III bulk flow during that discharge. The overall flow structure and flow speeds are similar to the ones recorded during 33666, however there are some local differences. The local flow maximum is higher and the minimum is lower than in discharge 33666. A different emission pattern is observed as well (cf. Figure 53b), as is expected for another divertor regime, since the temperature profile is different, which determines where C III is radiated. In Figure 57, the C III flow velocity measured during discharge 33678 is presented over time. Compared to discharge 33666, the plasma parameters were different, less external heating power was used and the discharge terminated earlier. The flow velocity maximum remains high during the short discharge. The locally different flow velocity could be either due to changed velocities or also the different radiation pattern, leading to other flow regions being integrated over.

[30]The divertor tile current in Figure 57b is used as indicator for ELMs in AUG. ELMs are an edge instability appearing during H-modes, in which plasma particles and energy from the core are expelled into the SOL on relatively short timescales

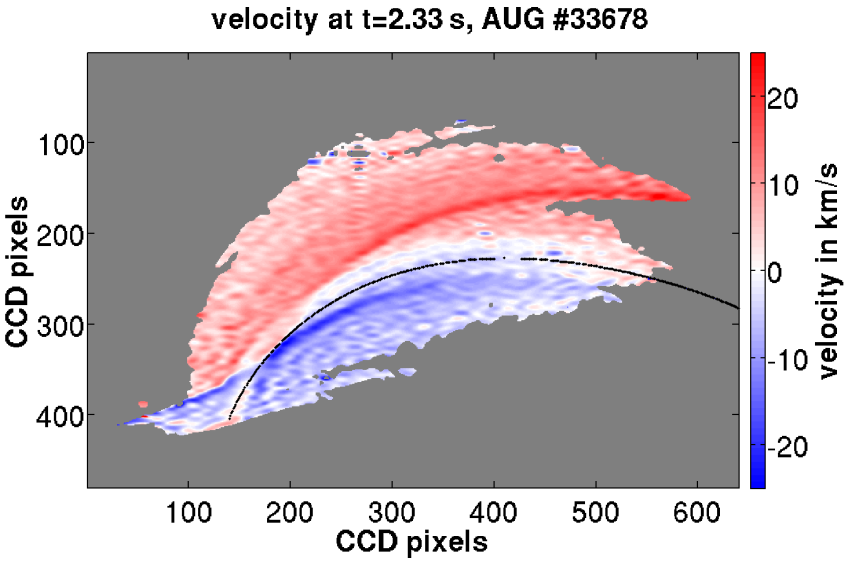

Figure 56 – Measured C III flow pattern in the lower divertor of AUG during a high-recycling discharge. The corresponding emission image is in Figure 53b. An image exposure time of 50 ms was applied for this measurement.

(a) **(b)**

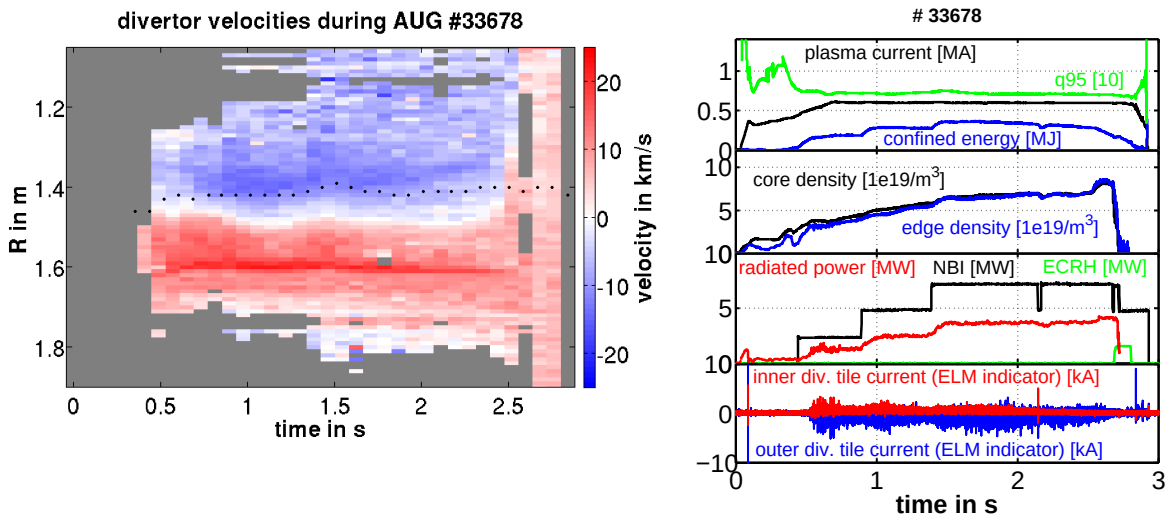

Figure 57 – (a) Line-integrated ion flow measured in the divertor by the Doppler CIS during a high recycling discharge. (b) Temporal evolution of some basic plasma parameters during AUG discharge 33678.

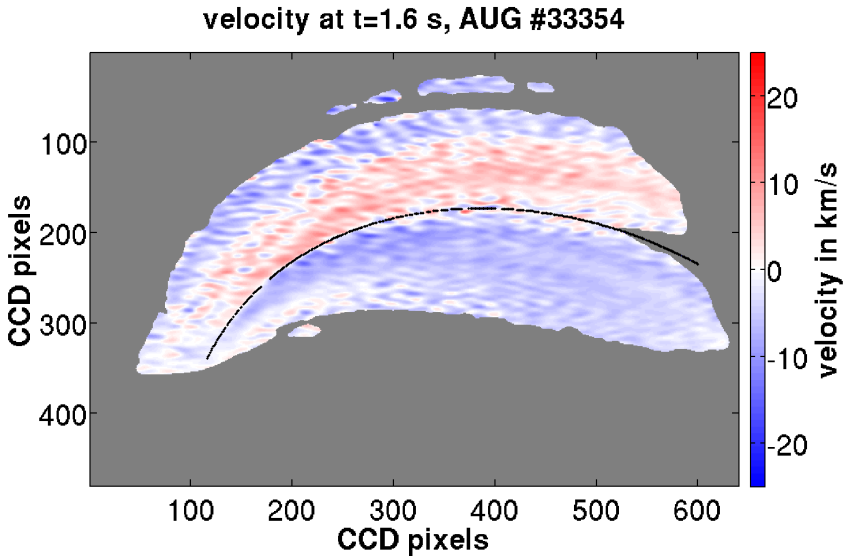

Figure 58 – Measured He II flow pattern in the lower divertor of AUG. An image exposure time of 50 ms was applied for this measurement.

(a) **(b)**

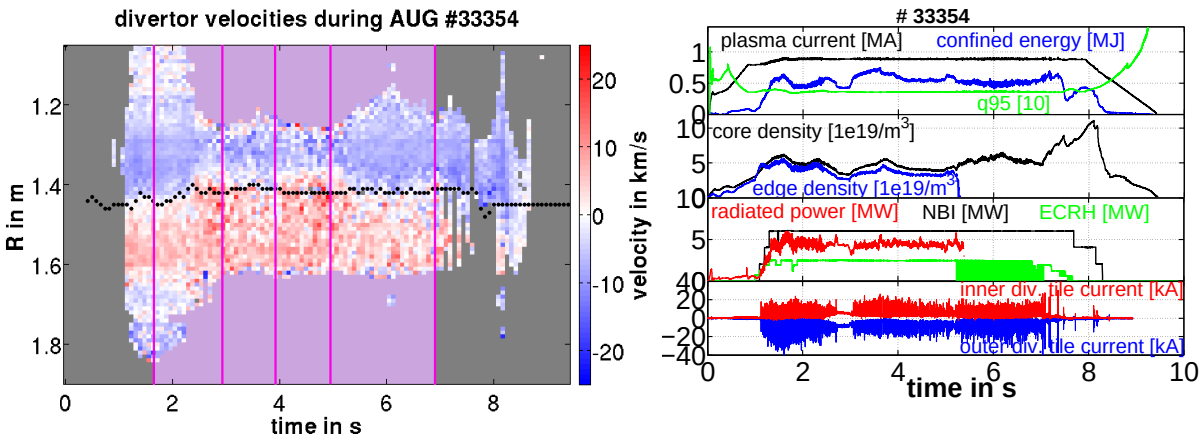

Figure 59 – (a) Line-integrated ion flow measured in the divertor by the Doppler CIS over the radius (toroidal angle constant, along the magenta line in Figure 62a) and time during the discharge for the He II line at 468 nm. The violet background and lines indicate the time during which different RMP phases were applied. (b) Temporal evolution of some basic plasma parameters during AUG discharge 33354. The divertor tile currents indicate a short, ELM-free phase induced by the application of the second RMP configuration.

He II flows are presented in Figure 58 from discharge 33354, which was in the low-recycling regime. As for C III in the low- and high-recycling regime, the He II flow was directed away from the target plates. The measured flows were more noisy than the C III flows due to poor fringe contrast and the general flow structure is the same as for the C III flows, however the flow speeds are only up to 15 km/s. During discharge 33354, resonant magnetic perturbations (RMPs)[31] were applied from $t = 1.8$ s to 7 s (Figure 58 shows a flow before RMP application). Figure 59 shows the temporal evolution of the flows along a line of constant toroidal angle. The measured Doppler CIS flows become very noisy from $t = 2.4$ to $t = 5.3$ s on the HFS. This is due to a decreased He II line emission during these phases. The plasma was operated with no gas inflow from the valves from 2.2 until 7 s during the discharge which correlates with the He II line emission decrease. The overall He II flow structure becomes changed as well at $t = 2.4$ (e.g. the position of zero flow is varied for a few centimetres), about 0.5 s after the RMPs are applied. It is not clear what causes the structural change of the flow, since it is not synchronized with the RMP onset and variations. Interestingly, the He II flow speeds remained rather constant throughout this phase.

Overall, during the AUG discharges in which C III was measured with the Doppler CIS, conditions in the divertor were relatively stable. According to Langmuir probe data, they were mostly in the low-recycling divertor regime. No nitrogen was puffed during the successfully calibrated Doppler CIS discharges, which is necessary for complete detachment in AUG ([33]). The analysed shots all appear to have very similar flow structures and speeds. For helium, the signal-to-noise ratio of the measured flow was not as good as during the C III measurements due to bad fringe contrast. The divertor regime was similar to the C III discharges, however RMPs were applied in four out of the five successfully calibrated discharges.

Neutral deuterium flow measurements

Next to the He II and C III ion flows, a few deuterium flow measurements were conducted for the D-α-line at 656.1 nm. It included only one measurement in the lower single null divertor configuration (shot 33708). Figure 60 shows a D-α flow measurement during this discharge. The neutral deuterium particles have a flow structure similar to those of the He II and C III ions, despite that they are not magnetized. The flow speed is significantly less than for the two impurities and ranges between ± 5 km/s, but it is directed away from the divertor target plates as well. The cause of this rather unexpected neutral flow behaviour is not known. If e.g. the measured neutral flow is produced by recently neutralized moving plasma ions, that have undergone a charge exchange reaction, the flow magnitude would be reasonable, however with reversed signs. The Doppler CIS flow sign, that is determined by the analysis procedure (cf.

[31] RMPs are generated with special coils to add magnetic field perturbations in the SOL to e.g. mitigate ELMs. With the application of RMPs, the magnetic field topology in the SOL is stochastised and is not 2D axisymmetric anymore.

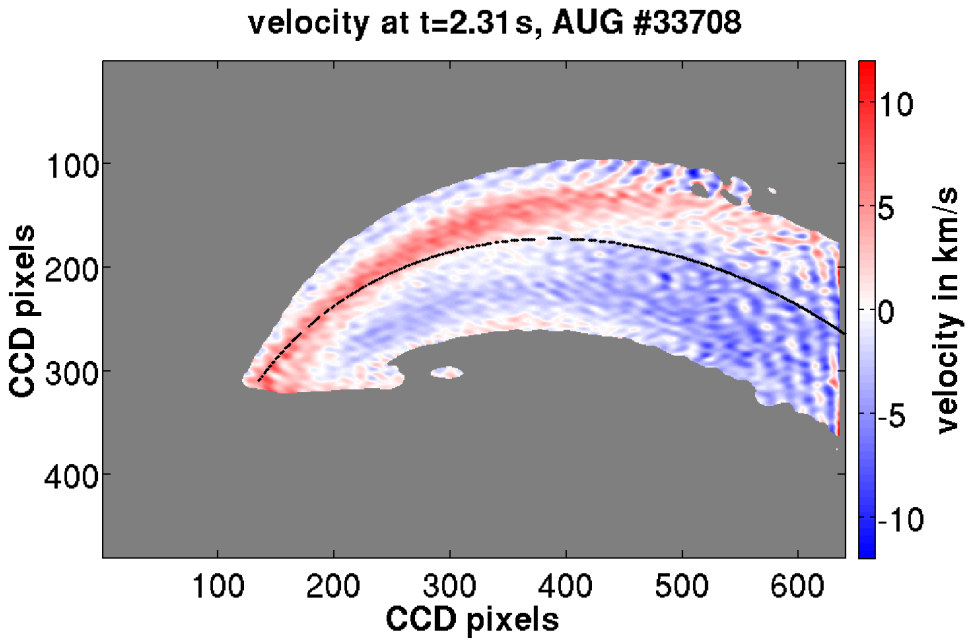

Figure 60 – Measured D-α flow pattern in the lower divertor of AUG during discharge 33708. The black line indicates the position of the X-Point. All parts of the image were greyed out where the emission intensity was below 10% of the maximum value. An image exposure time of 1 ms was applied for this measurement.

chapter 3.2.2, Equ. (41)), was confirmed with two independent methods: first, by a comparison of the plate set-up with the tunable laser measurement (cf. section 5.3), and second, by a gaussian fitting of the exact position of the $I(+)$ peaks in Fourier space (cf. Equ. (27)) during the Doppler CIS measurement for discharge 33708. Neutral distribution functions, temperature and flows have been investigated in the stellarator H-1NF with the Doppler CIS ([52] (p. 192),[76]). In this study, the edge neutral flow velocity was also found to be a little less in magnitude, but in the same direction as the edge ion flow velocity. It is not clear whether the measured flow sign was correct during discharge 33708, however, no mistake in the set-up or analysis could be found. For future applications of the Doppler CIS, a sign check is recommended directly for each plate configuration, e.g. with a tunable laser scan.
Discharge 33708 was the only discharge made with a reliable D-α calibration. Other D-α flow measurements also showed a clear flow structure, but were not absolutely calibrated and are therefore not shown here. These measurements confirmed the presence of neutral flows in the divertor and that measurement 33708 is not an exceptional case. If the measurement of the deuterium neutrals does indeed provide a proxy to measure the main ion flow, via the charge exchange, it would be very beneficial to investigate it in more detail with the Doppler CIS. However, it is beyond the scope of this work.

7.5 Flow component analysis

An important question is which component of the flows were primarily measured with the Doppler CIS in relation to the magnetic field. Generally, there are parallel as well as perpendicular flow drive mechanisms in the SOL of tokamaks (cf. chapter 2) with very different physical causes and implications. From the view into AUG (cf. Figure 51), the Doppler CIS should be able to measure both parallel and perpendicular flow components depending on their respective magnitude[32]
To investigate this question, some assumptions have to be made. Firstly, it is assumed that the effective measured Doppler CIS velocity, $v_{\mathtt{m}}$, can be expressed as the line-integrated dot product of the particle velocity $\hat{v}$ and the sightline direction $\hat{l}$, weighted with the line emission ϵ:

$$v_{\mathtt{m}} = \frac{\int (\hat{v}(l) \cdot \hat{l}) \epsilon(l) \mathrm{dl}}{\int \epsilon(l) \mathrm{dl}} \tag{49}$$

Equ. (49) is an approximation, since the Doppler CIS does not measure the particle velocity directly. To apply Equ. (49), the measured centre-of-mass of the observed spectral function must equal the average Doppler shift of the spectral line, which is e.g. only the case if there is no alien emission line or asymmetric line splitting. Complex distributions of ϵ, T_{CIII} or v along the sightline can further distort the spectral centre-of-mass. However, it can generally be assumed that the derived averaged velocity along the sightline is equal to the actual averaged line-integrated velocity if the parameters ϵ, T_{CIII} or v do not vary along the sightline, e.g. when the overall integration area is small.

To determine which flow components contributed to the Doppler CIS measured flows, a detailed analysis of the camera sightlines in relation to the magnetic field is presented in this subsection (for the low-recycling regime discharge 33666). In physical terms, the perpendicular and parallel flow components as well as their ratio can help identify and categorize important flow drive mechanisms, so the flow directions are defined as followed:

1. **parallel** to the magnetic field lines ($v_{\parallel}$)
2. **radial**: orthogonal to the (open) magnetic flux surfaces Ψ_N (v_{r})
3. **binormal**: orthogonal to the magnetic field lines, but tangential to the flux surfaces (v_{b})

Inserted into Equ. (49), the measured Doppler CIS flow in each camera pixel can be divided as:

$$v_{\mathtt{m}} = \frac{\int \epsilon \left[v_{\parallel} \left(\hat{l} \cdot \hat{B} \right) + v_{\mathrm{r}} \left(\hat{l} \cdot \nabla \hat{\Psi_N} \right) + v_{\mathrm{b}} \left(\hat{l} \cdot \left\{ \nabla \hat{\Psi_N} \times \hat{B} \right\} \right) \right] \mathrm{dl}}{\int \epsilon \mathrm{dl}} \tag{50}$$

The flows in the parallel, binormal and radial directions are weighted with the line emission

[32]The magnetic field is primarily in toroidal direction, especially in close proximity to the X-point.

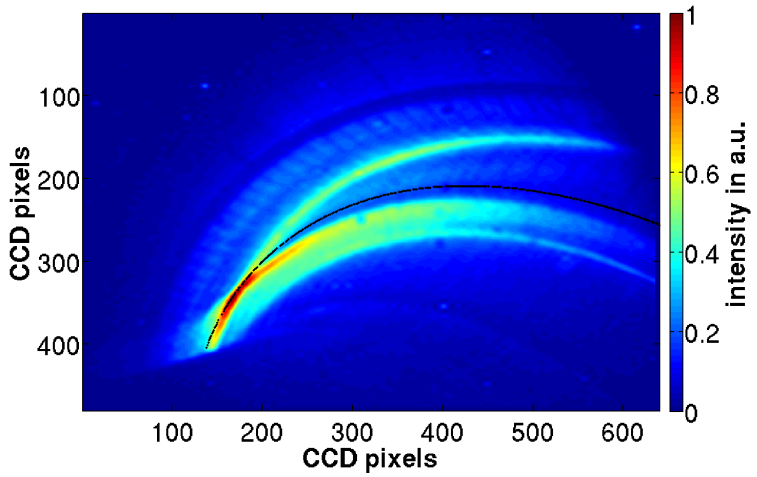

(a) C III emission image measured by the Doppler CIS camera during AUG shot 33666 at $t = 1.78$ s.

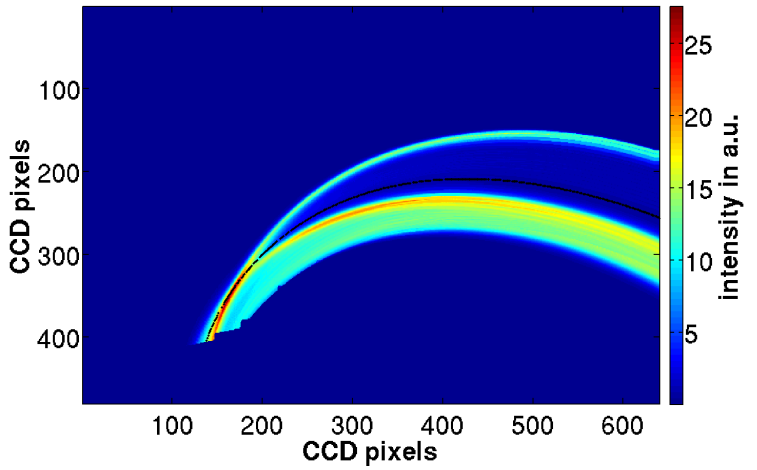

(b) Simulated C III emission image to match the measured emission image in Figure 61a.

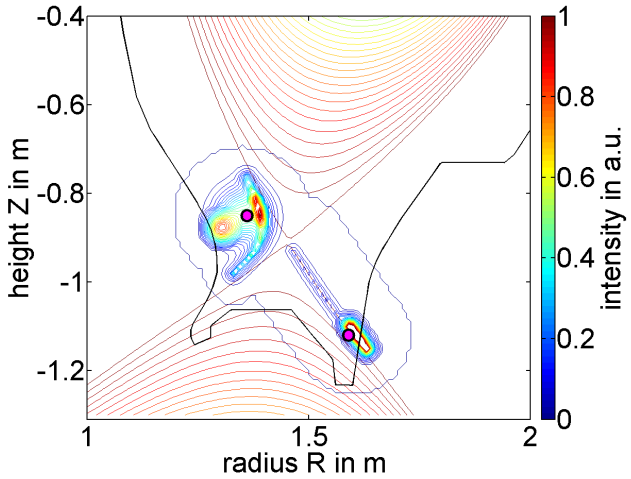

(c) Manually fitted C III emission pattern from which the simulated camera emission image in Figure 61b was determined. The magenta dots mark the position of two analysis points on HFS and LFS.

Figure 61 – Measured (a) and simulated (b) emission images for the C III line at 465 nm. The black line indicates the position of the X-Point. The magenta dots in (c) mark two analysis points on the HFS and LFS.

ϵ and the dot product of the sightline with the directional vector in relation to the magnetic field lines. In order to determine the parallel as well as perpendicular flow velocities from the measured Doppler CIS flow v_{m}, the magnetic field topology B and $\Delta\Psi$, the sightline $\hat{l}$ and emissivity ϵ in R, Z-coordinates have to be known. The sightlines are reconstructed and the magnetic field line topology is determined by the CLISTE code for each discharge, as reported in section 7.2. The line emission is not known but can be determined from the measured emission images by the Doppler CIS camera. Figure 61a shows an example of a measured C III emission image and a simulated one (Fig. 61b) from a 2D assumed emission pattern (Fig. 61c). The simulation image does not include effects from the vignetting of the diagnostic. The emission pattern was manually fitted to qualitatively reproduce the measured emission image (without knowledge of the physically expected pattern). For future applications of the Doppler CIS, a fitting algorithm is suggested for inversions of the measured line emissions into the poloidal (R, Z)-plane, however such an application was not possible in the frame of this work. The good qualitative agreement of figures 61a and 61b are deemed sufficient.
The fitted emission pattern in Figure 61c indicates a detached plasma in the inner SOL. The outer divertor is attached. This pattern is observed by bolometers (for the total radiation) as reported in e.g. [40] (Figure 7) and [77] (Figure 6, upper image). Different regimes or states of detachment on the LFS and HFS divertor are attributed to different densities, the HFS divertor density usually being higher ([40]) (for lower single null configuration and ion grad-B pointing downwards).

With the simulated emission pattern $\epsilon(R, Z)$, the reconstructed sightlines and the magnetic field topology, the line-integrated parallel and perpendicular velocity components can be determined. Radial flows may arise due to e.g. $\vec{E}_{\|} \times \vec{B}$- or diamagnetic drifts, however the parallel gradients (temperature, pressure) that cause these drifts are relatively small in low-recycling regimes such as during discharge 33666. This is why radial velocities are assumed to be on the order of just a few hundred meters per second and v_{r} is neglected.
If it can be assumed that the particle velocities $v_{\|}$ and v_{b} are constant over a certain region, Equ. (50) can be simplified:

$$v_{\mathrm{m}} = v_{\|} \underbrace{\frac{\int \epsilon \left(\hat{l} \cdot \hat{B}\right) \mathrm{dl}}{\int \epsilon \mathrm{dl}}}_{\mathrm{a}} + v_{\mathrm{b}} \underbrace{\frac{\int \epsilon \left(\hat{l} \cdot \left\{\nabla \hat{\Psi_N} \times \hat{B}\right\}\right) \mathrm{dl}}{\int \epsilon \mathrm{dl}}}_{\mathrm{b}} \tag{51}$$

This condition is fulfilled for sightlines that have only a single, small area where the emissivity is significant, which is valid in Figure 61c for sightlines that see either the LFS or HFS areas but not both. Equ. (51) has two unknowns, the line-averaged $v_{\|}$ and v_{b}, for each sightline. The integrals a and b can be calculated for each sightline from the known data. To solve the equation with the two unknowns, one has to rely on the toroidal axisymmetry of the tokamak: at each

position of the same R and Z values, the velocity components (and other plasma parameters) stay the same[33], i.e. that $v_{\parallel}$ and v_{b} are functions of only (R, Z) and not of the toroidal angle ϕ.

The measured flows in 33666 remained relatively constant throughout the discharge (cf.

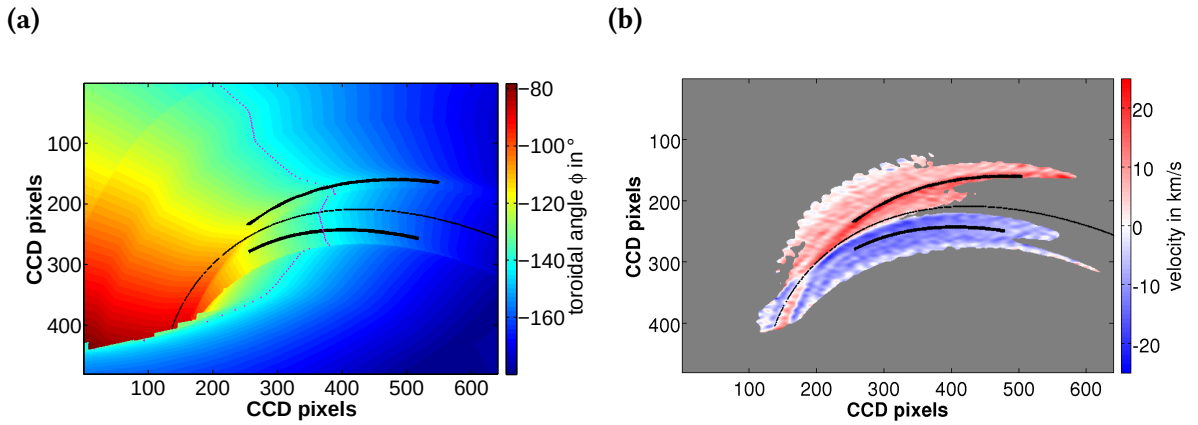

Figure 62 – (a) The toroidal position angle ϕ (at the position of contact between each sightline with the wall) in the Doppler CIS camera image. The dotted line indicates pixels of an arbitrary constant toroidal angle ϕ. (b) Time-averaged velocity during AUG discharge 33666 (from $t = 1.65\,\mathrm{s}$ to $t = 1.90\,\mathrm{s}$). The black lines indicate the position of two lines of constant r and z (cf. dots in Figure 61c).

previous subsection). Thus, Equ. (51) was solved for a time-average of v_{m} during discharge 33666 (for which the emission in Figure 61a was qualitatively fitted) to determine the integrals a and b. Two poloidal positions were chosen for the velocity component analysis: one on the HFS at $R = 1.36\,\mathrm{m}$, $Z = -0.85\,\mathrm{m}$ and one on the LFS at $R = 1.59\,\mathrm{m}$, $Z = -1.12\,\mathrm{m}$. These two points are marked in Figure 61c and their corresponding pixels in the camera view can be seen in Figure 62 over a small range of toroidal angles. The corresponding sightlines are in areas of high emission (low noise) and integrate light coming only from either the HFS or LFS. The time-averaged, measured velocity from the Doppler CIS measurement, v_{m}, and the calculated parameter integrals a and b from Equ. (51) for these sightlines can be seen as a function of toroidal angle in Figure 63. The red lines $|a|$ and $|b|$ represent the toroidal variation that would be expected for a pure parallel or binormal flow, respectively. The toroidal variation of the measured Doppler CIS velocity resembles the slope of the a-Integral, an indication that v_{m} mainly resulted from parallel flow. A linear regression with the two parameters was used to determine the velocity components, $v_{\parallel}$ and v_{b}, for both R,Z-points. The regression fit solution, $v_{\mathtt{fit}}$, can also be seen in Figure 63 and yielded the following values:

- on the HFS-line: $v_{\parallel} = 20.1 \pm 4.3\,\mathrm{km/s}$ and $v_{\mathrm{b}} = -2.1 \pm 3.3\,\mathrm{km/s}$ (stat$\pm v$ syst)
- on the LFS-line: $v_{\parallel} = -26.1 \pm 1.3\,\mathrm{km/s}$ and $v_{\mathrm{b}} = 2.9 \pm 0.7\,\mathrm{km/s}$

The signs of $v_{\parallel}$ and v_{b} define the flow with respect to the parallel or binormal direction according to Equ. (51), not to the diagnostic sightlines. Figure 64 shows an overview of the directions of

[33] 2D axisymmetry can be assumed in a tokamak with small error fields and no resonant magnetic perturbations applied, which was the case during the analysed shot (33666).

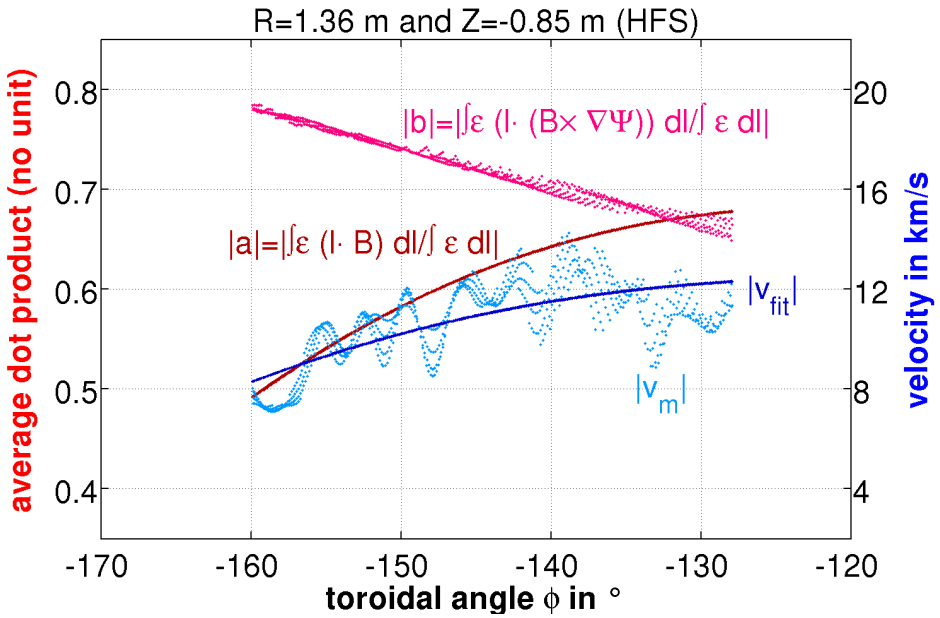

(a) Parameters for the R,Z-point on the HFS.

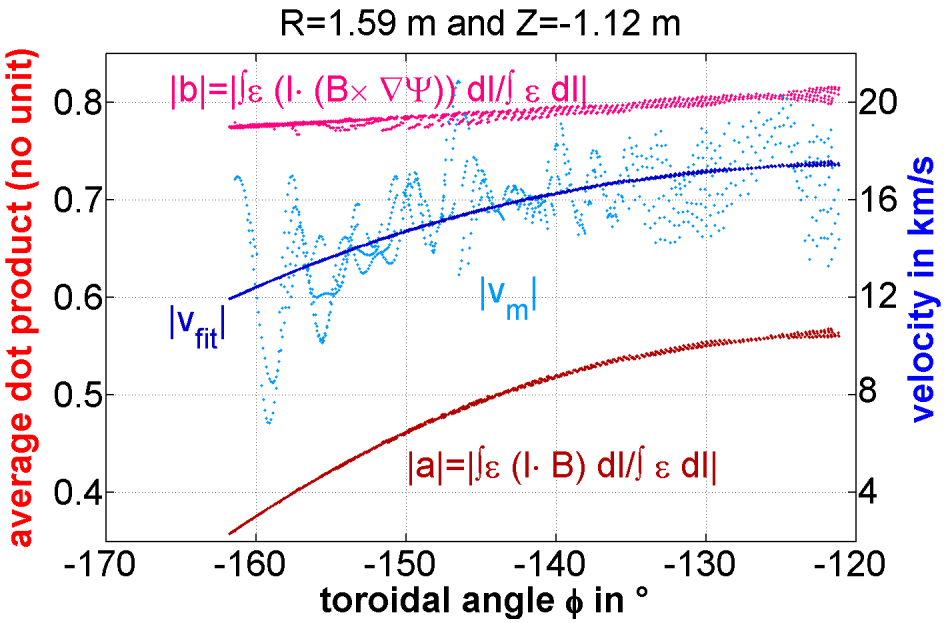

(b) Parameters for the R,Z-point on the LFS.

Figure 63 – Parameters for the determination of the parallel and binormal flow components, $v_{\parallel}$ and v_{b}, from the measured Doppler CIS velocity during AUG discharge 33666. A linear regression with the known parameters a,b and v_{m} of Equ. (51) was performed for an axisymmetric line at constant (R,Z) on the LFS and HFS each. The fitted solution, $v_{\mathtt{fit}}$, was included as well. The position of all parameters along the chosen R,Z-line is expressed by the toroidal angle defined in Figure 62a.

the parallel and binormal directions in a poloidal cut of the AUG SOL. The toroidal magnetic field points towards the observer, thus the sign of the parallel velocity indicates that the flow is towards the observer on the HFS as well, and on the LFS away from the observer. Since the radial direction (defined by $\vec{\nabla}\Psi_N$) is pointing in the same direction as the expected radial electric field E_r, binormal flows are expected to be positive. However, this is not the case on the HFS. Uncertainties were determined with an error propagation. It included the fitting errors from the linear regression, a deviation $\delta\epsilon$ between the simulated emission pattern and the measured one as well as the systematic error of the velocity signal due to the Doppler CIS analysis procedure (cf. chapter 3.2.2), being of the order of $\pm$500 to 1000 m/s for the plate configuration in AUG 33666. Since the binormal flow value is less than the uncertainty of v_{m}, the sign of v_{b} cannot be trusted.

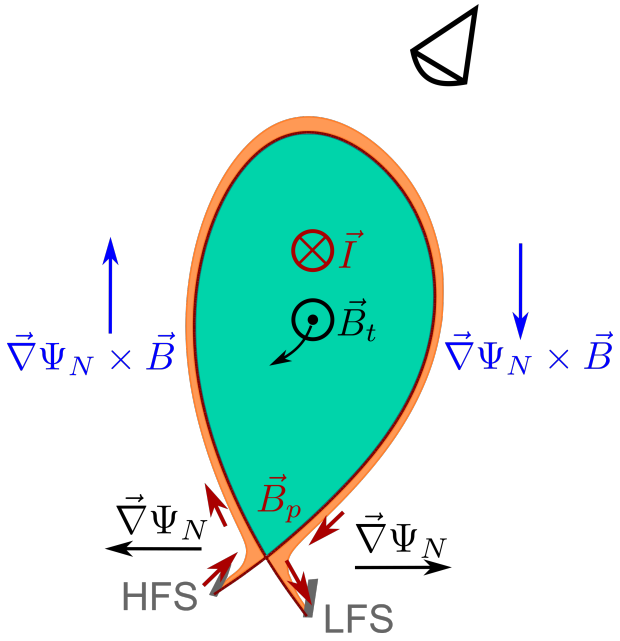

Figure 64 – Poloidal overview of the AUG SOL topology with the self-defined flow directions in relation to the magnetic field. The toroidal magnetic field pointed towards the Doppler CIS diagnostic.

The regression analysis implicates that the parallel flow was dominant for the measured Doppler CIS flow and is in the range of about 20-30 km/s. Apart from the flow sign, this agrees with SOLPS code simulations for AUG discharges in similar parameter conditions as well as with other spectral observations (cf. e.g. ([17]), Figure 3). The perpendicular, binormal flow is at most just a few kilometres per second. Small flows could arise from a combination of radial electric fields in the range of a few kV/m and diamagnetic drifts due to pressure gradients on the scale of a few millimetres. Differences might arise because of parameter variations between the HFS and LFS. Also, the C III emission (and thus the integration areas) is occurring at different distances to the target plates. On the HFS, where the flow is slightly higher and was measured in greater distance to the target plate, e.g. the thermal force could be increased due to a higher temperature gradient.

This analysis demonstrates the possibilities of the Doppler CIS, since the derived flow velocity components and the emission distribution required only a single measurement image. With a modest improvement in the uncertainty and further improvement of the procedure (e.g. a fitting routine for the (R, Z)-projection of the emission), smaller uncertainties for the flow components could be achieved, allowing for more accurate values of v_b and also a radial profile information of the flow components across the emission region. The correct simulation of the emission pattern is not only crucial for a correct value of $\epsilon(R, Z)$, but it also determines where the integral over the dot products a, b is made.

7.6 Summary

The Doppler CIS diagnostic was operated successfully for lower-single null discharges at ASDEX Upgrade. With integration times of about 30-100 ms, impurity ion flows of C III and He II were measured in the lower divertor. Neutral deuterium flows D-α were measured as well, with exposure times of 1 ms. The goal of flow measurements in the SOL and divertor is the general understanding of the plasma and impurity edge behaviour. Doppler CIS flow measurements revealed two major counter-flow areas in the divertor due to the magnetic field topology. On the HFS, they pointed towards the diagnostic camera and on the LFS away from it - analysis showed that this were both flows pointing away from the target plates for He II, C III as well as D-α. The sign can be explained for the impurities, however it is not clear what could produce the observed D-α flow pattern away from target plates.
The investigated discharges revealed remarkably, temporally constant and similar flows for each species fairly independent of core plasma parameters. Plasma core parameters can have an influence on the SOL impurity flows, since they determine drive mechanisms for the plasma ion SOL flow ([13]) which interacts with the impurities by friction forces. For He II and C III, flows in the range of 10-20 km/s were measured, for neutral deuterium it was significantly less. An analysis showed that under the assumption of constant flows in the emission regions and with toroidal axisymmetry, these flows are mainly parallel to the magnetic field lines. The procedure demonstrated that from a single image, both components of the impurity flow can be extracted, for both the HFS and LFS. Within uncertainties, this is consistent with expected physics. Theoretically, a radial variation of $v_\parallel$ and v_b could be performed, for additional (R, Z)-values. Furthermore, a poloidal emissivity distribution can be derived from a single Doppler CIS measurement image as well.

8 Overview and Conclusions

As main purpose of this work, a diagnostic set-up for absolute flow measurements in a high-temperature plasma experiment was developed. A Doppler CIS diagnostic was successfully set-up and used for plasma flow measurements in the linear, low-temperature plasma experiment VINETA.II and impurity ion and neutral flow measurements in the divertor of tokamak experiment ASDEX Upgrade. The plasma flows in VINETA.II were ranging from several hundred m/s to two km/s, whereas SOL impurity flows in AUG were on the order of 20 km/s, equivalent to Doppler line shifts of a few picometers (VINETA) and 40 pm (AUG) for the observed plasma species.

Measurements conducted in VINETA.II and ASDEX Upgrade demonstrated very clearly that for non-multiplet spectral emission lines, where a calibration source $\lambda_{\mathtt{cali}}$ for the un-shifted emission line λ_0 is provided (such as in VINETA.II), the calibration and analysis procedure is reliable and straightforward. However, absolute Doppler CIS calibration and analysis becomes more difficult when a calibration line $\lambda_{\mathtt{cali}} = \lambda_0$ is not available (such as is the case for many impurity lines in the SOL of high-temperature plasma experiments such as AUG or MAST). This is due to second order terms in the analysis procedure, that were shown here to be essential for quantitative analysis. For absolute wavelength calibration, all plate parameters (such as their thickness, the point of zero incidence angle to the plate surface normal etc.) need to be known to a very high accuracy, since the analysis procedure relies on calculations based on these parameters. Otherwise, phase errors arise due to the parameter uncertainties. In this work, these phase errors due to inaccurate plate parameters were determined by a comparison between the measured and simulated calibration phase. This solution is only possible with direct calibration before and after each measurement, because additional phase offsets between the calibration and measurement due to e.g. ambient temperature changes can be specified. Due to the plate parameter uncertainties, a small systematic error is produced for the measured flow with this method, however, it was still acceptable for the flows measured in AUG.

Next to absolute wavelength calibration, the flow sign is an important quantity to determine, since it indicates whether flows are directed towards or away from the diagnostic view. For AUG impurity and neutral flow measurements, the analysed flow sign was investigated in retrospect with two independent methods, since the measured impurity and neutral flows in the divertor were found to be counter-directed to the expected plasma flow. The sign was confirmed for the existing AUG measurements, however, a sign check is recommended for each plate configuration in future applications. Such a check was performed for a different plate configuration with a tunable laser scan, that directly yields the relation between the measured phase difference, $\Delta\Phi$ and the wavelength shift, $\Delta\lambda$.

The applied Doppler CIS set-up included a moveable mirror to reliably calibrate and exclude phase offsets due to external influences, which was necessary as active temperature control was not used. A tunable diode laser scan was performed to test the overall performance and accuracy of the Doppler CIS set-up and analysis procedure. During the measurement of the tuned laser wavelength (at $\lambda = 668\,\mathrm{nm}$), a second, fixed laser wavelength at $\lambda = 488\,\mathrm{nm}$ was measured to distinguish the fringe phase changes due to ambient temperature changes. This constitutes the first demonstration that one Doppler CIS camera system can be used to simultaneously measure two spectral lines at the same time. This is possible if:

1. those two lines are sufficiently separated from each other in Fourier space (more than 100 nm).

2. two close calibration sources for both lines exist, which could then also be used for calibration at the same time (as in the performed laboratory experiment) or a tunable laser.

3. there is an optimal plate thickness for both lines to yield a sufficient fringe contrast.

An interesting candidate for such a simultaneous measurement of two emission lines could be e.g. the C II and C III lines at 658 nm and 465 nm, to investigate flow differences of the same species at different ionization stages in the SOL.

First Doppler CIS measurements in VINETA.II enabled the study of basic plasma ion dynamics in a linear, low-temperature plasma experiment. Flows down to several hundred meters per second could be successfully detected. The ion dynamic in VINETA.II is dominated by an $\vec{E_r} \times \vec{B_z}$-drift present due to the electron temperature gradient in the plasma column. A radial electric field on the order of a few V/m is generated around the magnetic axis in case of a relatively high, peaked electron temperature of about 5 eV or stronger. The drift was only observed in a small operational range of the VINETA.II experiment (for high heating power and low initial gas pressure). Otherwise, zero flow was measured, consistent with the flat electron temperature profile in these conditions.

In AUG, successfully calibrated C III and He II flow measurements revealed impurity flows on the order of 10-20 km/s, comparable to impurity flow measurements in the SOL of other tokamaks (MAST ([24]) or DIII-D ([57])). A linear regression analysis demonstrated that these flows were mainly parallel to the magnetic field lines. For all discharges with He II and C III Doppler CIS measurements in AUG, flows were remarkably similar and were unaffected by the core plasma parameters. This implies SOL impurity flows are more determined by divertor physics than that of the core. Nearly all flows were measured in a low-recycling regime, but one discharge in high-recycling regime revealed locally higher flows, indicating that the overall flow velocity is most likely dependent on the present divertor regime. From theoretical

understanding, SOL plasma parameters determine the balance of forces acting towards and away from the target plates on the impurity particles. However, the emission pattern is also different during the high-recycling regime, thus the flow could have remained similar at each position, but line-averaged differently because the Doppler CIS only detects flows in regions of more intense line emission.
Although the available Doppler CIS flow data gathered for this work does not allow a categorical investigation into the subject, the diagnostic has been developed to a point where such studies could now be undertaken.

First 2D detailed measurements of the C III and He II flows were made at AUG and of Ar II in VINETA.II. For the Doppler CIS, an absolute calibration with a simple calibration lamp was demonstrated. The diagnostic was set-up to be compatible with operation in a fusion research environment, where access to diagnostics is limited and environmental changes are present (e.g. temperature changes). The stability of the calibration over the measurement duration was qualified. Furthermore, an analysis procedure for the extraction of emissivity, parallel and perpendicular flows from a single CIS image in an axisymmetric device was presented. The impurity flows in typical AUG discharges can be explained with the known divertor physics and seem to be more strongly determined by SOL parameters than the core plasma (that has a more significant influence on the main plasma SOL flow).

Outlook

The requirements for building a CIS diagnostic to measure magnetic reconnection in VINETA.II were briefly assessed. During a driven magnetic reconnection cycle, additional ion motion due to a $\vec{E_z} \times \vec{B_{xy}}$-drift resulting from the temporal change of magnetic topology and possibly from induced electric fields in the magnetic reconnection plane are expected. Since the driven reconnection process in VINETA.II happens on a very fast timescale ($\approx 160\mu$ s), the Doppler CIS diagnostic would require several extensive adjustments, such as a shutter and trigger to expose the camera (with a long exposure time) in the same phase of repeated reconnection cycles.

If the Doppler CIS were to be permanently installed on AUG (or another high-temperature plasma experiment), the following additions to the diagnostic are recommended:

- instalment of a tunable laser source for the Doppler CIS calibration.
- a fitting algorithm for the localisation of the observed line radiation.

Using a wide-range tunable laser source would serve three essential purposes: the possibility to calibrate any plasma emission line, simplifying the calibration procedure and analysis (with $\lambda_{\mathtt{cali}} = \lambda_0$) as well as to measure the $\Delta\Phi \rightarrow \Delta\lambda$-relation for each plate configuration directly

to increase the diagnostic accuracy. The latter would also give certainty for the flow sign. The downside of using wide-range tunable laser sources instead of calibration lamps is the loss of the significant cost advantage of the CIS system over equivalent spectroscopic systems.
A fitting routine for the tomographic inversion of the observed line emissions could be implemented to quantify where exactly the Doppler CIS measures and simultaneously determine the exact position of the line radiation in the SOL. During this work, it was shown that in a tokamak, one Doppler CIS camera is sufficient for separation of parallel and perpendicular flows if the plasma emission and flows are toroidally axisymmetric. The analysis is also dependent on the exact localisation of the emission. Additionally, impurity localisation can serve as an indicator for the type of divertor regime or the source of impurities during the discharge. Thus, in general, the inverted $\epsilon(R, Z)$ could be a very useful constraint for the SOL simulation codes.

The Doppler CIS is a powerful tool for the investigation of divertor flows during detachment as well as for flow reversal (either by magnetic field reversal or certain plasma conditions). Such data would significantly improve comparisons with SOL flow and emission simulations by e.g. the SOLPS or EMC3-Eirene codes. A initial comparison of the existing AUG flow data with SOLPS was started, however these comparisons revealed that to reliably validate the measured flows with the simulated ones, an accurate emission pattern has to be emulated with the code first. This is a task that requires careful impurity parameter settings and time, which was not possible in the frame of this work.

References

[1] Stocker, T.F. et al. (2013) Climate Change 2013: The Physical Science Basis. Working Group 1 (WG1) Contribution to the Intergovernmental Panel on Climate Change (IPCC) 5th Assessment Report (AR5) *Cambridge University Press*

[2] Wagner F. (2014) *Eur. Phys. J. Plus* **129**: 20

[3] Khan N., Kalair A., Abas N. and Haider A. (2017) *Renewable and Sustainable Energy Reviews* **72** 590-604

[4] Teixeira R.E. (2012) *Green Chem.* **14** 419

[5] Cherubini A., Papini A., Vertechy R. and Fontana M. (2015) *Renewable and Sustainable Energy Reviews* **51** 1461-76

[6] (2002) *A Technology Roadmap for Generation IV Nuclear Energy Systems* U.S. DOE Nuclear Energy Research Advisory Committee and the Generation IV International Forum

[7] (2014) *Technology Roadmap Update for Generation IV Nuclear Energy Systems* OECD Nuclear Energy Agency for the Generation IV International Forum

[8] Romanelli F., Barabaschi P., Borba D. et. al. (2012) *Fusion Electricity: A roadmap to the realisation of fusion energy* European Fusion Development Agreement, EFDA

[9] Maisonnier D., Cook I., Pierre S. et al. (2005) *Fusion Engineering and Design* **75-79** 1173-1179

[10] Meade D. (2010) *Nucl. Fusion* **50** 014004 (14pp)

[11] Chen F.C. (2016) Introduction to Plasma Physics and Controlled Fusion (3rd edition) *Springer International Publishing Switzerland*

[12] König R., Grigull P., McCormick K. et. al (2002) *Plasma Phys. Control. Fusion* **44** 2365-422

[13] LaBombard B., Rice J.E., Hubbard A.E. et. al. (2004) *Nucl. Fusion* **44** 1047-66

[14] Matsumoto H., Ogawa T., Tamai H. et. al. (1987) *Nucl. Fusion* **27** (7) 1181-7

[15] Grigull P., McCormick K., Baldzuhn J. et. al. (2001) *Plasma Phys. Control. Fusion* **43** (2001) A175-A193

[16] Howard J. (1990) *Rev. Sci. Instrum.* **61**(3) 1086

[17] Gafert J., Behringer K., Coster D. et. al. (1999) *J. Nucl. Mater.* **266-269** 365-9

[18] Hutchinson I.H. (2002) Principles of Plasma Diagnostics (2nd edition) *Cambridge University Press*

[19] Tsalas M., Hermann A., Kallenbach A. et. al. (2007) *Plasma Phys. Control. Fusion* **49** 857-72

[20] Asakura N. (2007) *Journal of Nuclear Materials* **363-365** 41-51

[21] Lester R., Zhai Y., Corr C. and Howard J (2016) *Plasma Sources Sci. Technol.* **25** 015025

[22] Chung J., König R., Howard J., Otte M., Klinger T. (2005) *Plasma Phys. Control. Fusion* **47** 919-40

[23] Micheal C., Howard J. and Blackwell B. (2001) *Rev. Sci. Instr.* **72** (1) 1034

[24] Silburn S.A., Harrison J.R., Howard J. et. al. (2014) *Rev. Sci. Instrum.* **85** 11D703

[25] Howard J., Jaspers R., Lischtschenko O., Delabie E., Chung J. (2010) *Plasma Phys. Control. Fusion* **52** 125002 (10pp)

[26] Riemann K.-U. (1994) *Contrib. Plasma Phys.* **34** (2/3) 127-132

[27] Schneider R. (2001) Habilitation Thesis: Plasma edge physics for tokamaks

[28] Stangeby P.C. (2000) The Plasma Boundary of Magnetic Fusion Devices *Institute of Physics Publishing*

[29] Riemann K.-U. (1992) *Contrib. Plasma Phys.* **32** (3/4) 231-236

[30] Shimomura Y., Keilhacker M., Lackner K. and Murmann H. (1983) *Nucl. Fusion* **23** (7) 869

[31] Borrass K. (1991) *Nucl. Fusion* **31** 1035

[32] Bernert M. (2013) PhD thesis: Analysis of the H-mode density limit in the ASDEX Upgrade tokamak using bolometry *LMU München*

[33] Reimold F., Wischmeier M, Bernert M. et al. (2015) *Nucl. Fusion* **55** 033004 (11p)

[34] Groth M., Porter G.D., Boedo J.A. et. al. (2009) *J. Nucl. Materials* **390-391** (2009) 343-346

[35] Asakura N., Sakurai S., Itami K. et. al (2003) *Journal of Nuclear Materials* **313-316** 820-827

[36] Jaervinen A.E., Allen S.L., Groth M. et al (2017) *Nuclear Materials and Energy* **000** 1-5

[37] Stacey W.M. (2009) *Phys. Plasmas* **16** 032506

[38] Feng Y., Kobayashi M., Lunt T. and Reiter D. (2011) *Plasma Phys. Control. Fusion* **53** 024009

[39] Stacey W.M. (2012) Fusion Plasma Physics (2nd edition) *Wiley-VCH*

[40] Potzel S., Wischmeier M., Bernert M. et. al. (2014) *Nucl. Fusion* **54** 013001 (19pp)

[41] Pitts R.A., Andrew P., Bonnin X. et. al. (2005) *Journal of Nuclear Materials* **337-339** 146-153

[42] Boedo J.A., Schaffer M.J., Maingi R. and Lasnier C.J. (2000) *Phys. Plasmas* **7** (4) 1075-8

[43] Chankin A.V., Corrigan G., Groth M. et. al. (2015) *Plasma Phys. Control. Fusion* **57** 095002 (11pp)

[44] Chankin A.V., Coster D.P., Asakura N. et. al. (2007) *Nucl. Fusion* **47** 479-489

[45] Stangeby P.C., Elder J.D., McLean A.G. and Watkins J.G. (2017) *Nuclear Materials and Energy* **000** 1-6

[46] Chankin A.V., Coster D.P., Asakura N. et. al. (2007) *Nucl. Fusion* **47** 762-772

[47] Lee W.D., Rice J.E., Marmar E.S. et al. (2003) *Phys. Rev. Lett.* **91** 205003

[48] Matthews G.F. (2005) *J. Nucl. Materials* **337-339** 1-9

[49] Howard J., Micheal C., Glass F. et. al. (2001) *Rev. of Scient. Inst.* (invited) **72**(1) 888

[50] Howard J. (2002) *Applied optics* **41**(1) 197-208

[51] Silburn S.A. (2014) PhD thesis: A Doppler Coherence Imaging Diagnostic for the Mega-Amp Spherical Tokamak *University of Durham*

[52] Micheal C. (2003) PhD Thesis: Doppler spectroscopy of argon plasmas in H-1NF using a coherence imaging camera *Australian National University*

[53] Veiras F.E., Perez L.I., Garea M.T. (2010) *Applied Optics* **49** (15) 2769-77

[54] Howard J. (1999) *Rev. Sci. Instrum.* **70**(1) 368

[55] Chung J. (2004) PhD Thesis: Time resolved 2D Doppler imaging of ion dynamics *Ernst-Moritz-Arndt-Universität Greifswald*

[56] Howard J. (2008) *Plasma Phys. Control. Fusion* **50** 125003 (18pp)

[57] Samuell C., Allen S.L., Meyer W.H. and Howard J. (2017) *Journal of Instrumentation* **12** C08016

[58] Ford O., Howard J. and Wolf, R.C. (2015) *Rev. Sci. Instr.* **86** 093504

[59] Bohlin H., von Stechow A., Rahbarnia K, Grulke O., and Klinger T. (2014) *Rev. Sci. Inst.* **22** 023501

[60] Biskamp D. (2000) Magnetic Reconnection in Plasmas *Cambridge University Press*

[61] Yoo J., Yamada M., Ji H. and Myers C.E. (2013) *Phys. Rev. Letters* **110** 215007

[62] Bibinov N., Halfmann H., Awakowicz P. and Wiesemann K. (2007) *Meas. Sci. Technol.* **18** 1327-37

[63] Bashkin S. and Stoner O. (1975) Atomic Energy Levels and Grotian Diagrams, Volume 1: Hydrogen I - Phosphorus XV *Elsevier*

[64] NIST Atomic Spectra Database Lines Form (August 2016) (`http://physics.nist.gov/PhysRefData/ASD/lines_form.html`)

[65] Schröder C. (2003) PhD Thesis: Experimental investigations on drift waves in linear magnetized plasmas *Ernst-Moritz-Arndt-Universität Greifswald*

[66] Haskey S.R., Thapar N., Blackwell B.D. et. al. (2014) *Rev. Sci. Instr.* **85** 033505

[67] Rognlien T.D., Ryutov D.D., Mattor N. and Porter G.D. (1999) *Phys. Plasmas* **6** 1851

[68] Rozhansky V., Kaveeva E., Molchanov P. et. al. (2009) *Nucl. Fusion* **49** 025007 (11pp)

[69] Frerichs H., Schmitz O., Evans T., Feng, Y. and Reiter D. (2015) *Phys. Plasmas* **22** 072508

[70] Lunt T., Carralero D., Feng Y. et al. (2015) *Journal of Nuclear Materials* **463** 744-747

[71] Cooke P.I.H. and Prinja A.K. (1987) *Nucl. Fusion* **27**(7) 1165-9

[72] Krasheninnikov S.I., Soboleva T.K., Batischev O.V. et. al. (1992) *Journal of Nuclear Materials* **196-198** 899-903

[73] Wagner F., Becker G., Behringer K. et. al. (1982) *Physical Review Letters* 49 (19) 1408-12

[74] McCarthy P.J., Martin P. and Schneider W. (1999) The CLISTE Interpretive Equilibrium Code (IPP 5/85) Garching: Max-Planck-Institut für Plasmaphysik

[75] Brezinsek S., Widdowson A., Mayer M. et al. (2015) *Nucl. Fusion* **55** 063021

[76] Michael C., Howard J. and Blackwell B.D. (2004) *Phys. Plasmas* **11** (8) 4008

[77] Kallenbach A., Bernert M., Beurskens M. et al. (2015) *Nucl. Fusion* **55** 053026

[78] Kato K. (1986) *IEEE Journal of Quantum Electronics* **22** (7) 1013-4

[79] Shi H.S., Zhang G., Shen H.Y. (2001) *J. Synthetic Cryst.* **30** 85-8

[80] Zelmon D.E., Small D.L., Jundt D. (1997) *J. Opt. Soc. Am. B* **14** (12) 3319-22

[81] Ghosh G. (1999) *Optics Communications* **163** (1999) 95-102

A Appendix

A.1 Sellmeier coefficients

A.1.1 For the short Sellmeier Equation (19)

material	**refractive index**	$A_{e,o}$	$B_{e,o}$ (μm^2)	$C_{e,o}$ (μm^2)	$D_{e,o}$ (μm^{-2})	**source**
α-BaB_2O_4	n_o	2.7359	0.01878	-0.01822	-0.01354	[78]
	n_e	2.3753	0.01224	-0.01667	-0.01516	
YVO_4	n_o	3.778790	0.07479	-0.045731	-0.009701	[79]
	n_e	4.607200	0.108087	-0.052495	-0.014305	

Table 8 – Sellmeier coefficients for α-BaB_2O_4 and YVO_4.

A.1.2 For the three-oscillator Sellmeier Equation (20)

material	**refractive index**	$A_{e,o}$	$B_{e,o}$ (μm^2)	$C_{e,o}$	$D_{e,o}$ (μm^2)	$E_{e,o}$	$F_{e,o}$ (μm^2)	**source**
$LiNbO_3$	n_o	2.6734	0.01764	1.2290	0.05914	12.614	474.6	[80]
	n_e	2.9804	0.02047	0.5981	0.0666	8.9543	416.08	
$CaCO_3$	n_o	0.73359	0	0.96464	0.0194325	1.82831	120	[81]
	n_e	0.35860	0	0.82428	0.0166895	0.14429	120	

Table 9 – Sellmeier coefficients for $LiNbO_3$ and $CaCO_3$.

A.2 Multiplet spectral lines measured in ASDEX Upgrade

For the Doppler CIS analysis, the relative line ratio, $I_{\mathrm{rel},j}$, of a multiplet with n lines as well as its wavelength position need to be known. The exact line positions were taken from the NIST databank[34]. The (expected) relative intensity of each multiplet is determined with the statistical weight of its upper state, g_k, according to [22]:

$$I_{\mathrm{rel},j} = \frac{A_{k\to i,j} g_{k,j}}{\lambda} \cdot \frac{\sum_{j=1}^{n} \lambda_j}{\sum_{j=1}^{n} A_{k\to i,j} g_{k,j}} \tag{52}$$

In [51], the calculated relative intensities were found to be in good agreement with the measured ones.

wavelength λ_j (nm)	$A_{k\to i}$ (10^8/s)	g_k	g_i	I_{rel}
464.7418	0.726	5	3	0.5561
465.0246	0.725	3	3	0.3330
465.1473	0.724	1	3	0.1108

Table 10 – Spectral parameters of the C III multiplet at $\lambda_0 = 464.881\,\mathrm{nm}$. The transition is from $n_k = 3 \to n_i = 3$.

wavelength λ_j (nm)	$A_{k\to i}$ (10^8/s)	g_k	g_i	I_{rel}
468.5377	0.939	4	2	0.0816
468.5407	0.491	4	2	0.0427
468.5524	0.098	2	2	0.0043
468.5568	0.491	2	2	0.0213
468.5704	2.06	6	4	0.2685
468.5704	1.127	6	4	0.1469
468.5757	0.006	4	4	0.0005
468.5758	0.188	4	4	0.0163
468.5804	2.207	8	6	0.3835
468.5831	0.147	6	6	0.0192
468.5884	0.05	4	6	0.0043
468.5906	0.196	2	4	0.0085
468.5918	0.056	2	4	0.0024

Table 11 – Spectral parameters of the He II multiplet at $\lambda_0 = 468.57\,\mathrm{nm}$. The transition is from $n_k = 4 \to n_i = 3$.

[34] `https://www.nist.gov/pml/atomic-spectra-database`

wavelength λ_j (nm)	$A_{k\to i}$ (10^8/s)	g_k	g_i	$I_{\mathtt{rel}}$
656.0925	0.539	4	2	0.1357
656.094	0.225	4	2	0.0567
656.0967	0.021	2	2	0.0026
656.0986	0.225	2	2	0.0283
656.101	0.441	18	8	0.4997
656.1067	0.647	6	4	0.2444
656.1082	0.108	4	4	0.0272
656.1124	0.042	2	4	0.0053

Table 12 – Spectral parameters of the D I multiplet at $\lambda_0 = 656.1\,\mathrm{nm}$. The transition is from $n_k = 3 \to n_i = 2$.

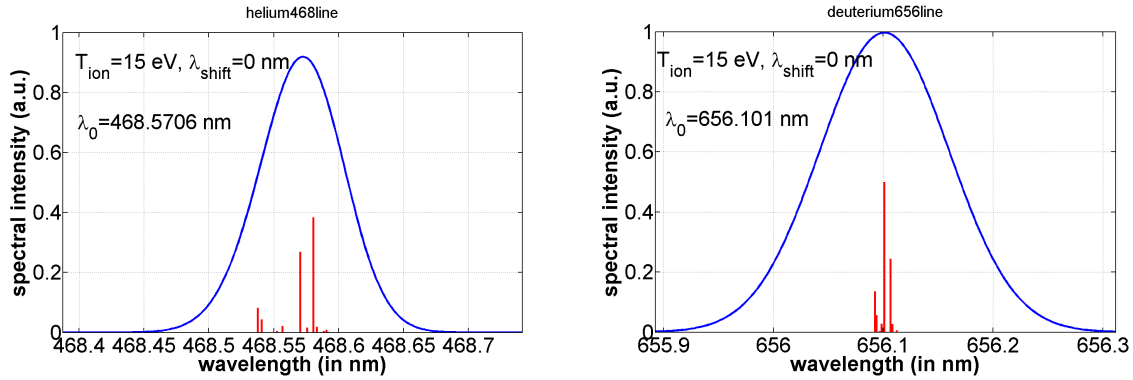

Figure 65 – Left image: Spectrum of the He-II multiplet at 468.57 nm. Right image: Spectrum of the D-I multiplet at 656.1 nm.

A.3 Image fibre bundle

The usage of an image fibre bundle in the set-up of the Doppler coherence imaging system proved to have some perturbing disadvantages, but also some advantages. The used image fibre bundles were produced by Schott USA. They are composed of about $7.5 \cdot 10^5$ single fibres melded together at their ends and had a length of about 4.5 m. A picture of the image fibre bundle used for the VINETA.II measurements can be seen in the left image of Figure 66.

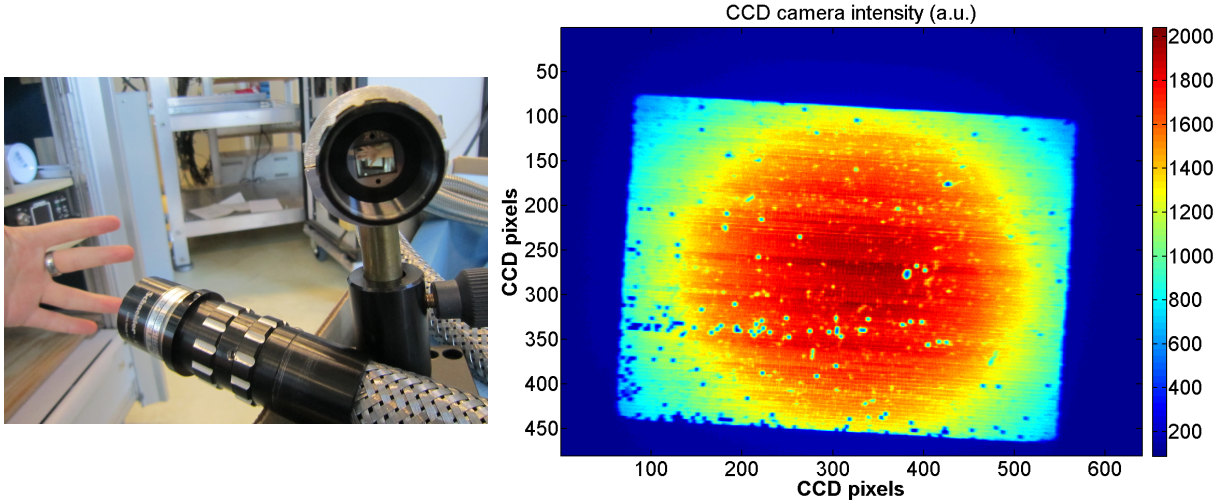

Figure 66 – Left: Image fibre bundle used for the Doppler CIS measurements in VINETA.II. An $f = 8\,\text{mm}$ lens was mounted onto one end of the bundle. Right: Focused image of image fibre bundle end to investigate its destroyed fibres. The entire size of the image fibre guide end is about 9.7 mm x 7.7 mm. The picture was taken with the CCD camera. A white lamp source was used to illuminate the other end of the image bundle. In the image, the so-called multi-fibres are roughly recognizable as a rectangular pattern, each with a size of about 50 μm x 50 μm and consisting of 5 x 5 single fibres.

In the right image of Figure 66, some of the fibres of the image guide are destroyed. This is mainly due to the manufacturing process, by which some of the fibres break. However, some destroyed fibres can also arise due to wrong handling of the image guides.
Broken fibres are a problem for measuring with the Doppler CIS, because they produce gaps in the interference pattern of the birefringent crystals. Furthermore, the small periodic rectangular pattern produced by the multi-fibres disturb the Fourier image of the birefringent interference pattern. To avoid these effects, the objective lens at the diagnostic end of the image guide needs to be slightly defocused (in relation to the end of the image guide).

In order to determine the numerical aperture

$$A = n \cdot \sin \alpha \tag{53}$$

of the image guide, a simple experimental scheme was arranged in the laboratoy. This can be seen in Figure 67. The maximum incidence angle α under which light could enter the image guide, was found to be $\alpha = 36.5 \pm 3.7\,^\circ$. That corresponds to a numerical aperture of

$A = 0.59 \pm 0.05$ (with $n = 1$ being the refractive index of air). While measuring, a circular pattern was observed at the end of the image guide (cf. Figure 67). The emergent angle of the light at the end of the guide is mainly the same as its incidence angle. The bigger the incidence angle, the larger the diameter of the circle. For $\alpha = 0\,^\circ$ a bright spot was observed on the white screen.

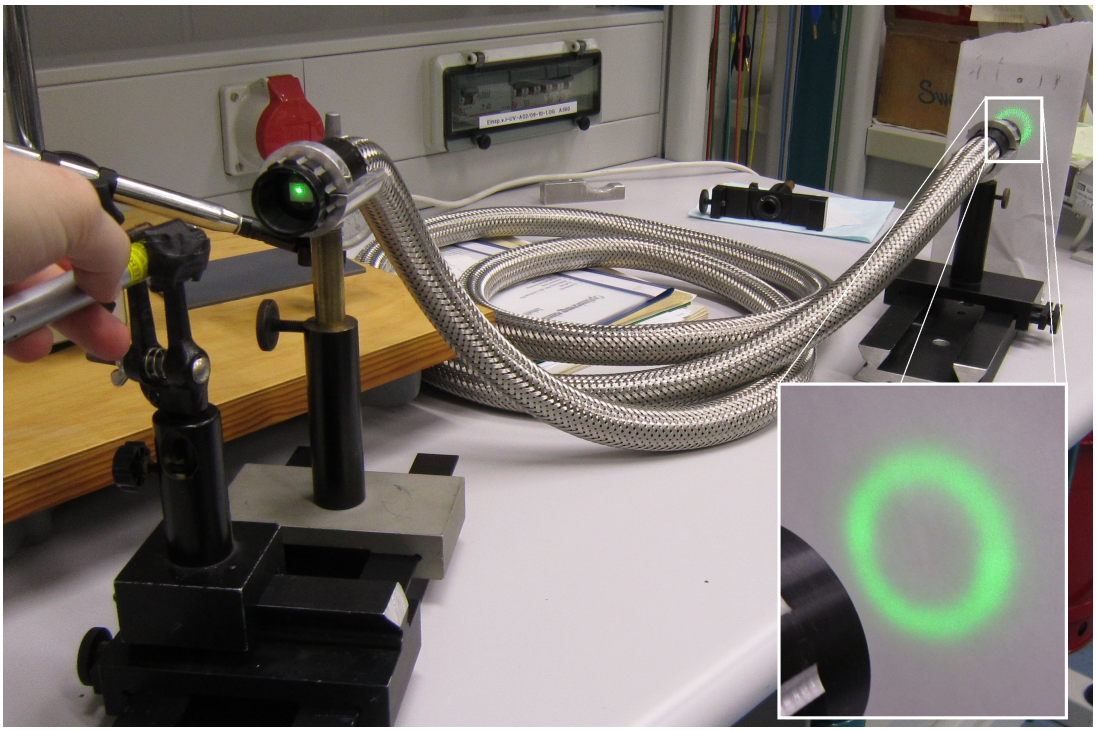

Figure 67 – Set-up for the determination of the numerical aperture of the image guide. A green laser pointer was used to measure the emergent angle of the light at the other end of the image guide.

During a period of several months AUG operation, the transmission of the plasma light through the image fibre bundle was considerably reduced. This is due to neutrons that are mainly produced by the injection of deuterium neutral beams into a deuterium plasma. The neutrons induce displacements in the crystal lattice of the fibres that decrease their transmission. In order to restore the transmission, the bundle can be heated in a vacuum oven. By the heating (or "baking") of the fibre bundles, the defects caused by the neutrons are healed. An oven temperature of 230 C° (200°C at the image fibre bundle) for 48 hours is necessary.

To quantify the effect of the baking, the transmission of a used image fibre bundle before and after baking was measured. This is shown in Figure 68. By the heating of the fibres, the transmission was increased at least for an order of magnitude in the blue part of the spectrum. This was very important for the Doppler CIS measurements of the He II and C III multiplets at 468.57 nm and 464.88 nm respectively, since the transmission was nearly zero. For the red wavelengths, the fibre bundle transmission is generally higher. During the Doppler CIS measurements in AUG, it was found that a reduction of the image bundle transmission similar to the one in Figure 68 can take place in the frame of several weeks. For another image fibre

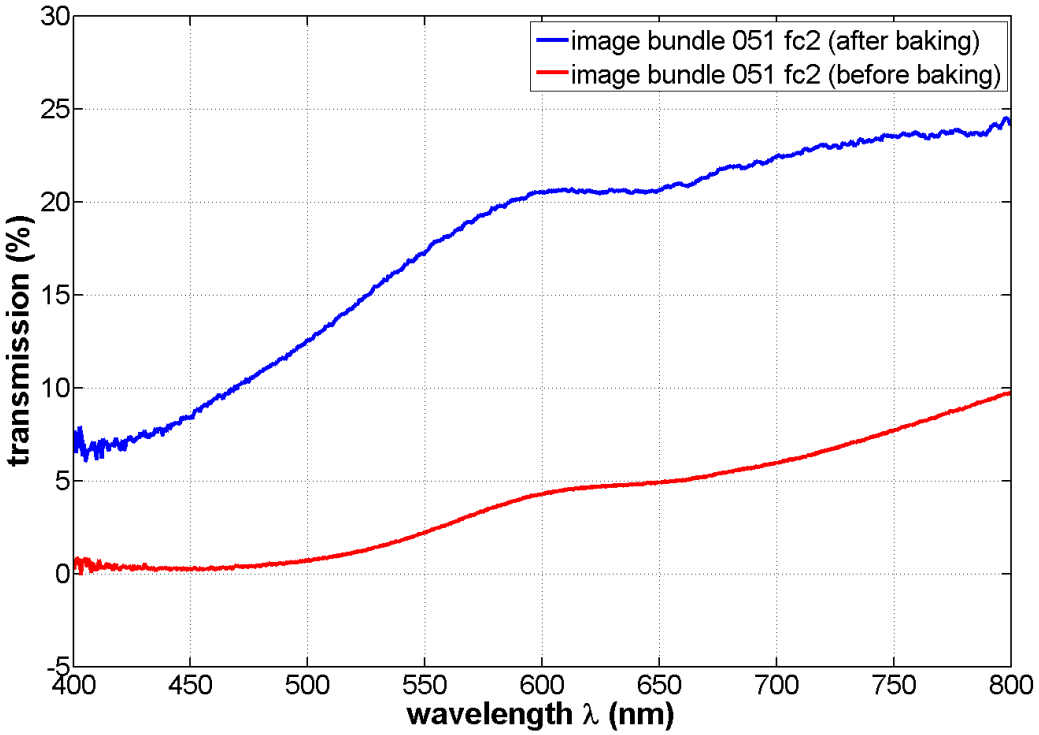

Figure 68 – Transmission curves of an image fibre bundle used for the Doppler CIS measurements in AUG. Image bundle 051 fc2 was used in the AUG torus hall during March and April 2016. Its transmission was measured before (red line) and after (blue) baking in a vacuum oven.

bundle, that was used without a break from July 2015 until March 2016 in the AUG torus hall, the transmission was even worse than in Figure 68. For future applications of the Doppler CIS in AUG, it is therefore recommended to switch and heat the used image fibre bundles every month (during deuterium plasma operation). Generally, an image fibre bundle with low transmission can be recognized with the naked eye. As a rule of thumb, if a white lamp source is transmitted white at the other end of the image fibre bundle, the transmission is fine. If the white source is appearing yellow or even red, then the transmission of the image fibre bundle is reduced.

Another disadvantage of the image fibre bundle was the sometimes difficult handling of it: one half of the image bundle was positioned in an immersion tube that had a bend close to its inner end. The removal and re-positioning of an image fibre bundle proofed to be time-consuming, as it was not easy to fiddle the image fibre end around the bend at the inner end of the immersion tube.
However, the use of the fibre bundle allowed a diagnostic position further away from the magnetic field coils of ASDEX Upgrade. The diagnostic was placed on top of a deflection box, right next to the protection shield of one of the neutral beam boxes. Furthermore, the ambient temperature of the crystal plates proved to be stable during the AUG discharges and was just

changing more strongly after switching on the CCD camera.

A.4 Projection of light orientation angles on CCD chip

In order to calculate the phase Φ between the ordinary and extraordinary ray on the CCD chip (according to Equ. (15)), the incidence angle α and the angle between the incidence light plane and the projection of the optical axis on the birefringent plate surface, δ, need to be known. With Φ, the interference signal S (conf. Equ. (26)) can be simulated. In this subsection, the projection of the birefringent plate angles α and δ (conf. Equ. (15)) onto the CCD chip is explained.

Each CCD pixel is assigned to an (x,y)-coordinate that can be translated into an α and δ-value. The range of the incidence angle α is defined by the chip proportions as well as the objective lens in front of the CCD chip. All the light that is collected in a single CCD pixel has the same incidence angle on the birefringent plate. A schematic can be found in Figure 69, where the incidence angle α on the birefringent plate is the same angle of the CCD pixel in relation to the optical axis of the objective lens. Thus, the incidence angle α on the birefringent plate can

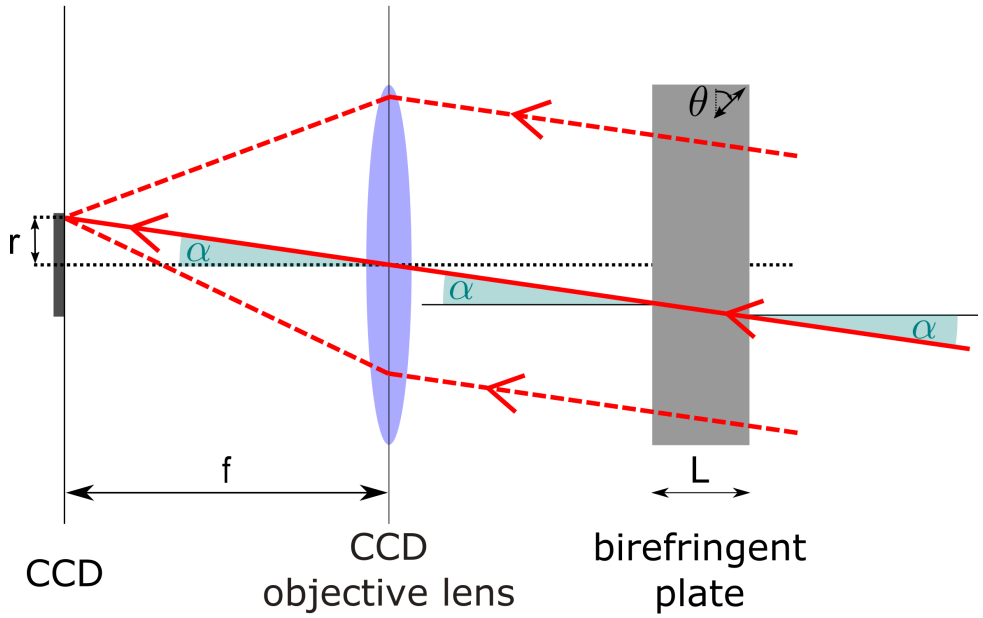

Figure 69 – Projection of the light incidence angle α on the birefringent plate and on the CCD chip.

be calculated for each CCD pixel according to:

$$\alpha(x, y) = \tan^{-1}\left(\frac{r}{f}\right)$$

where $r = \sqrt{(x - M_x)^2 + (y - M_y)^2}$ is the distance of each CCD pixel to the central pixel (M_x, M_y). The central pixel is defined as $\alpha = 0$. f is the focal length of the objective lens in front of the CCD. An example calculation for α is provided in Figure 70a.

δ is simulated in a similar way. As for α, the central pixel (M_x, M_y) is the reference point. δ rotates around (M_x, M_y). It is necessary to define an orientation for δ, meaning the direction of the projection of the optical axis of the plate on its surface. It should correspond to the orientation of the plates in the experimental set-up. There are several ways of how to calculate δ. In this work, the central pixel was chosen to divide the CCD chip area into four quadrants, where $\delta(x, y)$ is calculated differently in each quadrant. The computation of δ is based on trigonometric considerations, see Figure 71.

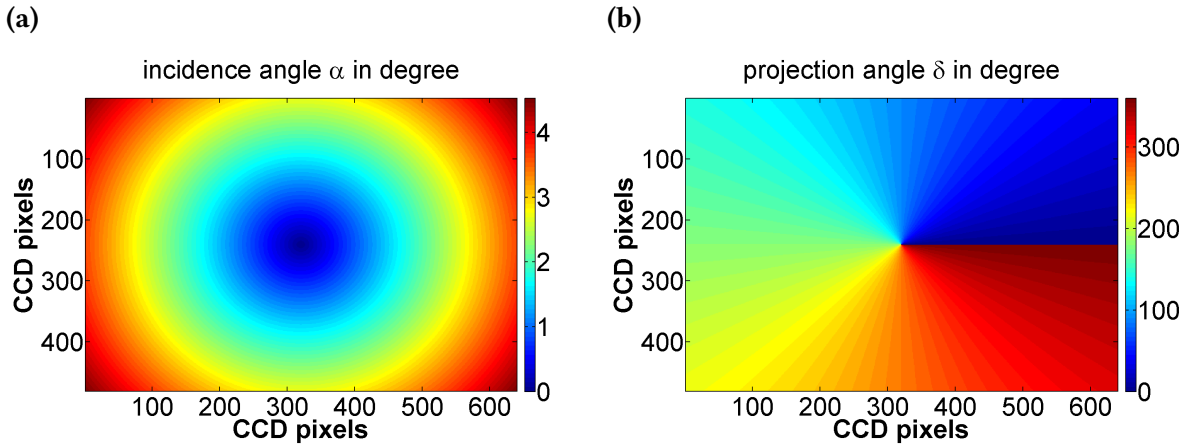

Figure 70 – Calculated projection of (a) incidence angle α and (b) angle δ from the birefringent plate on the CCD chip. The focal length of the objective lens was set to $f = 50$ mm and the size of 1 CCD pixel is $9.9\,\mu$m. For these parameters, α is in the range of $0 \leq \alpha \leq 4\,^\circ$. δ is in the range of $0 \leq \alpha \leq 360\,^\circ$ (if (M_x, M_y) is a pixel on the CCD chip). Both angles are necessary for the simulation of the fringe phase Φ according to Equ. (15).

For the first and third quadrant, an angle is identified by

$$\beta(x, y) = \sin^{-1}\left(\frac{M_y - y}{r}\right)$$

and for the second and fourth quadrant, it is

$$\gamma(x, y) = \cos^{-1}\left(\frac{M_y - y}{r}\right).$$

For each quadrant, δ can be thus determined according to:

1. quadrant: $\delta = \beta$
2. quadrant: $\delta = \gamma + 90\,^\circ$
3. quadrant: $\delta = \beta + 180\,^\circ$
4. quadrant: $\delta = \gamma + 270\,^\circ$

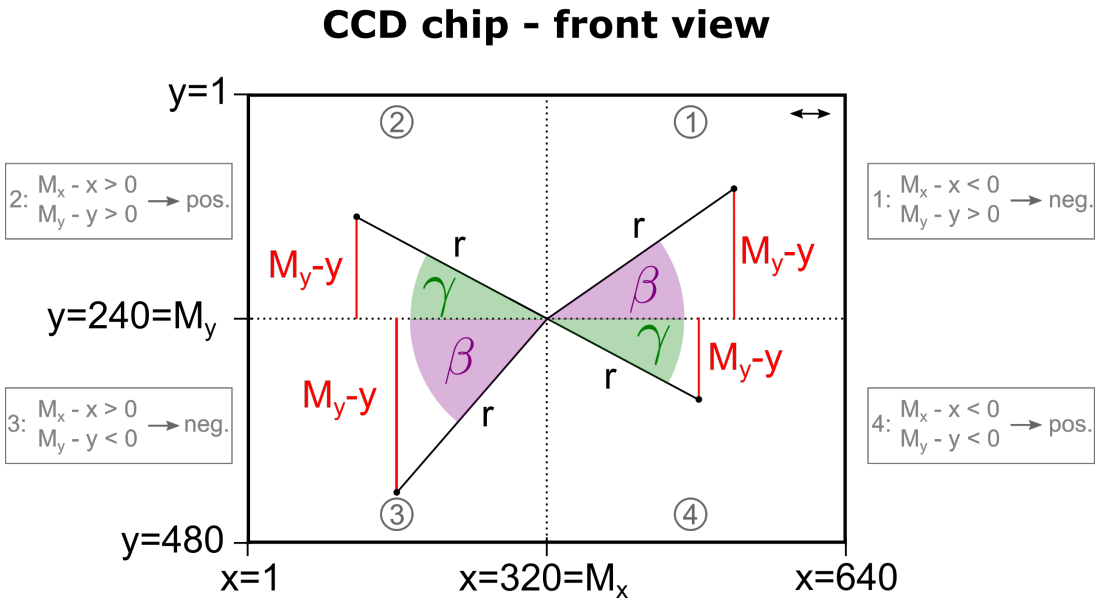

Figure 71 – Schematic of how the projection angle δ is determined for a CCD chip with 640x480 pixels. In the upper right corner, the orientation of the projected optical axis of the birefringent plates is included. The information in the gray boxes might help to select the quadrants in a code.

An example calculation for δ is provided in Figure 70b. In this example, the orientation of the birefringent plate optical axis was set in horizontal direction.

A.5 VINETA spectra

The three noble gases (see Figure 72) available for VINETA.II were spectrally investigated. The argon spectra are described in chapter 6.2, whereas examples of helium and neon spectra can be found here (cf. Figures 73 and 74). The spectrum was measured with an echelle grating spectrometer.

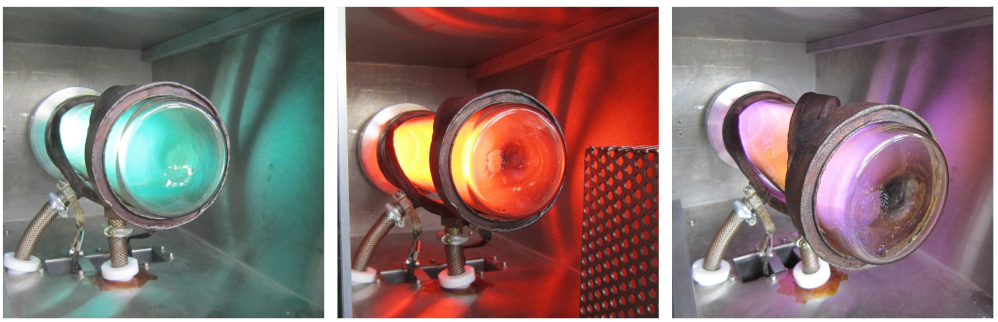

Figure 72 – Different working gases used for plasma generation in VINETA.I. Left image: Helium. Middle image: Neon. Right image: Argon. The plasmas were produced in low power discharges (< 500 W) with the helicon cell of VINETA.I.

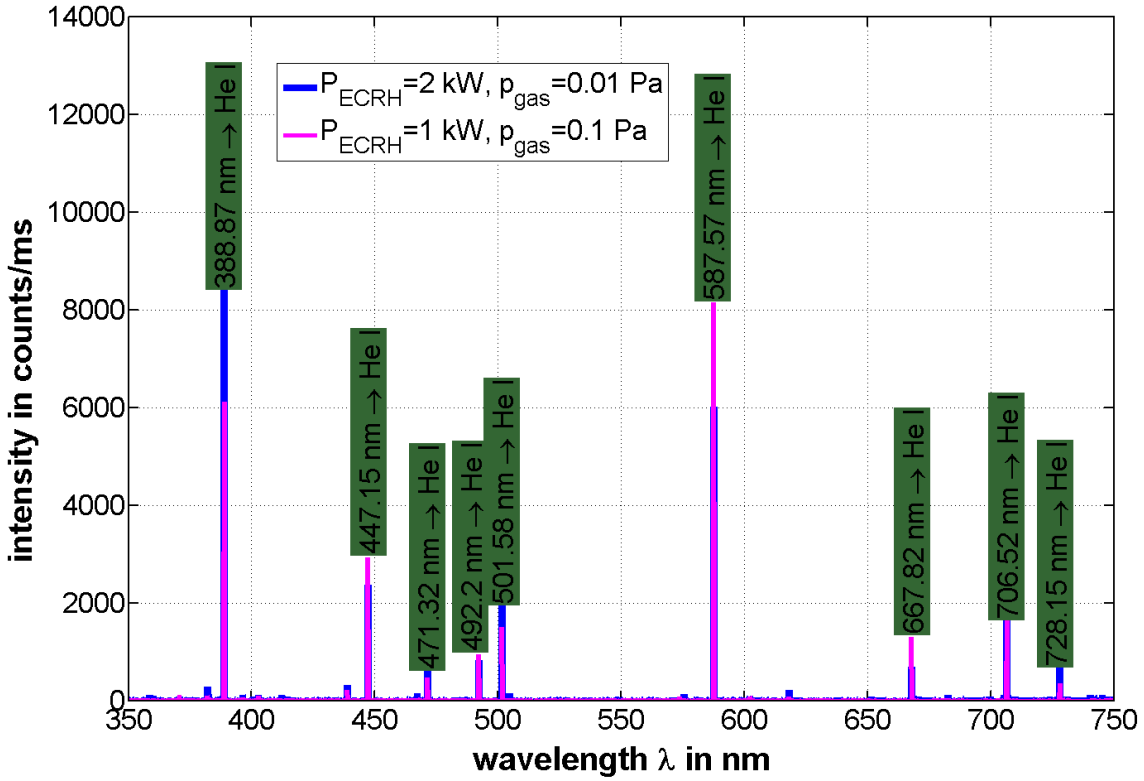

Figure 73 – Emission spectrum of a helium discharge in VINETA.II for different operation parameters.

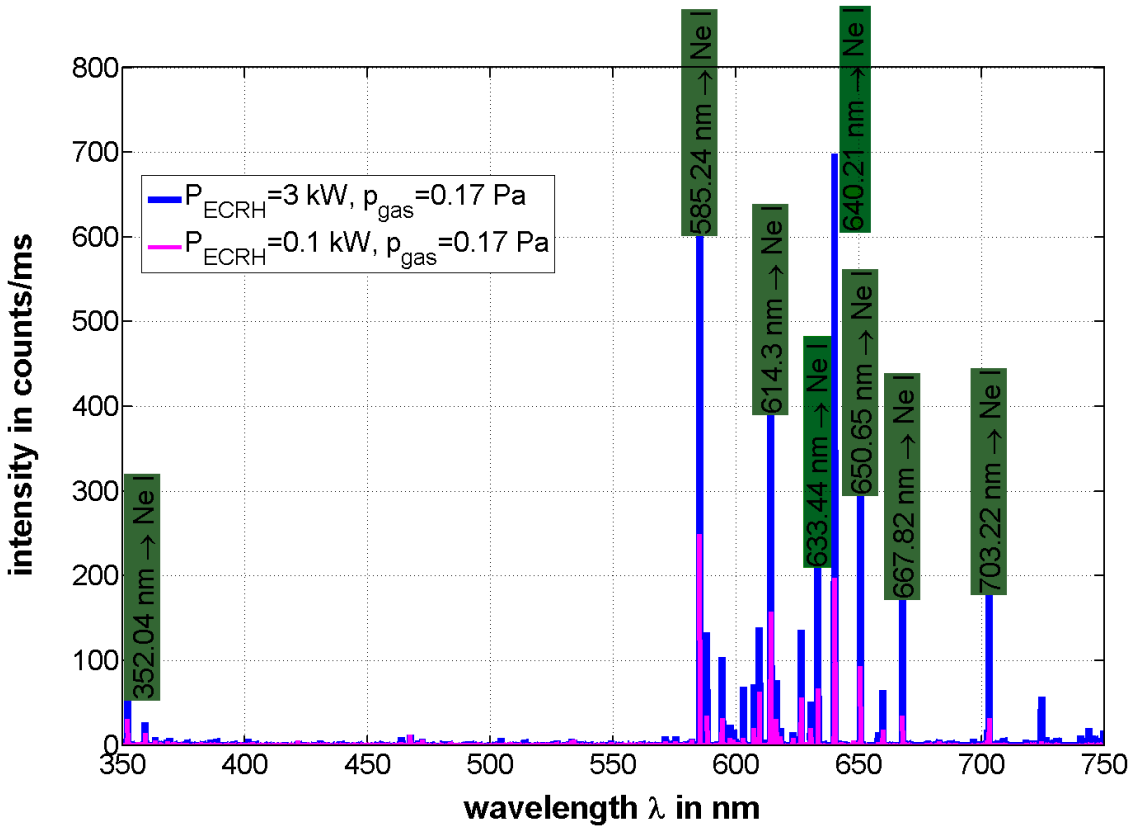

Figure 74 – Emission spectrum of a neon discharge in VINETA.I for different operation parameters. Not all identified neon lines are marked for better overview.

List of Figures

An overview of all figures, where the copyright is owned by other people/institutions than the author of this thesis, is given in the following list:

Figure	License	Copyright
2	-	© IPP, illustration: Dr. Christian Brandt. Reproduced with permission.
14	CC BY 3.0	© 2018 IOP Publishing. Reproduced with permission. All rights reserved
17	CC BY 3.0	© 2018 IOP Publishing. Reproduced with permission. All rights reserved
24	CC BY 3.0	© 2018 IOP Publishing. Reproduced with permission. All rights reserved
47	-	© Adrian von Stechow. Reproduced with permission.
48	-	© Tilmann Lunt. Reproduced with permission.
49	-	© IPP, photo: Volker Rohde. Reproduced with permission.
51	CC BY 3.0	© 2018 IOP Publishing. Reproduced with permission. All rights reserved
52	CC BY 3.0	© 2018 IOP Publishing. Reproduced with permission. All rights reserved
53b	CC BY 3.0	© 2018 IOP Publishing. Reproduced with permission. All rights reserved
54a	CC BY 3.0	© 2018 IOP Publishing. Reproduced with permission. All rights reserved
56	CC BY 3.0	© 2018 IOP Publishing. Reproduced with permission. All rights reserved
58	CC BY 3.0	© 2018 IOP Publishing. Reproduced with permission. All rights reserved
60	CC BY 3.0	© 2018 IOP Publishing. Reproduced with permission. All rights reserved
61b	CC BY 3.0	© 2018 IOP Publishing. Reproduced with permission. All rights reserved
61c	CC BY 3.0	© 2018 IOP Publishing. Reproduced with permission. All rights reserved
62b	CC BY 3.0	© 2018 IOP Publishing. Reproduced with permission. All rights reserved
63a	CC BY 3.0	© 2018 IOP Publishing. Reproduced with permission. All rights reserved
63b	CC BY 3.0	© 2018 IOP Publishing. Reproduced with permission. All rights reserved

List of Publications and Conference Contributions

Publications

Important results which originated from this PhD thesis are summarised as articles and planned to be submitted in international scientific journals with peer-review system.

Doppler Coherence Imaging of Divertor and SOL flows in ASDEX Upgrade and Wendelstein 7-X D. Gradic, O.P. Ford, A. Burckhart, F. Effenberg, H. Frerichs, R. König, T. Lunt, V. Perseo, R.C. Wolf, AUG Team and W7-X Team *Plasma Phys. Control. Fusion* ***60*** *(2018) 084007 (12pp)*
https://doi.org/10.1088/1361-6587/aac4d2

The article is written completely by myself and I have done all simulations and calculations for the ASDEX-Upgrade measurements and analysis. O. Ford, A. Burckhart and T. Lunt have helped to set-up the Doppler CIS on AUG. R.C. Wolf contributed by constructive discussions and feedback. All parts of the article about W7-X are not part of my PhD thesis. F. Effenberg and H. Frerichs provided the simulations and images for W7-X flow simulations. V. Perseo, O. Ford and R. König have mainly designed and set-up the Doppler CIS on W7-X.

A second paper (no title yet) on the calibration procedure for the Doppler CIS in ASDEX Upgrade is currently under work and is planned to be submitted to *Review of Scientific Instruments*.

Conference Contributions

- DPG Frühjahrstagung 2015
  02.03. to 06.03.2015 in Bochum
  Poster: **Doppler coherence imaging of ion dynamics in the plasma experiment VINETA**
  D. Gradic, O. Ford and R. Wolf

- 20th International Stellarator-Heliotron Workshop
  05.10. to 09.10.2015 in Greifswald
  Poster: **Doppler coherence imaging of ion dynamics in VINETA II**
  D. Gradic, O. Ford, R. Wolf and VINETA Team

- DPG Frühjahrstagung 2016
  29.02. to 04.03.2016 in Hannover
  Talk: **Doppler coherence imaging of Ion Dynamics in VINETA II and ASDEX-Upgrade**
  D. Gradic, O. Ford, T. Lunt, R. Wolf and VINETA Team

- DPG Frühjahrstagung 2017
  13.03. to 17.03.2017 in Bremen
  Poster: **Doppler Coherence Imaging of impurity ion flows in ASDEX-Upgrade divertor and plasma flows in VINETA.II**
  D. Gradic, O. Ford, T. Lunt, R. Wolf, ASDEX-Upgrade Team

- 2nd European Conference on Plasma Diagnostics
  18.04. to 21.04.2017 in Bordeaux (France)
  Talk: **Absolutely calibrated Doppler coherence imaging flow measurements in the divertor of a tokamak**
  D. Gradic, O. Ford, T. Lunt, R. Wolf and ASDEX-Upgrade Team

- 21st International Stellarator-Heliotron Workshop
  02.10. to 06.10. 2017 in Kyoto (Japan)
  Poster: **Doppler Coherence Imaging of Divertor and SOL flows in W7-X and ASDEX-Upgrade**
  (awarded with student poster prize)
  D. Gradic, O. Ford, V. Perseo, T. Lunt., R.C. Wolf, D. Ennis, ASDEX-Upgrade Team and W7-X Team

Acknowledgements

This work would not have been possible without the help and encouragement of many people. First and foremost, I would like to thank my supervisor, Oliver Ford, for guiding me in so many fields, be it physics or diagnostic related. He always took time for me, even during very busy times such as the current W7-X campaign, and never failed to provide reasonable (and fast!) answers to my many questions. It was a great pleasure to work together with him, whether to enjoy from his vast experience or his ability to always be motivating and encouraging.
My deepest gratitude goes to my academic supervisor, Prof. Robert Wolf, for employing me as a PhD at IPP and putting the trust in me to work on this very interesting PhD topic that allowed me to gather much insight into many areas. He also always supported me and found the time for many discussions in case of questions.
Many thanks as well go to Andreas Burckhart for his support to install the CIS on AUG, unconditional help and generously borrowing me his bicycle for almost 2 months. Felix Reimold (FZ Jülich), Yühe Feng, Florian Effenberg (University of Wisconsin) and Tilmann Lunt for many explanations of their codes and discussions about the physical mechanisms of SOL flows. Scott Silburn (CCFE), Cameron Samuell (Lawrence Livermore National Laboratory) and Prof. John Howard (ANU) for correspondences about the Doppler CIS diagnostic, much helpful feedback and discussions and the latter two also for a very nice first meeting at the ECPD 2017.

It has been a great pleasure to work at IPP during my PhD years. I am very grateful to many of my colleagues at IPP, both in Garching and Greifswald. The large majority of them helps to create a friendly and constructive working atmosphere. High-temperature plasma physics is a scientifically challenging field that requires the cooperation of many talented scientists, engineers and computer scientists around the world. At IPP, there is the possibility to work together with a large team of people on two experiments, ASDEX Upgrade and Wendelstein 7-X, that have contributed and promise to contribute significantly towards the realisation of future fusion power plants. I want to thank Ralf König, Ralph Dux and Steffen Potzel for much advice and help on spectroscopic matters. Ekkehard Pasch for help during the search of spectral lamps and power supplies for it. The entire VINETA group (Olaf Grulke, Kian Rahbarnia, Thomas Windisch, Birger Buttenschön, Adrian von Stechow, Nils Fahrenkamp, Timo Schröder, Dusan Milojevic, Ilya Shesterikov, Joel Clementson, Benjamin Brünner) for their help, providing data, discussions and their support for my VINETA.I and VINETA.II measurements. In particular Nils for letting me use the LIF laser for wavelength scans with my diagnostic, Ilya for the langmuir probe measurements and Adrian for his calculations. Marco Wischmeier, Thomas Pütterich and Marco Cavedon for their help in the discovery of a mistake in my analysis code. The latter one also for borrowing me a Zr calibration lamp for He II measurements. Christoph Biedermann for allowing Oliver and me the use of his spectroscopy laboratory and equipment (and occasionally "loaning" stuff). Jürgen Baldzuhn, Maceij Krychowiak, Bernd Kurzan, Matthias Otte and Alexander Lebschy for allowing me to use their spectrometers. Volker Rohde and Detlef Bösser for their advice and help to heat out the image fibre bundles. Michael Endler and the IPP Garching Werkstatt for supplying components for the CIS. And Maria Radau for everything in general and her help after my bicycle accident in particular.

I would like to thank my office colleagues, fellow PhDs and friends who were always open for discussions and support, participated in many funny and long board game evenings or were generous suppliers of chocolate: Alexander Rodatos, Felix Warmer, Holger Niemann, Peter Drewelow, Manuel Zolchow, René Reimer, Humberto Trimino-Mora, Georg Schlisio, Daniel

Böckenhoff, Lukas Rudischhauser and Valeria Perseo. Also, further away, my friends Sophia, Lena and Antje.
Lastly, I would like to thank my family for their continuous support and love.